2019•2020

Faculteit Industriële ingenieurswetenschappen

master in de industriële wetenschappen: bouwkunde

Masterthesis

Simulation of the dynamic behaviour of unreinforced non-structural masonry elements under combined horizontal and vertical seismic inputs

PROMOTOR :

Prof. dr. ir. Herve DEGEE

PROMOTOR :

Prof. Andrea PENNA

BEGELEIDER :

Ph. D. Stylianos KALLIORAS

Dries Eerdekens, Tom Weetjens

Scriptie ingediend tot het behalen van de graad van master in de industriële wetenschappen: bouwkunde

Gezamenlijke opleiding UHasselt en KU Leuven

2019 • 2020

Faculteit Industriële ingenieurswetenschappen

master in de industriële wetenschappen: bouwkunde

Masterthesis

Simulation of the dynamic behaviour of unreinforced non-structural masonry elements under combined horizontal and vertical seismic inputs

PROMOTOR :

Prof. dr. ir. Herve DEGEE

PROMOTOR :

Prof. Andrea PENNA

BEGELEIDER :

Ph. D. Stylianos KALLIORAS

Dries Eerdekens, Tom Weetjens

Scriptie ingediend tot het behalen van de graad van master in de industriële wetenschappen: bouwkunde

UHASSELT KU LEUVEN

Deze masterproef werd geschreven tijdens de COVID-19 crisis in 2020. Deze wereldwijde gezondheidscrisis heeft mogelijk een impact gehad op de opdracht, de onderzoekshandelingen en de onderzoeksresultaten.

Acknowledgements

The present Master's thesis is the product of a collaboration between the Universities of Hasselt (UHasselt) and Leuven (KULeuven) in Belgium, and the University of Pavia (UniPV) in Italy. We are indebted to our supervisor from the UHasselt, prof. dr. ir. Hervé Degee, for his valuable advice and constructive comments during the authoring of this thesis, and his constant encouragement throughout the project. We would also like to recognise the contributions made to this thesis by our supervisors from the UniPV, dr. Stylianos Kallioras and prof. Andrea Penna, for their excellent guidance and support during the elaboration of the models for the non-linear time-response analyses. Their insight and knowledge on the subject were critical to the success of this project.

The numerical simulations included in this work were performed using the software *Trilly*, a set of Matlab routines allowing the analysis of the dynamic response of local unreinforced masonry (URM) mechanisms, developed by the *Masonry Structures* research group at the UniPV. The experimental data employed for the calibration of the numerical models were obtained from a series of shake-table tests on three nominally identical URM buildings, carried out at the UniPV and the European Centre for Training and Research in Earthquake Engineering (EUCENTRE) in Pavia. These tests were part of the EUCENTRE project *'Study of the vulnerability of masonry buildings in Groningen'* within the research framework programme on hazard and risk of induced seismicity in the Groningen province of the Netherlands, sponsored by the Nederlandse Aardolie Maatschappij BV (NAM) [1]. The experiments aimed at evaluating the influence of the vertical acceleration component of ground motions on the dynamic response of URM buildings.

Table of contents

List of Tables

List of Figures

Abstract

Recently, a series of full-scale shake-table experiments on three identical unreinforced masonry (URM) building specimens were carried out at the University of Pavia and the European Centre for Training and Research in Earthquake Engineering. The tests investigated the dynamic behaviour of the buildings under uni-, bi-, and tri-directional ground motions.

Numerically simulating the seismic response of non-structural URM building components under bi-directional (i.e. combined horizontal and vertical) input accelerations seems to be sensitive to multiple parameters. Literature on the influence of the input parameters on the response of such masonry elements was limited. This Master's thesis simulates the experimental seismic performance of chimneys, parapet and gable walls under multi-directional input motions, and evaluates the range of the input parameters that best capture the dynamic behaviour of these elements.

The simulations were performed using *Trilly*, a programme for the analysis of the dynamic response of local URM mechanisms through simplified single-degree-of-freedom systems. Comparing the numerical and experimental responses of the building components showed that the software could reproduce accurately the dynamic behaviour under both uni-, and multi-directional input motions. The results provide numerical parameters that best fit the experimental data. Additionally, the study compares the efficiency of different damping models. The constant damping coefficient turned out to be the most reliable damping model.

Abstract in het Nederlands

Recent zijn er een reeks levensgrote schudtafeltesten uitgevoerd op drie identieke ongewapende metselwerkgebouwen door de Universiteit van Pavia en het Europees Centrum voor Training en Onderzoek in Aardbevingstechniek. De testen onderzochten het dynamisch gedrag van de gebouwen onder één-, twee- en driedimensionale seismische bewegingen.

Het numeriek simuleren van de seismische respons van niet-structurele ongewapende metselwerkcomponenten onder tweedimensionale (zijnde horizontale en verticale) inputacceleraties blijkt gevoelig te zijn aan meerdere parameters. De bestaande literatuur op de invloed van deze inputparameters op het dynamisch gedrag was tot recent beperkt. Deze masterproef simuleert het experimentele seismische gedrag van schoorstenen, borstweringen en gevelmuren onder meerdimensionale acceleraties en evalueert het ontstane scala aan waarden voor de inputparameters.

De simulaties zijn uitgevoerd met *Trilly*, een programma voor de analyse van het dynamische gedrag van ongewapende lokale metselwerkmechanismen via vereenvoudigde systemen met één vrijheidsgraad. Het vergelijken van de numerieke en experimentele respons van de componenten toont aan dat de software op een accurate manier het dynamisch gedrag voor zowel één- als meerdimensionale acceleraties kan simuleren. De resultaten tonen hierbij de inputparameterwaarden. Bovendien is er een vergelijking uitgevoerd naar de efficiëntie van de verschillende dempingsmodellen. Hieruit blijkt de *constant damping coefficient* het meest betrouwbaar te zijn.

1 Introduction

1.1 Background

Unreinforced masonry (URM) buildings are primarily seen as vertical load-bearing structural systems, meaning they transfer vertical loads from each floor and wall to the foundation. Despite the evident high strength and stability of URM structural components under gravity loads, their vulnerability to horizontal loads should not be neglected. Horizontal loads, like wind and seismic actions, cause high bending moments and horizontal displacements that affect the stability of structural and non-structural URM elements significantly. For instance, damage due to horizontal actions can cause the fall of a chimney, and the local collapse of a part of the structure.

Historically, in the Benelux Union, seismic events happen rarely (approximately once a year), causing minor damage only. However, in the Groningen region of the Northern Netherlands, low-intensity earthquakes have occurred several times over the past two decades. These earthquakes have caused minor damage to the local building stock, which consists mainly of URM buildings [2]. This increased seismicity is due to the local natural gas extraction activities, which induce soil compaction and consequent ground shaking of low intensity [3].

Recently, an experimental study conducted at the UniPV and the EUCENTRE investigated the effects of both tectonic and induced seismicity scenarios on the seismic behaviour of URM structures, also accounting for the multi-directionality of ground motions. The experiments included a series of shake-table tests on three identical URM building specimens, constructed at full scale. One of the employed seismic input motions for the shake-table tests was a three-component recording from the M_W 3.4 2018 Zeerijp earthquake, induced by the natural gas production activities at the Groningen gas field in the Northern Netherlands. Another set of acceleration recordings was employed, coming from the M_W 5.9 seismic event of 26 October 2016 near Visso, which was one of the major seismic events of the 2016 Central Italy earthquake sequence. In the latter case, the horizontal and vertical acceleration components were stronger in amplitude and better synchronised when compared with the first one, creating the conditions for inducing more significant damage to the URM building specimens [4, 5].

1.2 Scope

As mentioned above, URM buildings can suffer both structural and non-structural damage when subjected to seismic actions. Thus, the availability of reliable analysis software and calculation methods to study the seismic response of both global and local mechanisms in this type of buildings is of great importance.

In this study, the focus will be placed on the calibration and validation of a software package for the numerical analysis of the dynamic response of non-structural components commonly found in URM buildings, such as chimneys, gables and parapet walls. To that end, the experimental data from the shake-table tests described above will be exploited. The software, named *Trilly* (developed at the University of Pavia [6]), is a set of Matlab routines allowing the analysis of the dynamic response of local URM mechanisms through the use of simplified single-degree-of-freedom (SDOF) systems. Recently, *Trilly* has been used to perform non-linear time-history analysis of URM walls, also accounting for the combined action of horizontal and vertical accelerations.

By varying different input model parameters, the software can be tuned to simulate with satisfying accuracy the dynamic response of URM components of different geometry and mechanical properties. Specifically, the software *Trilly* can model the one-way out-of-plane (OOP) bending mechanisms of vertical spanning strip walls, the overturning mechanisms of chimneys, parapets and gable walls, as well as two-way OOP bending mechanisms of well-restrained building walls. In this Master's thesis, investigating the influence of various input model parameters will allow tuning a series of reliable SDOF systems that capture the experimental dynamic response of typical URM building components at full scale.

1.3 Thesis Outline

This Master's thesis is organised in the structure described below. Chapter 1 provides an introduction to the subject by informing about the seismic vulnerability of URM buildings to seismic actions, and by outlining the investigations that will be carried out in the later chapters of the thesis. Chapter 2 provides a detailed review of the existing literature on the numerical modelling methods for the assessment of the OOP response of URM walls. Chapter 3 describes the experimental reference study used in the thesis. Chapter 3 also describes the main features of the numerical analysis tool used to simulate the experimental seismic response of the non-structural URM building components under examination. Chapter 4 presents the characteristics of the examined building components and the approach that was followed to simulate the experiments through non-linear time-history analysis. Chapter 5 presents the analysis results, discussing the response of the elements before and after cracking separately. Finally, Chapter 6 summarises the findings of this Master's thesis and proposes future developments of the work.

2 Literature Review: Out-of-Plane Behaviour of URM Walls

2.1 Static Force-Displacement Relationships

The OOP behaviour of URM walls is initially characterised by a linear elastic response, followed by the non-linear elastic force-displacement response due to rocking behaviour after the formation of cracks and hinges. The flexural stiffness of the masonry controls this linear elastic branch. Figure 1 shows the experimental force-displacement relationship of a two-leaf URM wall subjected to one-way OOP bending (through airbag tests). The plot is provided in terms of the applied lateral load versus the displacement at level of the cracking.

A URM wall can exhibit a rocking behaviour only after the formation of a hinge, which is created when cracks occur in the masonry. The force for which these cracks appear is the cracking force, denoted by F_{cr}. The OOP response is often idealised by a linear elastic branch up to the attainment of F_{cr}, which causes a number of hinges needed to develop a rocking mechanism. The development of a mechanism is characterised by an explosive response at cracking and the transition into the rocking response, usually modelled through a bilinear or trilinear idealisation, as shown in Figure 2 [6]. To model the OOP response of URM panels correctly, it is of great importance to define carefully the necessary parameters controlling both the pre-crack linear-elastic response and the post-crack non-linear elastic response.

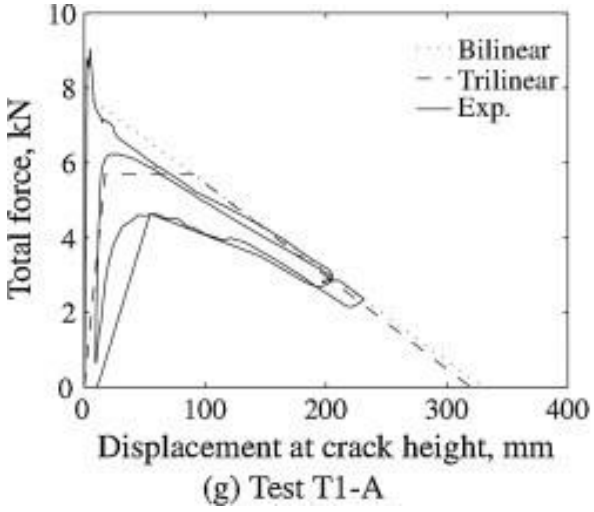

Figure 1: Airbag test performed on a two-leaf unreinforced masonry panel [7]

(a) (b)

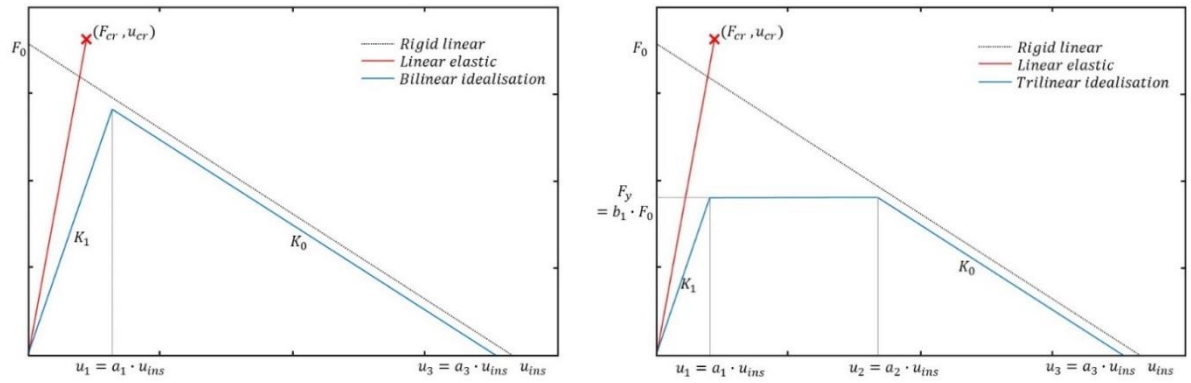

Figure 2: Idealisation of the non-linear elastic OOP force-displacement behaviour: (a) bilinear response curve; (b) trilinear response curve

2.1.1 The Pre-Crack Linear-Elastic Response

In order to predict well the OOP displacement demand, one should determine both the initial flexural stiffness and the lateral load resistance of the URM wall accurately. The correct definition of the model parameters is critical in ensuring an accurate estimation of both F_{cr} and the associated cracking displacement u_{cr} [6].

In the case of vertical spanning strip walls (VSSW) (as seen in Figure 3), there is a strong dependence of the initial elastic response phase on the restraint conditions at the top and bottom edges. These support conditions can be either pinned, or fixed, or anything in between. Consideration of the restraint conditions is made by means of parameters α_b and α_t, for the bottom and top ends of a wall, respectively. The two parameters take values between 0 (pinned configuration) and 1 (fully fixed configuration). In real masonry walls, α_b is generally higher than α_t, approaching 1 due to the more effective restraint conditions at the base of the wall [6].

The two limit support configurations that can be simulated with these two parameters are i) the double-fixed boundary condition ($\alpha_t = 1$ and $\alpha_b = 1$), and ii) the pinned-pinned boundary condition ($\alpha_t = 0$ and $\alpha_b = 0$). The double-fixed configuration leads to a stiffer behaviour of the wall since it requires the formation of three pivot points (through cracking) before the initiation of a rocking response mechanism. Usually, the first crack occurs at the top end of the wall due to the lower axial load. The second crack appears at the bottom end, while the last expected hinge appears at mid-height of the wall. On the contrary, a wall with pinned-pinned support configuration exhibits damage with cracking around its mid-height, frequently resulting in a force-displacement relationship with lower stiffness [6].

By assuming a uniformly distributed face load, the overall lateral force that triggers the formation of cracks can be calculated using Equation (1).

$$F_{cr} = \frac{\zeta + \sqrt{\zeta^2 - \frac{W^2}{4 \cdot b^2} - \frac{(\alpha_b \cdot M_b - \alpha_t \cdot M_t)}{b^3} - \frac{(\alpha_b \cdot M_b - \alpha_t \cdot M_t)^2}{b^4}}}{\frac{3 \cdot h}{2 \cdot b^2}} \quad (1)$$

In Equation (1), W is the weight of the wall, O is the gravity load on top of the wall, t is the thickness of the wall, f_w is the masonry bond strength, M_b is the cracking moment at the bottom end, and M_t

is the cracking moment at the top end. The latter quantities are computed using Equations (2) and (3).

$$M_b = \left(f_w + \frac{W + O}{b}\right) \cdot \frac{b^2}{6} \tag{2}$$

$$M_t = \left(f_w + \frac{O}{b}\right) \cdot \frac{b^2}{6} \tag{3}$$

The parameter ζ is calculated using Equation (4).

$$\zeta = f_w + \frac{1}{b} \cdot \left(\frac{W}{2} + O + \frac{3 \cdot (\alpha_b \cdot M_b + \alpha_t \cdot M_t)}{b}\right) \tag{4}$$

Equation (1) relies on the distribution of the maximum tensile stress $\sigma_t(x)$ along the wall height h. Equating the derivative of $\sigma_t(x)$ with zero, i.e. $\sigma_t{}'(x) = 0$, leads to Equation (5), which gives the location along the height of the wall, h_1, where the maximum tensile stress reaches the masonry flexural strength (f_w, which affects F_{cr}) [6]. Values for h_1/h of 0.5–0.7 are commonly seen in full-scale static and dynamic tests [8].

$$\frac{h_1}{h} = \frac{1}{2} + \frac{1}{h \cdot F_{cr}} \left(\frac{W \cdot \mathrm{b}}{6} + (\alpha_b \cdot M_b - \alpha_t \cdot M_t)\right) \tag{5}$$

The value of u_{cr} is computed by (6):

$$\mathrm{u_{cr}} = \frac{\beta}{384} \cdot \frac{F_{cr} \cdot h^3}{E \cdot I} \tag{6}$$

where β is a parameter that depends on the wall boundary conditions, with $\beta = 5$ for the pinned-pinned configurations, and $\beta = 2$ for the fixed-fixed configurations [6]. E is the masonry Young's modulus, and I is the moment of inertia of the wall section.

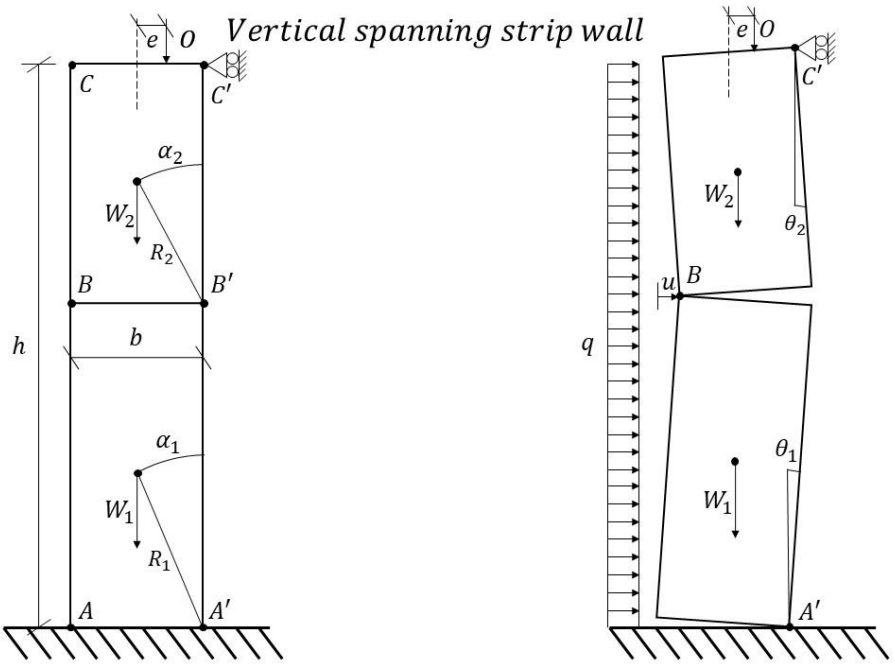

Figure 3: Vertical spanning strip wall forming an assembly of two rigid blocks with a rocking behaviour, at rest (left) and at its deformed shape (right)

In the case of a parapet wall (PW), which is a cantilever-type element (free top end and fixed bottom end, as shown in Figure 4), Equation (1) can be simplified as per Equation (7). The latter provides the required force F_{cr} to form a crack at the base of the PW, assuming a uniformly distributed face load [9]:

$$F_{cr} = m' \cdot g \cdot \frac{I}{\mathrm{b} \cdot h} \cdot (f_w + \frac{W + O}{A}) \quad (7)$$

where m' is equal to 3/5 of the total mass and A is the wall cross-section area.

2.1.2 The Post-Crack Non-Linear Elastic Response

After the exceedance of the linear elastic phase, the rocking behaviour of the URM wall is activated. Both the bilinear and trilinear representations of the OOP rocking response mechanism are based on the rigid-body idealisation of the wall, assuming infinite compressive strength and high slenderness. This behaviour is regulated by the force F_0, at which the rocking motion is triggered, and the displacement u_{ins}, which is the maximum attainable displacement of the wall before reaching static instability.

Figure 3 shows the deformed shape of a VSSW exhibiting pure rocking behaviour. This shape is characterised by the formation of hinges at the top, mid-height, and bottom cross-sections of the wall. These hinges (A', B', C') allow the VSSW system to act as two rigid bodies that rotate around these pivot points. The two resulting rigid bodies are characterised by the following quantities: the parameters α_1 and α_2, describing their slenderness (geometry); the weights W_1 and W_2, acting at the centre of mass (G_2 and G_2) of each body; and the rotations θ_1 and θ_2, which are calculated using Equations (8) and (9).

$$\theta_1 = \frac{u}{h_1} \quad (8)$$

$$\theta_2 = \frac{u}{h_2} \tag{9}$$

The rest of the system is defined by the vertical overburden force O, applied with an eccentricity e, and the horizontal displacement at the mid-height hinge, u [6]. Based on the assumption that the VSSW system responds as an assembly of two rigid bodies, the quantities F_0 and u_{ins} can be computed as:

$$F_0 = \frac{2}{h_1} \cdot (W + O) \cdot t + \frac{O}{h - h_1} \cdot (b + 2 \cdot e) \tag{10}$$

$$u_{ins} = \frac{\frac{2}{h_1} \cdot (W + O) \cdot t + O \cdot \frac{b + 2 \cdot e}{h - h_1}}{\frac{2}{h_1} \cdot (W + O) + \frac{2 \cdot O}{h - h_1}}. \tag{11}$$

Figure 4 shows a parapet wall (PW) in a rocking motion. The block is characterised by the radius distance R, which defines the distance of the centre of mass G from the pivot point O' (index of the size of the block), and the slenderness angle α, which is the arctangent of the ratio of thickness to height (b/h) [9]. The quantities F_0 and u_{ins}, determining the rigid-body bilinear force-displacement relationship can be derived using the Equations (12) and (13) provided below.

$$F_0 = \frac{1}{h} \cdot (W + O) \cdot b + \frac{2}{h} \cdot O \cdot e \tag{12}$$

$$u_{ins} = \frac{\frac{2}{h_1} \cdot (W + O) \cdot \frac{b}{2} - \frac{2}{h} \cdot O \cdot e}{\frac{2}{h} \cdot (W + 2 \cdot O)} \tag{13}$$

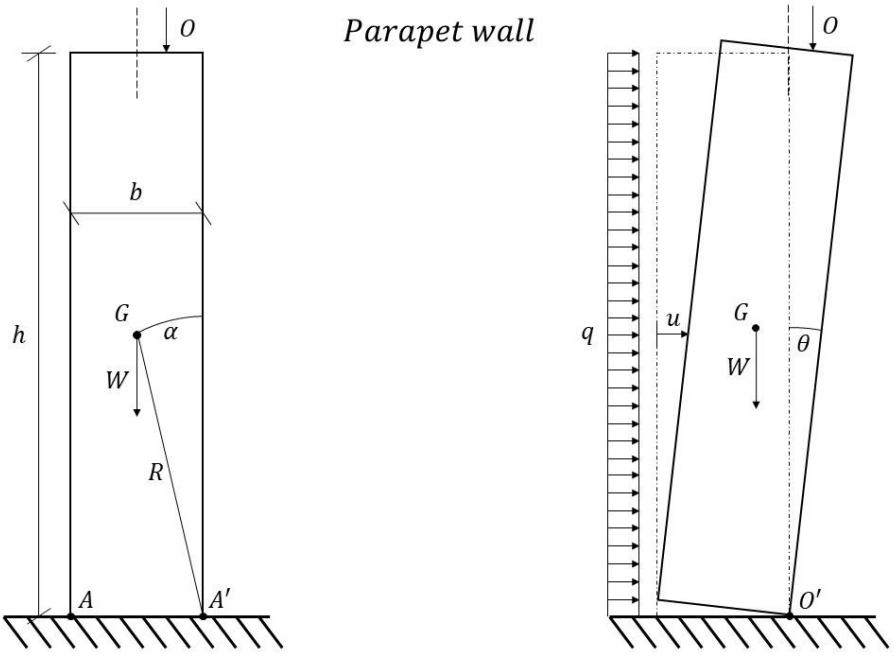

Figure 4: Parapet wall as a single rigid body with a rocking behaviour at rest (left) and at its deformed shape (right)

The calculated parameters F_0 and u_{ins} for both the VSSW and the PW systems are subsequently used to compute the negative stiffness of the overturning mechanism, K_0, which is commonly modelled through the use of the bilinear or trilinear elastic force-displacement response idealisations [9].

$$K_0 = \frac{F_0}{u_{ins}} \tag{14}$$

The bilinear OOP force-displacement response is further defined by the displacement parameters u_1 and u_3. The first displacement, u_1, controls the initial cracked stiffness of the wall while u_3 is the displacement corresponding to zero lateral force, in some cases matching u_{ins} (when the wall is made of infinitely rigid material). Taking into account the masonry compressive strength and the physical dimensions of the hinges leads to Equations (15) and (16) [6]. Using u_1 and u_3, the force F_1 in the bilinear idealisation can be calculated using Equation (17).

$$u_1 = a_1 \cdot u_{ins} \tag{15}$$

$$u_3 = a_3 \cdot u_{ins} \tag{16}$$

$$F_1 = \frac{u_3 - u_1}{K_0} \tag{17}$$

In the case of the trilinear elastic response model, other parameters come into play. F_y describes the force that sets the height of the plateau shown in Figure 2. The lower corner displacement defining the force plateau is defined by u_1, whereas the higher corner displacement is termed u_2. The two parameters are computed using the Equations (18) and (19) provided below.

$$F_y = b_1 \cdot F_0 \tag{18}$$

$$\mathrm{u}_2 = a_2 \cdot u_{ins} \tag{19}$$

The factors a_1, a_3, and b_1 are dependent on wall thickness, the acting vertical overburden force and the mechanical properties of the masonry [10]. In a study conducted by Doherty *et al.* (2000), it was concluded that the values of a_1, a_2, and b_1 increased in value when the rotation mortar joints further degraded. The degradation of the pivot points can originate from two phenomena; (i) the pivots possessing finite dimensions, instead of the general assumption of them being infinitesimally small; and (ii) the URM wall having a finite lateral stiffness instead of being infinitely rigid. Ultimately, this results in a lever arm less than half the thickness of the wall (as is assumed for an infinitely rigid wall), affecting the resistance of the wall to lateral forces [11]. It defines three stages of degradation: new, moderate and severe degradation corresponding to a_1 values of 0.06, 0.13 and 0.20, b_1 values of 0.72, 0.60 and 0.50 and a_2 values of 0.28, 0.40 and 0.50 [11, 12]. The value of a_3 depends on the type of material: a soft material will bring the pivot point closer to the centreline of the cross-section, which is translated into a lower value of a_3.

2.2 Dynamic Rocking Behaviour

The dynamic behaviour of rocking systems, described by the equation of motion, can be directly derived from Lagrange's equation of motion [13]. The undamped SDOF equation of motion for a rocking block under the hypothesis of no sliding, no bouncing effect, high slenderness and assuming that both supports move simultaneously in the case of VSSW systems, is the following [14]:

$$m' \cdot a(t) + f_{bi}(u,t) = -\lambda \cdot m' \cdot a_g(t) \tag{20}$$

In this equation, m' is the effective mass of the system, $a(t)$ is the system equivalent acceleration, f_{bi} is the restoring force, λ is a factor that allows the mobilisation of the entire mass of the system in the excitation term (i.e. the right side of the equation), and $a_g(t)$ is the input acceleration [6, 9]. Table 1 defines the parameters involved in the equation of motion as a function of whether it is a VSSW or PW system.

Table 1: Parameters involved in the equation of motion for VSSW and PW systems [14]

System	$\boldsymbol{m'}$	$\boldsymbol{f_{bi}(u,t)}$	$\boldsymbol{\lambda}$
VSSW	$\frac{2}{3}\cdot(m_1+m_2)$	$\frac{2}{h_1}\cdot W\cdot\big(b-u(t)\big)+\frac{h}{h_1\cdot h_2}\cdot O\cdot\big(b+2\cdot e-u(t)\big)+\frac{2}{h_1}\cdot O\cdot(b-2\cdot e)$	$\frac{3}{4}$
PW	$\frac{4}{3}\cdot m$	$\frac{2}{h}\cdot W\cdot\left(\frac{b}{2}-u(t)\right)+\frac{2}{h}\cdot O\cdot\left(\frac{b}{2}-e-2\cdot u(t)\right)$	$\frac{3}{2}$

2.3 Energy Dissipation via Coefficient of Restitution

A URM wall will experience damping of its motion due to energy dissipated through the impact of the wall during rocking. A common approach to implement this damping mechanism in the dynamic response model of the system is the use of a coefficient of restitution (CR), relying on the classical hypotheses of impulsive dynamics [14].

The energy dissipation through the CR occurs after each half rocking cycle, reducing the angular velocity by a certain amount compared to the angular velocity of the immediately preceding half rocking cycle. This way, the CR can be defined as the angular velocity after impact (ω_{i+1}) divided by the angular velocity before impact (ω_i) [15]:

$$CR = \frac{\omega_{i+1}}{\omega_i} \tag{21}$$

Analytically the CR can be derived for both the VSSW and PW systems, based on the following assumptions: i) infinitesimal impact duration (resulting in an instant change of velocity); ii) no displacement during impact; iii) conservation of angular momentum around the rotational hinge before and after the impact [14]. The resulting formulas are shown in Equations (22) and (23) (described in [14]). This CR reduces the velocity of the system after every impact with respect to the velocity right before the impact. In symbols:

$$e_{an,VSSW} = 1 - 2\cdot\sin^2(\alpha_1) \tag{22}$$

$$e_{an,PW} = 1 - \frac{3}{2} \cdot \sin^2(\alpha) \tag{23}$$

$$\omega(t + dt) = e_{an} \cdot \omega(t) \tag{24}$$

As can be noted in Equations (22) and (23), the CR values are only dependent on the shape (slenderness) of the block, not the overall size. The more slender the wall is, the lower α or a_1 will be, which results in a higher value of e_{an}, and thus in less energy dissipation [14].

However, the overall damping force that acts in rocking URM systems is not solely the energy released at impact. There is an additional, continuous energy dissipation that occurs due to the flexural response of the wall and the deformation of the rocking interfaces. To account for this additional dissipation of energy, the analytical coefficients of restitution should be lowered. A previous study conducted by Sorrentino *et al.* (2011) proposed the replacement of e_{an} for PW systems by $e_{exp} = 0.95 \cdot e_{an}$ [16]. According to the same researchers, for VSSW systems, e_{an} should also be reduced further as $e_{exp} = 0.90 \cdot e_{an}$ [14].

2.4 Energy Dissipation via Equivalent Viscous Damping

Apart from the coefficient of restitution, there are also other options to model the damping effect in rocking URM structures, such as the equivalent viscous damping (EVD). This approach defines a damping force that is velocity-dependent through either a constant, or variable (with cycle-to-cycle iterations) or stiffness proportional damping ratio [14].

There are three non-iterative EVD models examined here, with the first one being based on a constant damping coefficient (CDC). This model assumes a constant damping ratio (ξ) acting on the system circular frequency (ω_1) of the first force-displacement curve branch, which results in a damping coefficient as follows [14, 17]:

$$C_{CDC} = 2 \cdot m' \cdot \omega_1 \cdot \xi \tag{25}$$

The two other models capture the influence on the energy dissipation of oscillation amplitude and the current frequency of vibration of the system. Both models act on the instantaneous circular frequency $\omega(t)$ which is defined by the secant stiffness of the system $K_{sec}(t)$ [14].

$$\omega(t) = \sqrt{\frac{K_{sec}(t)}{m'}} \tag{26}$$

The second of three models is the constant damping ratio (CDR) which is associated with all frequencies:

$$C_{CDR} = 2 \cdot m' \cdot \omega(t) \cdot \xi. \tag{27}$$

The final model is the stiffness-proportional damping ratio (SDR):

$$C_{SDR} = 2 \cdot m' \cdot \omega(t) \cdot \xi\big(\omega(t)\big). \tag{28}$$

The SDR model required another parameter to be described, $\xi(\omega(t))$, which is the damping ratio that is dependent on the instantaneous circular frequency:

$$\xi(\omega(t)) = \xi_1 \cdot \frac{\omega(t)}{\omega_1} \tag{29}$$

with ξ_1 being the damping ratio at the circular frequency ω_1.

The three EVD models can be derived based on the CR and the systems geometry. Equations (30), (31), and (32) show these relationships [14].

$$\xi_{CDC} = -0.667 \cdot a_1^{0.450} \cdot \ln\left(\frac{e_{xp}}{e_{an}} \cdot e_{an}\right) \tag{30}$$

$$\xi_{CDR} = -0.350 \cdot a_1^{0.074} \cdot \ln\left(\frac{e_{xp}}{e_{an}} \cdot e_{an}\right) \tag{31}$$

$$\xi_{SDR} = -0.218 \cdot a_1^{-0.195} \cdot \ln\left(\frac{e_{xp}}{e_{an}} \cdot e_{an}\right) \tag{32}$$

The above EVD models can be implemented into an equation of motion, this way accounting for the energy dissipation of a rocking body system. The general modified SDOF equation of motion is shown in Equation (33).

$$m' \cdot a(t) + C_i \cdot v(t) + f_i(u,t) = -\lambda \cdot m' \cdot a_g(t) \tag{33}$$

Solving Equation (30) for the free vibrations of an example system described by Tomassetti *et al.* (2019) [14], results in Figure 5, which compare the three EVD models introduced above. The details of the VSSW system that was used for the calculations are: b = 0.10 m, h = 2.68 m, h_1 = 1.54 m, O = 0, a_1 = 0.04, d_1 = 0.85, and a_3 = 1; $u_0 = 0.9 \cdot u_{ins}$; v_0 = 0; ξ_{CDC} = 0.015, ξ_{CDR} = 0.027, $\xi_{1,SDR}$ = 0.044.

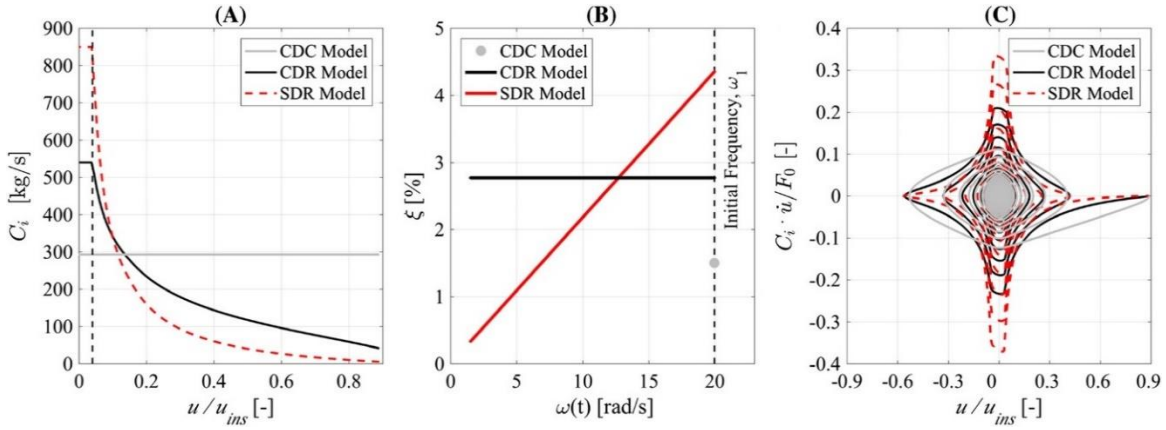

Figure 5: Comparison of various EVD models: (A) damping coefficient versus non-dimensional displacement for the CDC, CDR, and SDR models; (B) damping ratio versus circular frequency; and (C) normalised damping force versus normalised displacement amplitude of the three models during the decay of the oscillation [14, p. 1283]

For the CDC model, the damping force is obtained by the multiplication of the velocity with a constant quantity. On the contrary, the CDR and SDR models are characterised by a linear

relationship, C_i-u/u_{ins}, associating a damping ratio with the current secant frequency for any oscillation that is larger than the first corner point a_1 (as shown in Figure 5 (B) [14]).

In Figure 5 (C), it can be noticed that all EVD models develop a higher damping force around zero displacements, with this behaviour being more pronounced for the CDR and especially the SDR model. This sounds reasonable because, in a rocking system, damping will occur at impact, which occurs when the system passes through its rest position (at zero displacements) [14].

3 Numerical Modelling of the Rocking Response of Walls

This paragraph discusses the numerical model that is used for the analysis of the dynamic rocking response of the various non-structural masonry elements commonly seen in URM buildings. First, the reference experimental campaign that was consulted for the calibration of the numerical models is presented, then the proposed numerical models that best-capture the experimental behaviour of the considered elements are described.

3.1 Reference Experimental Campaign

The experimental study conducted by Kallioras *et al*. (2020) [4] served as a benchmark for the calibration of the numerical model that was employed for the analyses presented in the following paragraphs. The tests intended to investigate the effects of vertical input accelerations on the seismic behaviour of three identical URM building specimens, considering both tectonic and induced seismicity scenarios. One of the employed seismic input motions for the shake-table tests was a three-component recording from the 2018 Zeerijp earthquake (M_W 3.4; Groningen gas field). Due to the low amplitude and the long time interval between the horizontal and vertical acceleration components, this motion was not appropriate for testing the adverse/beneficial effects of the ground motion multi-directionality. As such, a second, stronger ground motion was used. This second set of acceleration recordings was from the seismic event of 26 October 2016 near Visso (M_W 5.9; 2016 Central Italy earthquake sequence). In this latter case, the horizontal and vertical acceleration components were stronger in amplitude and well synchronised, creating the conditions for inducing more significant damage to the URM building specimens [4, 5].

3.1.1 Building Specimens Overview

The three test buildings were identical in geometry and construction details. The prototype building consisted of a single story with a height of 2.82 m. The structure also included: i) a gable wall with a height of 1.95 m; ii) two chimneys of different heights (2.0 m at the South-West corner and 1.0 m at the South-East corner); iii) and three parapets extending over the floor level. The overall floor dimensions of the building specimens were 4.25 m in the North-South direction, and 4.04 m in the East-West direction [4, 5]. Photographs of the prototype building can be found in Figure 6. The ground-floor and first-floor plans can be seen in Figure 7.

The load-bearing walls consisted of unreinforced masonry, constructed using 215×100×50 mm^3 clay bricks shipped from the Netherlands. The bricks were bonded through 10-mm-thick head- and bed-joints, using an Italian lime mortar. The North, East, and West façades of the building consisted of a single (100-mm-thick) leaf. The South façade was constructed as a double (215-mm-thick) wythe wall, using the Dutch cross brickwork bond [4, 5].

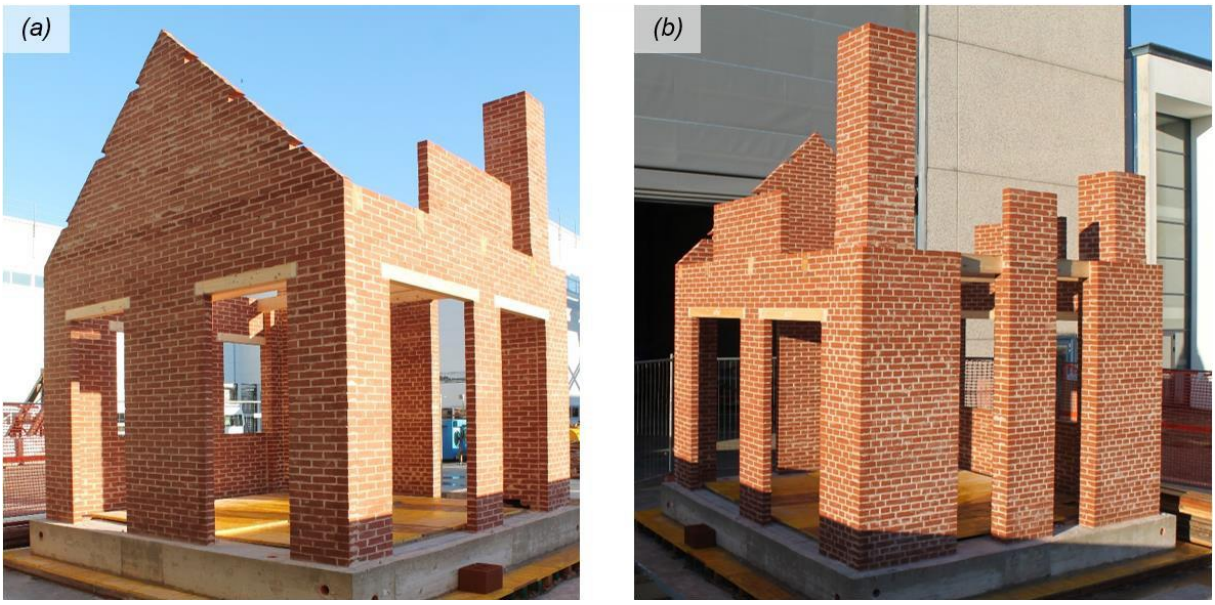

Figure 6: Full-scale building prototype: (a) North-West view; (b) South-West view [4, p. 5]

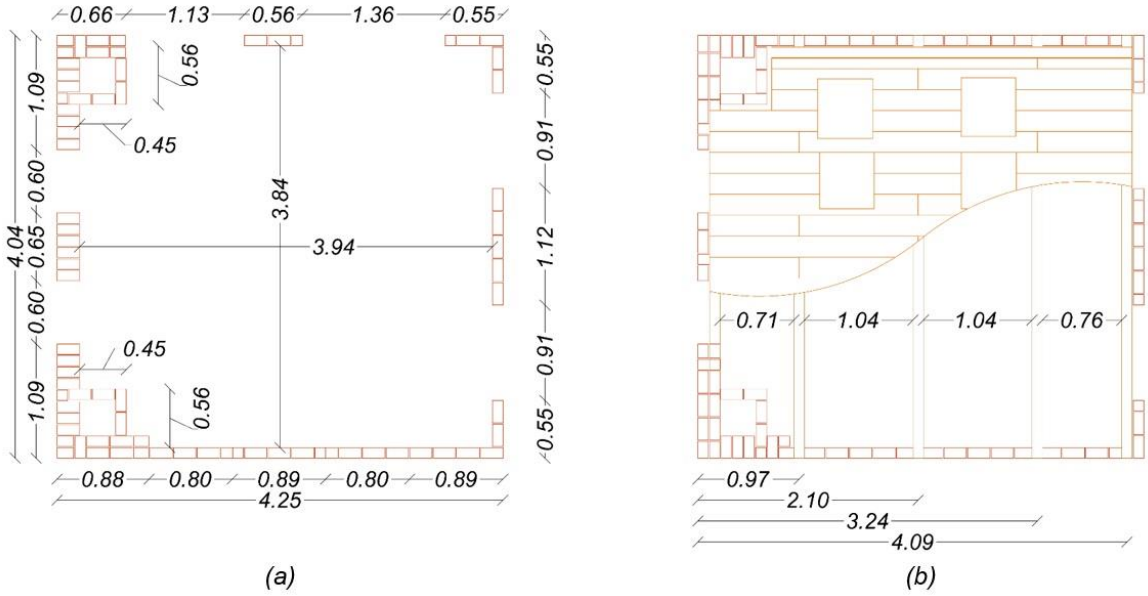

Figure 7: Full-scale building prototype: (a) ground-floor plan [m]; (b) first-floor plan [m] [4, p. 5]

3.1.2 Mechanical Properties of Materials

A series of strength tests were performed on mortar samples, clay units, and small masonry assemblies to determine the mechanical properties of the employed building materials. Tests were performed for all three URM building models; all specimens had an age exceeding 28 days. All tests were performed on materials of the same batches, which were used to construct the building specimens.

Table 2: Masonry mechanical properties of the building specimens [4, p. 17]

Mechanical property [units]	EUC-BUILD-8.1		EUC-BUILD-8.2		EUC-BUILD-8.3	
	Avg.	C.o.V.	Avg.	C.o.V.	Avg.	C.o.V.
Density of masonry, ρ_m [kg/m^3]	1950	-	1950	-	1950	-
Brick standard compressive strength, f_b [MPa]	43.5	0.10	43.5	0.10	43.5	0.10
Brick flexural strength, f_{bf} [MPa]	TBD	TBD	TBD	TBD	TBD	TBD
Mortar compressive strength, f_c [MPa]	1.14	0.24	1.37	0.24	1.36	0.21
Mortar flexural strength, f_t [MPa]	3.93	0.13	4.71	0.22	4.30	0.14
Masonry compressive strength, f_m [MPa]	9.74	0.19	11.1	0.05	11.7	0.09
Masonry Young's modulus in compression*, E_{m1} [MPa]	5300	0.28	7000	0.37	6700	0.28
Masonry flexural bond strength, f_w [MPa]	0.23	0.07	0.14	0.03	0.13	0.05
Masonry (bed-joint) cohesion, f_{v0} [MPa]	0.50	-	0.66	-	TBD	-
Masonry (bed-joint) initial shear-friction coefficient, μ [-]	0.80	-	0.71	-	TBD	-
Masonry (bed-joint) initial resistance in torsion, T_0 [kNm]	N/A	-	N/A	-	0.38	-
Masonry (bed-joint) shear-friction coef. in torsion, μ_{tor} [10^{-3} m^3]	N/A	-	N/A	-	0.11	-

TBD: To be determined in future tests within the experimental campaign conducted by Kallioras *et al.* (2020) [4] (postponed due to the COVID-19 outbreak).
N/A: not available data.
* E_{m1}: computed as equal to the slope of the secant at 33% of f_m on the σ-τ curve.

3.1.3 Seismic Input Motions

As mentioned at the beginning of Section 3.1, two different types of seismic motions were considered in the experimental study: induced and tectonic seismicity. For the induced seismicity scenario, a three-component, pulse-like acceleration recording from the 2018 Zeerijp earthquake in the Groningen gas field of the Netherlands was used (termed SC1) [18]. These types of earthquakes, caused by local natural gas extractions, are characterised by an overall low magnitude and a shallow depth. This results in ground motions of comparable vertical and horizontal motion intensities but with a low amplitude and short duration. Due to the shallow depth, the source-to-site distance is short, resulting in considerable time intervals between the horizontal and vertical ground motions, as can be seen in Figure 8 [4, 5].

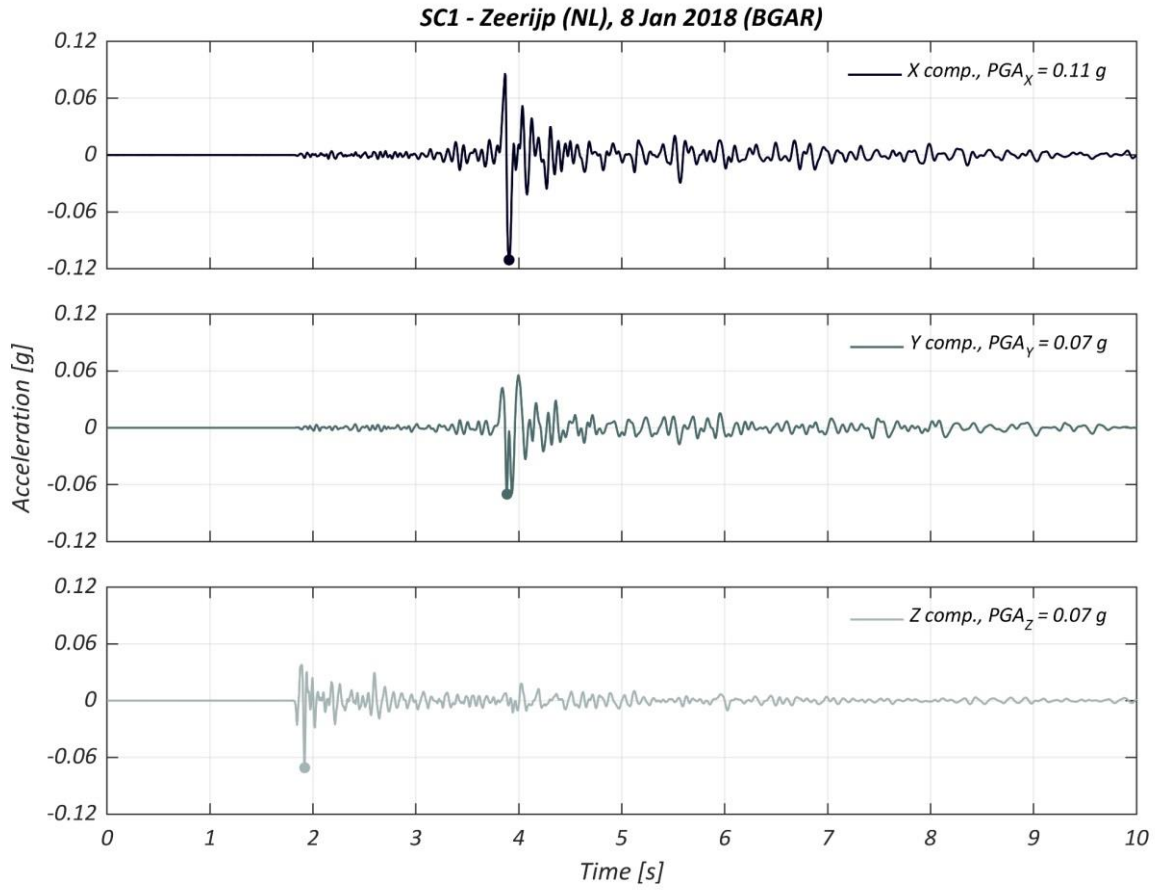

Figure 8: Seismic input motions SC1: acceleration recordings from the Zeerijp earthquake in Groningen, the Netherlands (BGAR station in Garsthuizen; lat: 53.368, long: 6.714) [4, p. 23]

For the tectonic seismicity scenario, a three-component motion recording from the seismic event of 26 October 2016 near Visso (from the 2016 Central Italy earthquake sequence) was adopted (termed SC2). This recording was preferred over ten other near-fault earthquake recordings carefully selected from the Near-Source Strong Motion (NESS) database. Some of the advantages of this recording over the rest ground motions of the dataset were: i) high amplitude of horizontal and vertical motions; and ii) coincident peaks between the horizontal and vertical motions. These elements were important to test the influence of vertical accelerations on the dynamic response of URM structures. The acceleration time series of the SC2 motion are shown in Figure 9, while Table 3 lists the characteristics of the two employed ground motions (SC1 and SC2) [4, 5].

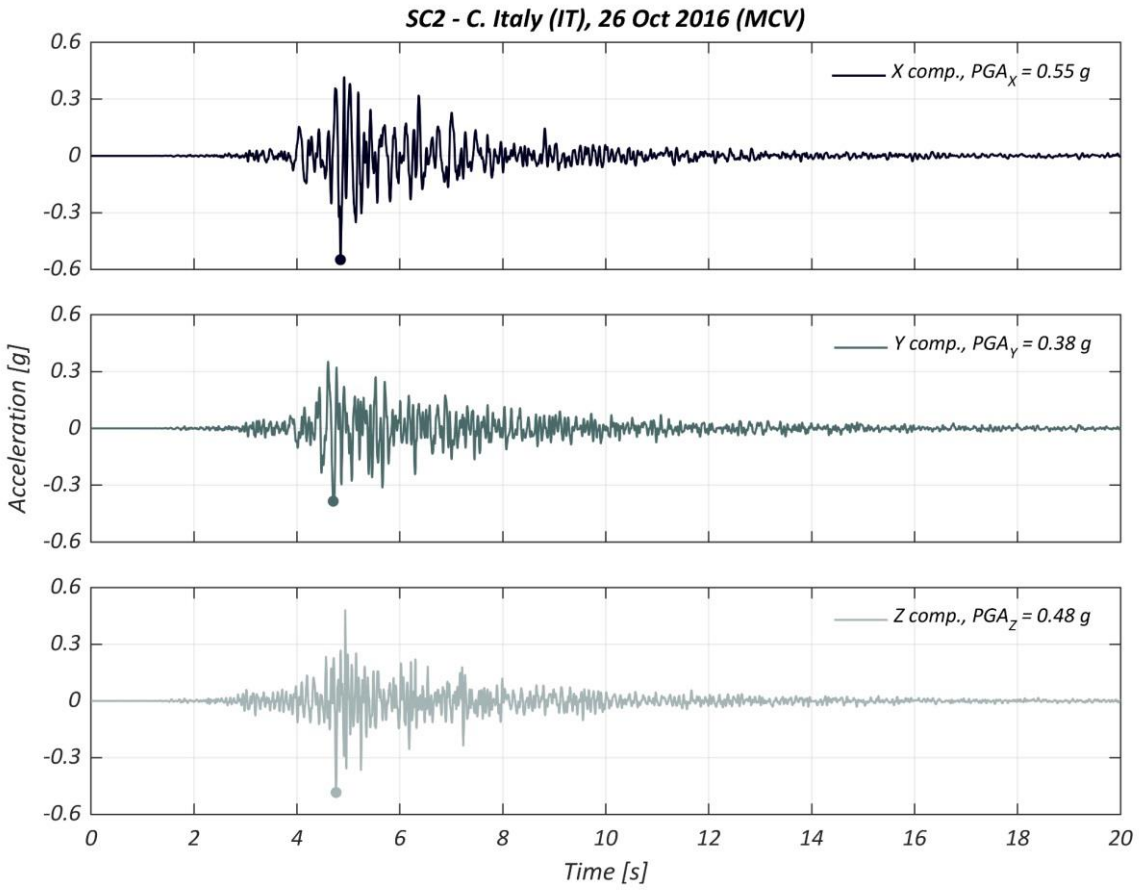

Figure 9: Seismic input motions SC2: acceleration recordings from the event of 26 October near Visso, during the 2016 Central Italy earthquake sequence (MCV station in Montecavallo; lat: 42.909, long: 13.129) [4, p. 24]

Table 3: Characteristics of the employed sets of ground motions [4, p. 22]

Event	Date and time	Station	M_W	R_{ep} [km]	D [km]	PGA_V/PGA_H* [-]	$\Delta t_{IA,5\%}$$ [s]	$I_{A,V}/I_{A,H}$+ [-]	PGV_V/PGV_H# [-]
Zeerijp (NL)	08/01/2018 14:00:52	Garsthuizen (BCAR)	3.4	2.5	3.0	0.64	1.97	0.27	0.21
C. Italy Visso (IT)	26/10/2016 19:18:06	Montecavallo (MCV)	5.9	14.0	7.5	0.88	0.22	0.55	0.37

*PGA_V/PGA_H: the ratio of peak vertical to peak horizontal ground acceleration. Indicates the magnitude of the relative instantaneous intensity of the vertical ground motion with respect to the horizontal ground motion, and the short-period spectral acceleration content.

$$\Delta t_{IA,5\%}$: time difference between the 5% accumulation of Arias intensity of vertical and horizontal ground motions. Indicates the synchronisation between the vertical and horizontal ground motions.

+$I_{A,V}/I_{A,H}$: ration of Arias intensity of the vertical to Arias intensity of the horizontal ground acceleration. Indicates the magnitude of the integral intensity of the vertical ground motion with respect to the horizontal ground motion.

#PGV_V/PGV_H: ratio of the peak vertical to the peak horizontal ground velocity. Indicates the magnitude of the relative instantaneous intensity of the vertical in relation to the horizontal ground motion, and the intermediate-period spectral acceleration content

3.1.4 Test Sequence

The test protocol consisted of nine incremental earthquake simulations, for which the seismic input motions were scaled in acceleration amplitude. The ground motion SC1 (Zeerijp 2018) was scaled at 50%, 100%, and 150%; the motion SC2 (Central Italy 2016) was scaled at 25%, 50%, 75%, 100%, 150%, and 200%. Before each earthquake simulation, shaking runs of lower intensity were performed to calibrate the system of shake table and building specimen [4, 5].

In between each earthquake simulation, the specimens were subjected to low-amplitude, random excitations. These excitations covered a wide frequency band from 0.1 to 40 Hz and had consistent energy content for the dynamic identification of the building specimens. These random excitation tests were applied to assess the effect of cumulative damage on the evolution of the global dynamic properties of the buildings at the end of each testing step [4, 5].

It is worth noting that after the earthquake simulation at SC2-75%, for all buildings, the North gable wall needed to be retrofitted due to significant displacements at the top of the wall. The strengthening interventions consisted of: i) four wall-to-diaphragm steel connectors at the floor-level; and ii) a timber end-plate outside the gable to prevent the out-of-plane overturning collapse of the gable [4, 5].

For a complete overview of the testing sequence for each building specimen, the reader is referred to the research report by Kallioras *et al*. (2020) [4, pp. 27-28]. The table lists from left to right the test ID-number and test name, the employed input signal, the motion components (X, Y, and Z) that were used in the test, and the scale factor applied to the ground motion.

3.1.5 Data Acquisition

During the shake-table tests, several sensors were used to capture the displacement and acceleration response of the building prototypes.

The conventional data acquisition systems consisted of typical potentiometers and accelerometers. Displacements were also monitored by a 3D-motion capture system, which consists of a set of cameras monitoring the motion of passive spherical markers attached to the wall of the building specimens, in all three directions (X, Y, and Z). This optical data acquisition system makes it possible to capture relative and absolute displacements of the building walls, as well as local displacements and deformations of the structural or non-structural building components. The acquired data has been used further in this thesis to compare the experimental data with the numerical simulations [4, 5].

3.2 Employed Numerical Models

As seen in Chapter 2, there are several modelling choices that need to be specified when performing a non-linear time-history analysis. This paragraph will describe which model parameters are adopted in the analysis using the *Trilly* software. In this thesis, only parapet walls will be analysed; no vertical spanning strip walls will be considered, so all Equations presented, or assumptions made in the following paragraphs of this study are based on parapet wall systems.

3.2.1 Static Force-Displacement Relationship

Both bilinear and trilinear relationships will be used in the simulation of the building components that are discussed here. For more information regarding the components, a reference to Chapter 4, Section 4.1 is made. As can be seen in that chapter, five building components are used as a reference to simulate their OOP response.

For the gable wall, and the South, East and West parapets, the bilinear force-displacement relationship will be used. In the case of the slender chimney, however, the trilinear force-displacement relationship will be used. The first four elements (i.e. the gable wall and the parapets) have a width of 0.10 m. In contrast, the slender chimney has a rectangular cross-section of 540×540 mm^2. The significantly wider cross-section of the chimney promotes the trilinear elastic idealisation as a more appropriate model of the force-displacement relationship. The gable wall and parapets have a width too small to form a plateau as is typical of the trilinear force-displacement relationship. Such thin walls can be better simulated using a bilinear elastic relationship.

3.2.2 Dynamic Behaviour

As has been stated also in Chapter 2, the dynamic behaviour of rocking URM elements can be divided into two phases. The first phase is the pre-crack phase, meaning the response phase before the attainment of the cracking force (F_{cr}). The second phase is the post-cracking, rocking response phase, accessed only after exceeding the force F_{cr}. This force creates hinges in the URM structure, which means the structure becomes a mechanism that can move around the formed hinges. The SDOF equation of motion that describes the pre-mechanism phase is written in Equation *(34)*.

$$m' \cdot a(t) + C_{lin} \cdot v(t) + f_{lin}(u,t) = -\lambda \cdot m' \cdot a_g(t) \qquad (34)$$

This pre-cracking phase equation of motion is linear; thus the effective mass (m') that is considered in this equation, is the effective mass of a linear deflected shape which is typical of a rocking response. Experimentally, however, the initially deformed shape is slightly different from this of the linear deflected shape, which is a limitation of this model [8]. The damping coefficient C_{lin} is constant during the analysis steps preceding the formation of cracks because it is based on the linear elasticity of the *F-u* relationship.

The equation of motion in the post-cracking phase can be written as Equation *(35)*.

$$m' \cdot a(t) + C_i \cdot v(t) + f_i(u,t) = -\lambda \cdot m' \cdot a_g(t) \qquad (35)$$

The parameters used in this equation of motion can be found in Table 1. Furthermore, C_i is the damping coefficient of the selected damping model among the CDC, CDR and SDR damping models; while f_i is the non-linear restoring force, being either bilinear f_{bi} or trilinear f_{tri} [14].

The effectiveness of EVD models in the simulation of experimental responses of VSSW elements has already been shown [6]. The CR can be estimated based on the given wall geometry by using several formulations (Equations. (22) and (23)). Using the CR value, the derivation of the EVD models can be performed as is already noted in Equations (30), (31), and (32). Using EVD models to simulate damping phenomena presents several advantages, such as: i) the formulation is in the same fashion as the one of a classic elastic oscillator; and ii) the implementation in finite-element environments is possible [14]. These advantages of the EVD models call for the use of one of these options to model damping throughout the thesis. The initial choice was to use the constant damping coefficient CDC; however, the application of the different EVD models will be compared in Chapter 0.

4 Simulation of Shake-Table Experiments

This study focusses on the simulation of the experimental seismic response of different non-structural URM elements subjected to dynamic excitation of increasing intensity. This chapter provides all necessary information regarding the full-scale shake-table tests, the seismic response of the building components in question, the calibration procedure of the numerical models, and the numerical simulation of the tests.

4.1 Considered URM Building Components

The objective of this Master's thesis is to provide a range of values for a set of input parameters that are of importance for the simulation of the seismic response of URM components under multi-directional seismic input, at both cracked and uncracked state. This is done by simulating the experimental response of various URM building components of three full-scale building specimens: i) EUC-BUILD-8.1, subjected to one horizontal input motion (X); ii) EUC-BUILD-8.2, subjected to one horizontal and a vertical input motion (X, Z); and iii) EUC-BUILD-8.3, subjected to two horizontal and a vertical input motion (X, Y, and Z).

The URM building components consist of elements located over the first-floor diaphragm of the building. Specifically, they consist in: i) the gable wall; ii) the South-West slender chimney; iii) the South parapet; iv) the East parapet; and v) the West parapet.

4.1.1 Gable Wall

The gable wall, located on the North façade of each building specimen, has a height of 1.94 m and a length of 4.04 m. It was built back to back with a timber truss, which allowed only the one-side rocking response of wall. During the testing sequence, the gable wall was retrofitted at shaking intensities of nominal PGA = 0.41 g using a timber plate to avoid the collapse due to out-of-plane overturning [4, 5].

Table 4 lists the different tests performed per building specimen, with the ID numbers as identified in the reference study [4, 5]. The table also provides the condition of the gable wall (cracked or uncracked) and the short name that will be used to refer to each specific test in what follows. The location of the gable wall on the first-floor plan is shown in Figure 10, while a view of the gable wall and the timber truss structure is shown in Figure 11.

As can be seen in Table 4, the SC1 ground motions did not cause any significant structural damage to the gable wall of buildings EUC-BUILD-8.1 and EUC-BUILD-8.3. In the case of EUC-BUILD-8.2, the first structural damage to the gable wall was noticed during the test SC1-100% [4, 5].

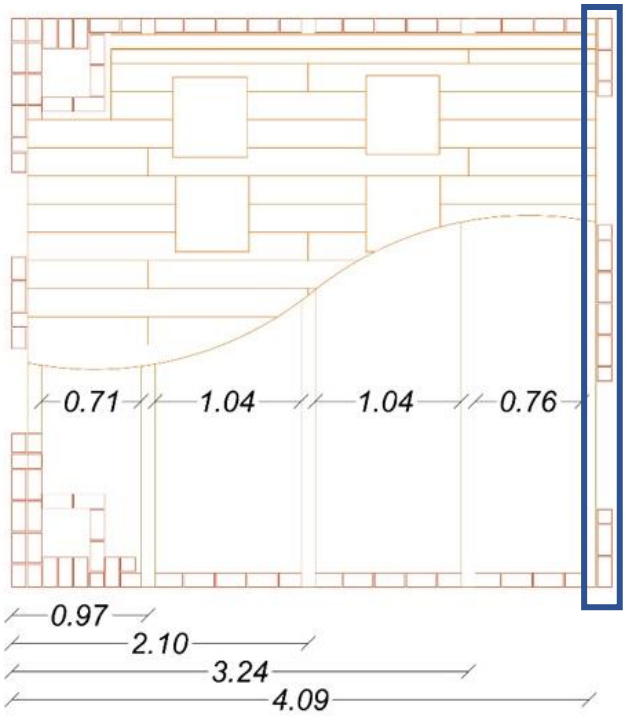

Figure 10: First-floor plan of the prototype building: location of gable wall [4, p. 5]

Figure 11: Gable wall built back to back with the timber truss [4, p. 12]

Table 4: Gable wall: list of testing sequence

Building specimen	Test name	Test ID	Damage condition	Short name
EUC-BUILD-8.1	SC1-50%	9	Uncracked	8.1-GW-9
	SC1-100%	12	Uncracked	8.1-GW-12
	SC1-150%	16	Uncracked	8.1-GW-16
	SC2-25%	22	Uncracked	8.1-GW-22
	SC2-50%	24	Cracked	8.1-GW-24
	SC2-75%	28	Cracked	8.1-GW-28
	Gable wall was retrofitted			
	SC2-100%	30	Cracked	8.1-GW-30
	SC2-150%	36	Cracked	8.1-GW-36
	SC2-200%	41	Cracked	8.1-GW-41
EUC-BUILD-8.2	SC1-50%	6	Uncracked	8.2-GW-6
	SC1-100%	9	Cracked	8.2-GW-9
	SC1-150%	13	Cracked	8.2-GW-13
	SC2-25%	18	Cracked	8.2-GW-18
	SC2-50%	21	Cracked	8.2-GW-21
	Gable wall was retrofitted			
	SC2-75%	28	Cracked	8.2-GW-28
	SC2-100%	30	Cracked	8.2-GW-30
	SC2-150%	32	Cracked	8.2-GW-32
	SC2-200%	34	Cracked	8.2-GW-34
EUC-BUILD-8.3	SC1-50%	6	Uncracked	8.3-GW-6
	SC1-100%	10	Cracked	8.3-GW-10
	SC1-150%	16	Cracked	8.3-GW-16
	SC2-50%	20	Cracked	8.3-GW-20
	Gable wall was retrofitted			
	SC2-75%	29	Cracked	8.3-GW-29
	SC2-100%	32	Cracked	8.3-GW-32
	SC2-150%	35	Cracked	8.3-GW-35
	SC2-200%	39	Cracked	8.3-GW-39

4.1.2 Slender Chimney

The slender chimney had a height of 2.04 m above the floor level and a flue of 340×340 mm^2. It was located at the South-West corner of the building [4, 5]. Table 5 provides information regarding the damage condition of the gable wall (cracked or uncracked), and the short name that will be used to refer to the specific test. Figure 12 shows the first-floor plan indicating the chimney, and Figure 13 shows a closer view of the chimney in-situ.

It is worth noticing that the free-standing part of the slender chimney of building EUC-BUILD-8.2 developed cracks only during shaking under the SC2-150% input motion, which was late in comparison to the other two building specimens.

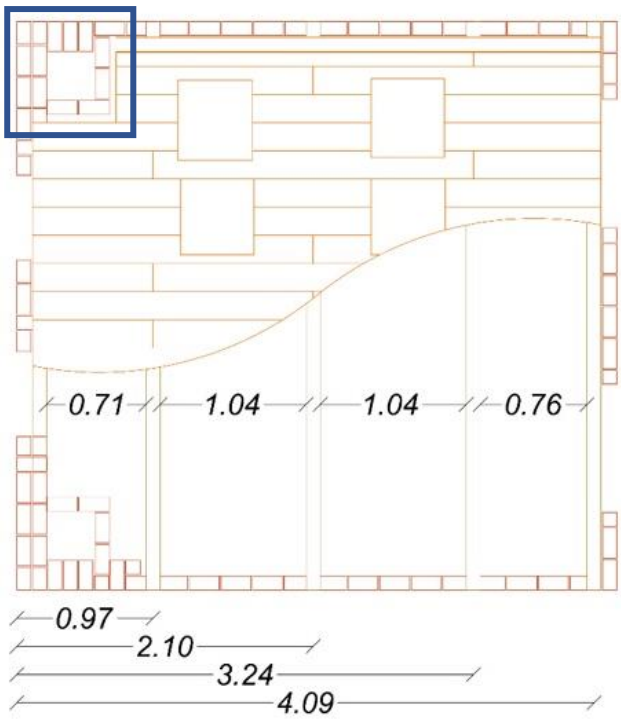

Figure 12: First-floor plan of the building prototype: location of the slender chimney [4, p. 5]

Figure 13: Slender chimney at the South-West corner of the building [4, p. 9]

Table 5: Slender chimney: list of testing sequence

Building specimen	Test name	Test ID	Condition	Typology
EUC-BUILD-8.1	SC1-50%	9	Uncracked	8.1-SC-9
	SC1-100%	12	Uncracked	8.1-SC-12
	SC1-150%	16	Uncracked	8.1-SC-16
	SC2-25%	22	Cracked	8.1-SC-22
	SC2-50%	24	Cracked	8.1-SC-24
	SC2-75%	28	Cracked	8.1-SC-28
	SC2-100%	30	Cracked	8.1-SC-30
	SC2-150%	36	Cracked	8.1-SC-36
	SC2-200%	41	Cracked	8.1-SC-41
EUC-BUILD-8.2	SC1-50%	6	Uncracked	8.2-SC-6
	SC1-100%	9	Uncracked	8.2-SC-9
	SC1-150%	13	Uncracked	8.2-SC-13
	SC2-25%	18	Uncracked	8.2-SC-18
	SC2-50%	21	Uncracked	8.2-SC-21
	SC2-75%	28	Uncracked	8.2-SC-28
	SC2-100%	30	Uncracked	8.2-SC-30
	SC2-150%	32	Cracked	8.2-SC-32
	SC2-200%	34	Cracked	8.2-SC-34
EUC-BUILD-8.3	SC1-50%	6	Uncracked	8.3-SC-6
	SC1-100%	10	Uncracked	8.3-SC-10
	SC1-150%	16	Uncracked	8.3-SC-16
	SC2-50%	20	Cracked	8.3-SC-20
	SC2-75%	29	Cracked	8.3-SC-29
	SC2-100%	32	Cracked	8.3-SC-32
	SC2-150%	35	Cracked	8.3-SC-35
	SC2-200%	39	Cracked	8.3-SC-39

4.1.3 South Parapet

The South parapet wall was 0.84 m high and 0.65 m wide. It was located at the South façade of each building specimen [4, 5]. The location of the South parapet on the first-floor plan is shown in Figure 12. A closer view of the South parapet is shown in Figure 13.

The South parapet collapsed in two out of the three shake-table experiments: during the SC2-150% test in EUC-BUILD-8.1; and during the SC2-200% test in EUC-BUILD-8.2.

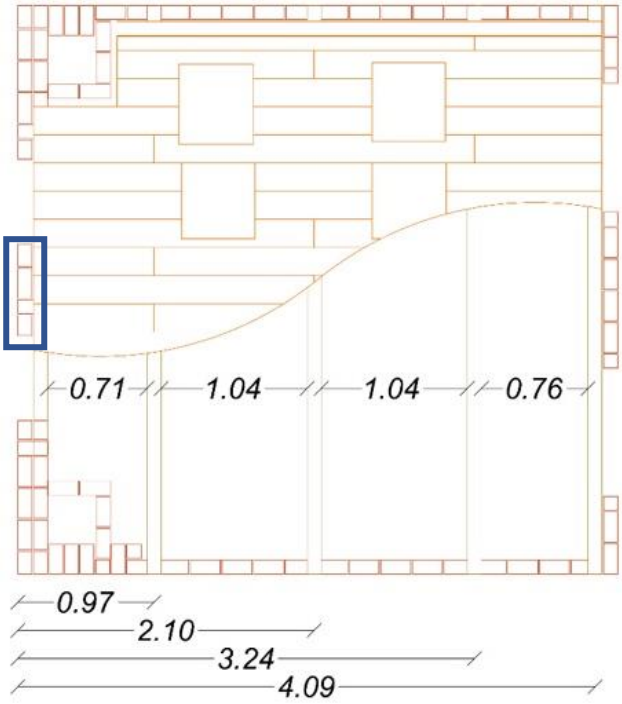

Figure 14: First-floor plan of the building prototype: location of the South parapet [4, p. 5]

Figure 15: Parapet on the South building façade [4, p. 9]

Table 6: South parapet: list of testing sequence

Building specimen	Test name	Test ID	Condition	Typology
EUC-BUILD-8.1	SC1-50%	9	Uncracked	8.1-SP-9
	SC1-100%	12	Uncracked	8.1-SP-12
	SC1-150%	16	Uncracked	8.1-SP-16
	SC2-25%	22	Uncracked	8.1-SP-22
	SC2-50%	24	Uncracked	8.1-SP-24
	SC2-75%	28	Cracked	8.1-SP-28
	SC2-100%	30	Cracked	8.1-SP-30
	SC2-150%	36	**COLLAPSED**	8.1-SP-36
	SC2-200%	41	**COLLAPSED**	8.1-SP-41
EUC-BUILD-8.2	SC1-50%	6	Cracked	8.2-SP-6
	SC1-100%	9	Cracked	8.2-SP-9
	SC1-150%	13	Cracked	8.2-SP-13
	SC2-25%	18	Cracked	8.2-SP-18
	SC2-50%	21	Cracked	8.2-SP-21
	SC2-75%	28	Cracked	8.2-SP-28
	SC2-100%	30	Cracked	8.2-SP-30
	SC2-150%	32	Cracked	8.2-SP-32
	SC2-200%	34	**COLLAPSED**	8.2-SP-34
EUC-BUILD-8.3	SC1-50%	6	Uncracked	8.3-SP-6
	SC1-100%	10	Uncracked	8.3-SP-10
	SC1-150%	16	Uncracked	8.3-SP-16
	SC2-50%	20	Uncracked	8.3-SP-20
	SC2-75%	29	Cracked	8.3-SP-29
	SC2-100%	32	Cracked	8.3-SP-32
	SC2-150%	35	Cracked	8.3-SP-35
	SC2-200%	39	Cracked	8.3-SP-39

4.1.4 East and West Parapets

The fourth and fifth building components to be considered were the East and West parapets. They were both parapet walls with a height of 0.66 m and a width of 1.63 m [4, 5]. Table 7 lists more information regarding the condition and short name of the East and West parapet tests. Figure 16 shows the location of both components on the first-floor plan, while Figure 17 shows the East parapet in a closer view.

As can be noticed in Table 7, the East parapet shows no structural damage during test sequences EUC-BUILD-8.1 and EUC-BUILD-8.2, which is reasonable, given that there was no excitation in the direction perpendicular to the plane of the wall. Cracks only occurred under shaking at SC2-50% in the EUC-BUILD-8.3 experiment. This happened due to the presence of the horizontal Y-component of motion in the East-West direction of building EUC-BUILD-8.3. The West parapet wall did not undergo any structural damage throughout the different tests.

Figure 16: First-floor plan of the building prototype: location of the East (blue box) and West parapet walls (green box) [4, p. 5]

Figure 17: Parapet wall on the East building façade [4, p. 9]

Table 7: East and West parapet walls: list of testing sequences

Building specimens	Test name	Test ID	East parapet		West parapet	
			Condition	Typology	Condition	Typology
EUC-BUILD-8.1	SC1-50%	9	Uncracked	8.1-EP-9	Uncracked	8.1-WP-9
	SC1-100%	12	Uncracked	8.1-EP-12	Uncracked	8.1-WP-12
	SC1-150%	16	Uncracked	8.1-EP-16	Uncracked	8.1-WP-16
	SC2-25%	22	Uncracked	8.1-EP-22	Uncracked	8.1-WP-22
	SC2-50%	24	Uncracked	8.1-EP-24	Uncracked	8.1-WP-24
	SC2-75%	28	Uncracked	8.1-EP-28	Uncracked	8.1-WP-28
	SC2-100%	30	Uncracked	8.1-EP-30	Uncracked	8.1-WP-30
	SC2-150%	36	Uncracked	8.1-EP-36	Uncracked	8.1-WP-36
	SC2-200%	41	Uncracked	8.1-EP-41	Uncracked	8.1-WP-41
EUC-BUILD-8.2	SC1-50%	6	Uncracked	8.2-EP-6	Uncracked	8.2-WP-6
	SC1-100%	9	Uncracked	8.2-EP-9	Uncracked	8.2-WP-9
	SC1-150%	13	Uncracked	8.2-EP-13	Uncracked	8.2-WP-13
	SC2-25%	18	Uncracked	8.2-EP-18	Uncracked	8.2-WP-18
	SC2-50%	21	Uncracked	8.2-EP-21	Uncracked	8.2-WP-21
	SC2-75%	28	Uncracked	8.2-EP-28	Uncracked	8.2-WP-28
	SC2-100%	30	Uncracked	8.2-EP-30	Uncracked	8.2-WP-30
	SC2-150%	32	Uncracked	8.2-EP-32	Uncracked	8.2-WP-32
	SC2-200%	34	Uncracked	8.2-EP-34	Uncracked	8.2-WP-34
EUC-BUILD-8.3	SC1-50%	6	Uncracked	8.3-EP-6	Uncracked	8.3-WP-6
	SC1-100%	10	Uncracked	8.3-EP-10	Uncracked	8.3-WP-10
	SC1-150%	16	Uncracked	8.3-EP-16	Uncracked	8.3-WP-16
	SC2-50%	20	Cracked	8.3-EP-20	Uncracked	8.3-WP-20
	SC2-75%	29	Cracked	8.3-EP-29	Uncracked	8.3-WP-29
	SC2-100%	32	Cracked	8.3-EP-32	Uncracked	8.3-WP-32
	SC2-150%	35	Cracked	8.3-EP-35	Uncracked	8.3-WP-35
	SC2-200%	39	Cracked	8.3-EP-39	Uncracked	8.3-WP-39

4.2 Numerical Simulation of Shake-Table Tests

The simulation of the shake-table experiments was performed employing the seismic analysis programme named *Trilly*. This is a set of Matlab routines, developed by the Masonry Structures research group of the University of Pavia, to analyse the dynamic response of local URM mechanisms through simplified SDOF systems. This section describes the various functions of the software and the calibration procedure against the experimental results.

4.2.1 Calibration Process: Identification of Variable Model Parameters

To simulate the experimental response of the URM building components throughout the testing sequence, some of the parameters that affect the most their dynamic response were calibrated through an iterative procedure. A distinction was made between the response of the elements at their cracked and uncracked condition.

Firstly, the shake-table tests for which the URM elements were cracked were simulated. A series of numerical simulations of each test were performed by considering a set of combinations of five parameters that varied. These varying input parameters are listed in Table 8. The first parameter, the wall height h, affects the mass m of the wall, and therefore also the weight W. In turn, the wall mass affects the force and displacement associated to the rigid linear relationship, i.e. F_0 and u_{ins}. Apart from that, it also influences the CR, and the effective mass m'. The second variable was a_1, which is the factor that defines the u_1 displacement and the stiffness of the cracked element. The third considered variable, a_3, determined the u_3 displacement, which is the lateral displacement capacity of the cracked overturning element. The fourth variable was *CorrCoeff*, which stands for the correction coefficient of the analytically computed CR. The analytically calculated CR is multiplied with the correction coefficient to account for the continuous energy dissipation, occurring due to the flexural response of the wall and the deformation of the rocking interfaces [14]. Finally, in the case of a trilinear elastic model of the force-displacement relationship, the $F_{0,Ratio}$, which is the ratio between F_0 and F_y, was also varied.

Table 8: Variable quantities considered in the simulation of the experimental dynamic response of the elements in the post-crack phase

Variable	Description
h	Wall height; it affects quantities like i) weight; ii) $u_{ins,}$; iii) F_0
a_1	Coefficient defining u_1 through Equation *(15)*: $u_1 = a_1 \cdot u_{ins}$.
a_3	Coefficient defining u_3 through Equation *(16)*: $u_3 = a_3 \cdot u_{ins}$.
CorrCoeff	Correction factor for the coefficient of restitution (CR)
$F_{0,Ratio}$	Ratio (also symbolled by b_1) between F_0 and F_y related with the Equation (18): $F_y = b_1 \cdot F_0$. Applicable only in the case of the trilinear elastic idealisation of the force-displacement relationship.

Afterwards, the tests for which the elements remained uncracked were simulated. Uncracked components do not show a rocking behaviour but remain linear elastic, moving on the force-displacement response branch F_{cr}-u_{cr}. As long as they remain uncracked an elastic damping acts on the URM components.

The first one of this set of varying input parameters was the wall height h, which influences the mass and thus the weight of the examined non-structural component. It also affects the cracking

displacement and force, u_{cr} and F_{cr}, which are involved in Equations (6) and (7). The second parameter was the elastic damping ratio *damp_el*, which is the damping acting on the linear elastic response phase [19]. The third varying parameter was the masonry Young's modulus in compression, E_{m1}, which is involved in the calculation of the cracked displacement u_{cr}. The fourth parameter that was varied during the numerical simulation of the dynamic response of the uncracked components was the masonry flexural strength f_w, which determines the bending moment capacity of the masonry component. The parameter f_w affects directly the lateral force that causes cracking, F_{cr}. All these parameters, apart from the elastic damping ratio, affect the stiffness (i.e. the slope) of the uncracked linear-elastic branch of the force-displacement relationship by altering F_{cr} and u_{cr}.

Table 9: Variable quantities considered in the simulation of the experimental dynamic response of the elements in the pre-crack phase

Variable parameter	Description
h	Wall height; it affects quantities like i) weight; ii) $u_{cr,}$; iii) F_{cr}
damp_el	Elastic damping ratio; it takes a constant value
E_{m1}	Masonry Young's modulus; it is involved into the computation of u_{cr}
f_w	Masonry flexural strength; it affects F_{cr}

4.2.2 Calibration Process: Constant Model Parameters

The geometric properties of the URM elements, which remained unchanged in the parametric analysis performed for the calibration of the models, are listed in Table 10. These properties were involved in the calculation of the mass, weight, cross-section and rotational moment of inertia, which are in turn used for the computation of F_{cr}, u_{cr}, and the analytical CR, e_{an}. The hollow section thickness, termed *sch* in *Trilly* (see user manual [19]), is used to calculate the net cross-section of the chimney.

Table 10: Geometric properties of the modelled URM building components

Properties	Gable wall	Slender chimney	South parapet	East parapet	West parapet
Width *w* [m]	4.04	0.54	0.65	1.63	1.63
Thickness *b* [m]	0.10	0.54	0.10	0.10	0.10
Hollow section thickness *sch* [m]	-	0.10	-	-	-

Other parameters that need to be defined for the non-linear time-history analyses are: i) the type of force-displacement relationship; ii) the type of damping model to be used; and iii) the type of rocking behaviour, meaning one- or two-side rocking. As shown in Table 11, the force-displacement behaviour of the slender chimney was modelled through a trilinear elastic response curve. Instead, the response of the gable and parapet walls was modelled using bilinear force-displacement relationships. The selected damping type was the constant damping coefficient (CDC) for all building components. All elements were modelled as two-side rocking elements, but for the gable wall, an infinitely elastic behaviour was imposed for response in the quadrant of negative displacements, meaning towards the side of the timber truss, which was not perfectly rigid to force the gable into perfect one-side rocking response.

Table 11: Other model parameters considered in the response-history analyses

Parameters	Gable wall	Slender chimney	South parapet	East parapet	West parapet
Idealisation	Bilinear	Trilinear	Bilinear	Bilinear	Bilinear
Damping type	CDC	CDC	CDC	CDC	CDC
Rocking type	Two-sided	Two-sided	Two-sided	Two-sided	Two-sided

It should also be noted that in the calculations, the overburden force *O* was always equal to zero because there is no additional axial load acting on the top of the components.

4.2.3 Consideration of Vertical Accelerations

Where vertical input accelerations were also applied (i.e. in experiments EUC-BUILD-8.2 and EUC-BUILD-8.3), the restoring force F_0 (i.e. the force needed to trigger the rocking motion) was calculated at every step of the analysis. This happens because the force F_0 is a function of the weight of the analysed URM component, which varies as vertical accelerations acting on the element vary. As a consequence, the force F_0 increases for upward accelerations, and decreases in the case of downward accelerations. This vector of varying restoring force F_{02} is calculated for every step of the analysis using Equation (36) for the parapet walls and slender chimney, and Equation (37) for the gable wall. As it can be seen in these equations, F_{02} is calculated in the same way as F_0, with the only difference found in accounting for the variation of the gravity accelerations. In these equations, a_v is the vertical acceleration.

$$F_{02} = \frac{(9.81 + a_v) \cdot m \cdot \frac{t}{2}}{\frac{h}{2}} \tag{36}$$

$$F_{02,GW} = \frac{(9.81 + a_v) \cdot m \cdot \frac{t}{2}}{\frac{h}{3}} \tag{37}$$

The effective mass m' of the system is defined with a value of 4/3 of the total mass of the component, based on Table 1. Together with this, the elastic stiffness is calculated based on Equation (38). The initial elastic circular frequency is also calculated in this phase, using Equation (39). Afterwards, the starting vectors of the dynamic analysis are set. In the case of a cracked component, the damping coefficient for the chosen damping type is now calculated based on Equations (25), (27), and (28).

$$K_{el} = \frac{F_{cr}}{u_{cr}} \tag{38}$$

$$\omega_{el} = \sqrt{\frac{K_{el}}{m'}} \tag{39}$$

In the following sections, the numerical responses of the building components are illustrated in the form of two graphs: i) normalised displacement (u/u_{ins}) versus time step; and ii) acceleration at the centre of mass a_G versus normalised displacement (u/u_{ins}). These figures will be discussed in more detail in the following chapter.

5 Discussion of Analysis Results

This chapter presents the results of the seismic response analysis. For each building component, two plots are provided: i) the displacement response time-series, in terms of normalised displacement (u/u_{ins}) versus time step; ii) the hysteretic response curve, in terms of the acceleration at the centre of mass (a_G) of the element versus the normalised displacement (u/u_{ins}).

5.1 Analysis of Cracked Components

The following sections discuss the simulations of the tests in which the components were cracked. For both EUC-BUILD-8.1 and EUC-BUILD-8.2 buildings, the responses of the East and West parapet walls are not simulated. This is because these building specimens were not excited in the East-West direction, as such the two parapets did not exhibit any rocking response.

5.1.1 EUC-BUILD-8.1

5.1.1.1 Gable Wall

The gable wall of the EUC-BUILD-8.1 building specimen showed structural damage starting from test 8.1-GW-24 onwards. The retrofitting interventions were implemented at 8.1-GW-30, after which there was no need to simulate any seismic response due to the rigid behaviour of the structural interventions. Figure 18 (A) and (B), show the simulations for test 8.1-GW-24 and 8.1-GW-28, respectively.

In both tests, a good agreement is noticed between the numerical and experimental response, especially in test 8.1-GW-24. Test 8.1-GW-28 shows a good capture of the first peak displacement but tends to overestimate the duration of this oscillation. There is a difference in numerical and experimental response after the peak for both simulations, which can be explained by the fact that the calibration was performed in the four-second window around the peak displacement response.

Table 12 lists the values of the four input parameters of the models that best-capture the behaviour of the gable wall in the 8.1-GW tests. The height of the gable wall varies between 2.231 m and 2.328 m, which means 1.15 to 1.20 times the nominal height of the gable, which is 1.94 m. The a_1 resulted between 0.012 and 0.034, while a_3 was between 0.945 and 0.99. The correction coefficient for the analytical CR ranges between 0.25 and 0.38. The ranges of values for all calibrated parameters are summarised in Table 13.

Table 12: Calibrated values for the input model parameters of the cracked gable for the 8.1-GW tests

Test name	Height h [m] h_{nom} = 1.94 m	a_1	a_3	*CorrCoeff*
8.1-GW-24	2.328	0.034	0.945	0.250
8.1-GW-28	2.231	0.012	0.990	0.380

Table 13: Range of calibrated input model parameters of the cracked gable for the 8.1-GW tests

Input parameter	Lower bound	Upper bound
Height h [m]	2.231	2.328
a_1	0.012	0.034
a_3	0.945	0.990
CorrCoeff	0.250	0.380

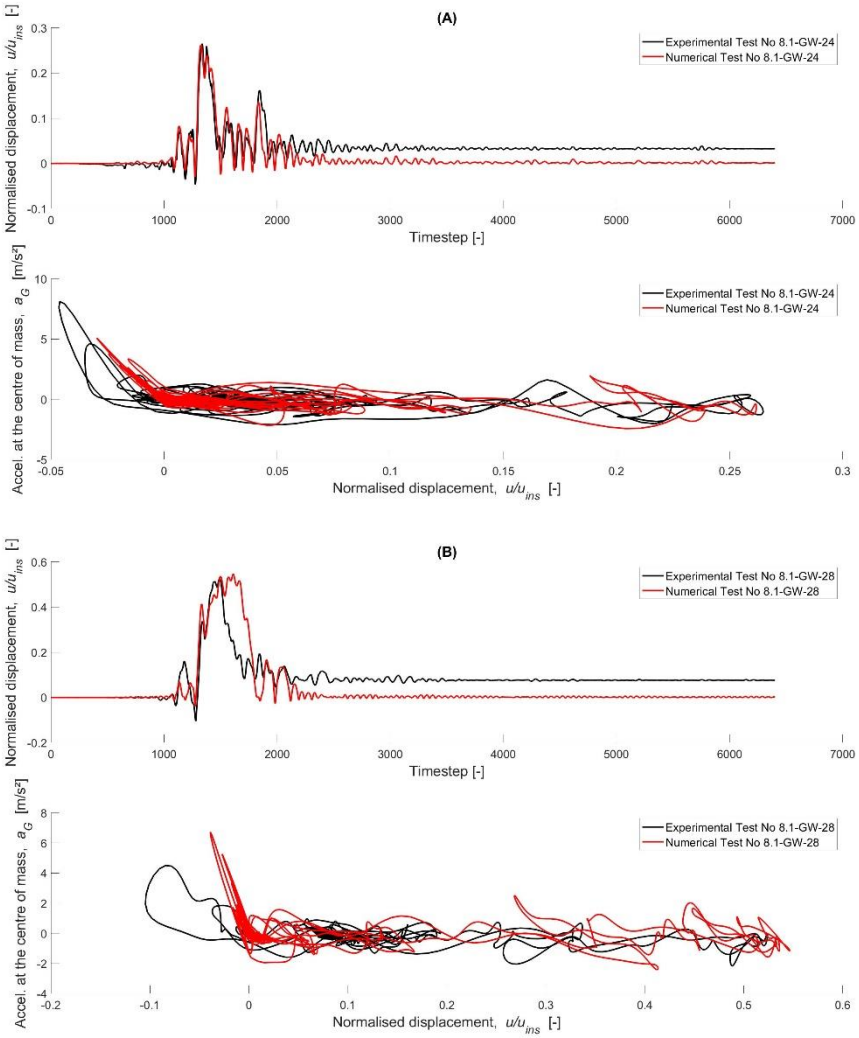

Figure 18: Comparison between the experimental and numerical response of the gable wall of building specimen EUC-BUILD-8.1 during tests: (A) 8.1-GW-22; and (B) 8.1-GW-24

5.1.1.2 Slender Chimney

The slender chimney showed cracks from test 8.1-SC-22 until the end of the sequence, 8.1-SC-41. The simulations of tests 8.1-SC-22, 8.1-SC-24, and 8.1-SC-28 are shown in Figure 19, while the simulations of 8.1-SC-30, 8.1-SC-36, and 8.1-SC-41 are illustrated in Figure 20. Overall, the numerical and experimental responses show a good agreement, especially for tests 8.1-SC-28, 8.1-SC-30, and 8.1-SC-36, despite an occasional small underestimation of the peak values.

It is worth noting that in case of test 8.1-SC-22, the two peak values between the time steps 1200 and 1500 are slightly underestimated, while the smaller peaks that follow were overestimated. On the contrary, test 8.1-SC-41 was captured accurately in the first ten peak values; however, the peak at time step around 2500 was underestimated. The numerical prediction also shows a shift in the oscillation frequency of the last four peak responses. Table 14 shows the values of the calibrated input model parameters for this testing sequence. Table 15 shows the ranges of values within which these parameters vary.

Table 14: Calibrated values for the input model parameters of the cracked chimney for the 8.1-SC tests

Test name	**Height h [m]** h_{nom} **= 2.04 m**	a_1	a_3	***CorrCoeff***	$F_{0,Ratio}$
8.1-SC-22	1.734	0.007	0.900	0.175	0.60
8.1-SC-24	2.244	0.011	0.808	0.525	0.75
8.1-SC-28	2.142	0.001	0.800	0.700	0.60
8.1-SC-30	2.142	0.018	0.850	0.595	0.70
8.1-SC-36	2.142	0.024	0.850	0.630	0.50
8.1-SC-41	2.448	0.034	0.850	0.980	0.80

Table 15: Ranges of the calibrated input model parameters of the cracked chimney for the 8.1-SC tests

Input parameter	**Lower bound**	**Upper bound**
Height h [m]	1.734	2.488
a_1	0.001	0.034
a_3	0.800	0.900
CorrCoeff	0.175	0.980
$F_{0,Ratio}$	0.50	0.80

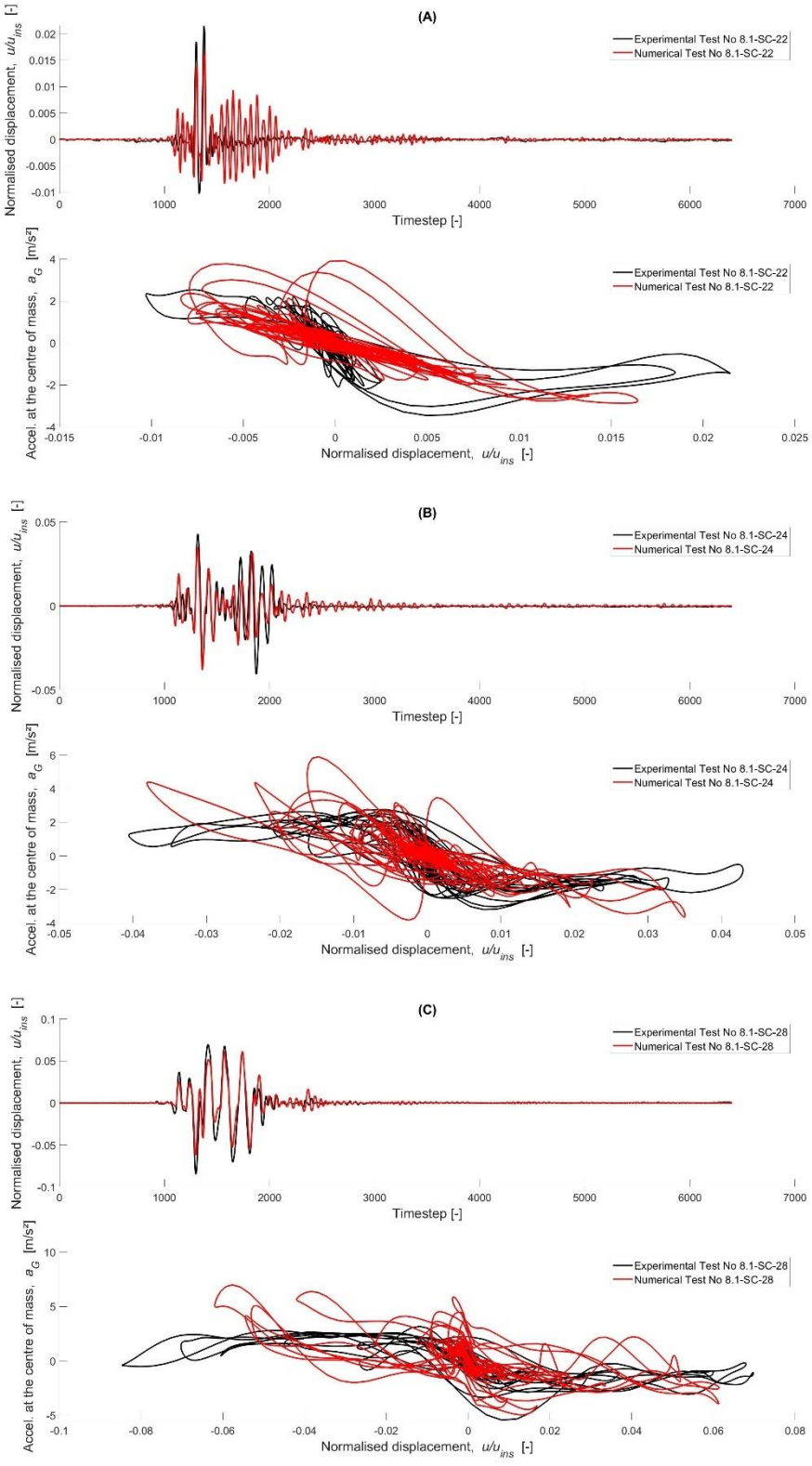

Figure 19: Comparison between the experimental and numerical responses of the slender chimney in the EUC-BUILD-8.1 tests: (A) 8.1-SC-22; (B) 8.1-SC-24; and (C) 8.1-SC-28

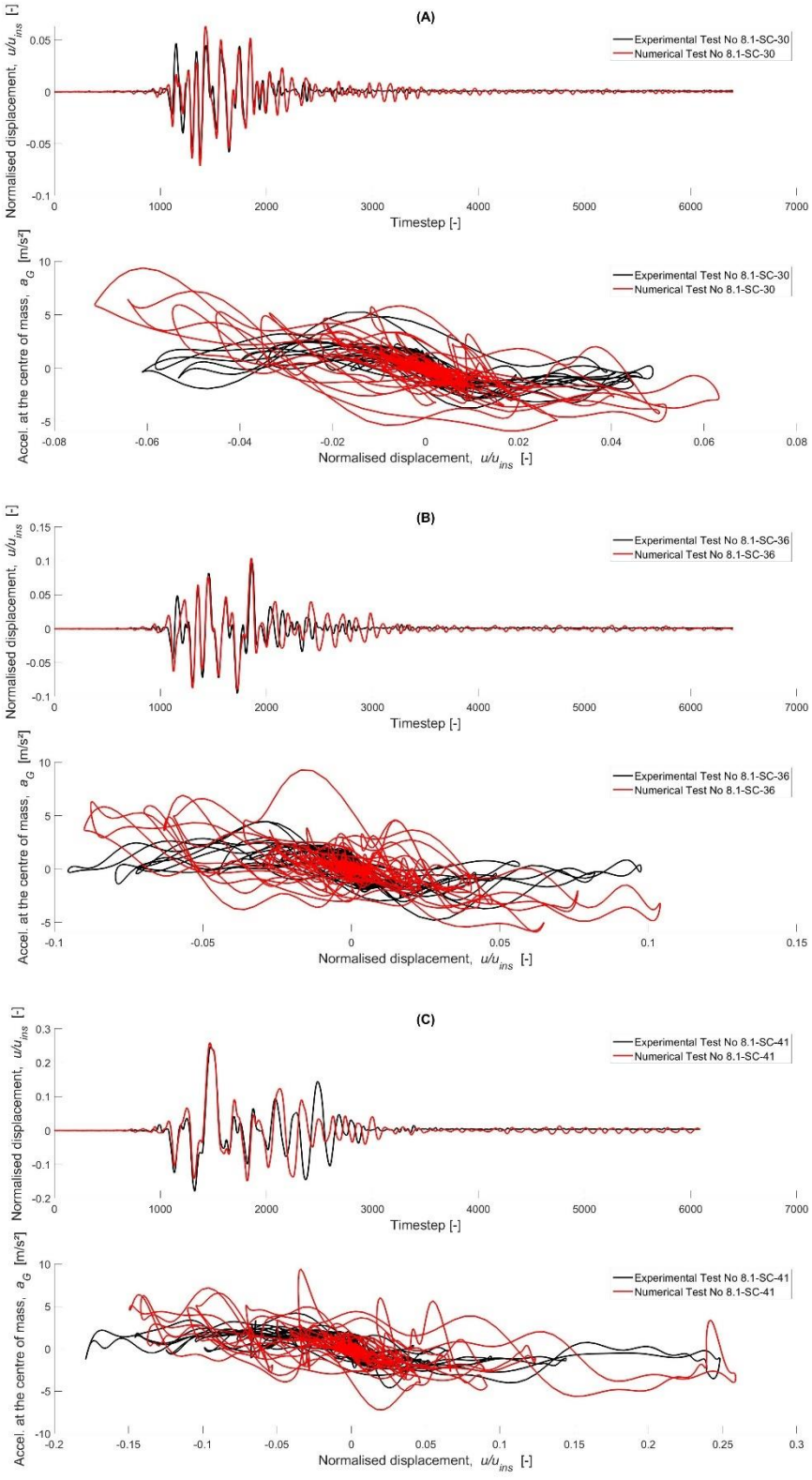

Figure 20: Comparison between the experimental and numerical responses of the slender chimney in the EUC-BUILD-8.1 tests: (A) 8.1-SC-30; (B) 8.1-SC-36; and (C) 8.1-SC-41

5.1.1.3 South Parapet

In the case of the South parapet, cracking occurred during the test 8.1-SP-28; the parapet collapsed during the test 8.1-SP-36. The latter test and the test 8.1-SP-41 were not simulated, since the input accelerations at the base of the parapet were not available: the accelerometer that was initially mounted there was removed in order to secure it from damage due to imminent collapse of the parapet. Figure 21 (A) shows that the simulation of test 8.1-SP-28 was not very accurate. The positive and negative peak located at time step around 1500 are underestimated on behalf of the numerical simulation.

Figure 21 (B) shows the simulation of test 8.1-SP-30. Experimental and numerical responses in the time window including the first peaks, i.e. between the time steps 1000 and 2000, show a good agreement. The rest of the numerical simulation time history, i.e. after the time step 2000, shows a slight overestimation of the normalised displacement. Table 16 and Table 17, list the calibrated values for the input model parameters, respectively.

Table 16: Calibrated values for the input model parameters of the cracked South parapet for the 8.1-SP tests

Test name	**Height *h* [m]** h_{nom} **= 0.84 m**	a_1	a_3	***CorrCoeff***
8.1-SP-28	0.672	0.026	0.893	0.800
8.1-SP-30	0.756	0.084	0.893	0.808

Table 17: Ranges of the calibrated input model parameters of the cracked South parapet for the 8.1-SP tests

Input parameter	**Lower bound**	**Upper bound**
Height *h* [m]	0.672	0.756
a_1	0.026	0.084
a_3	0.893	0.893
CorrCoeff	0.800	0.808

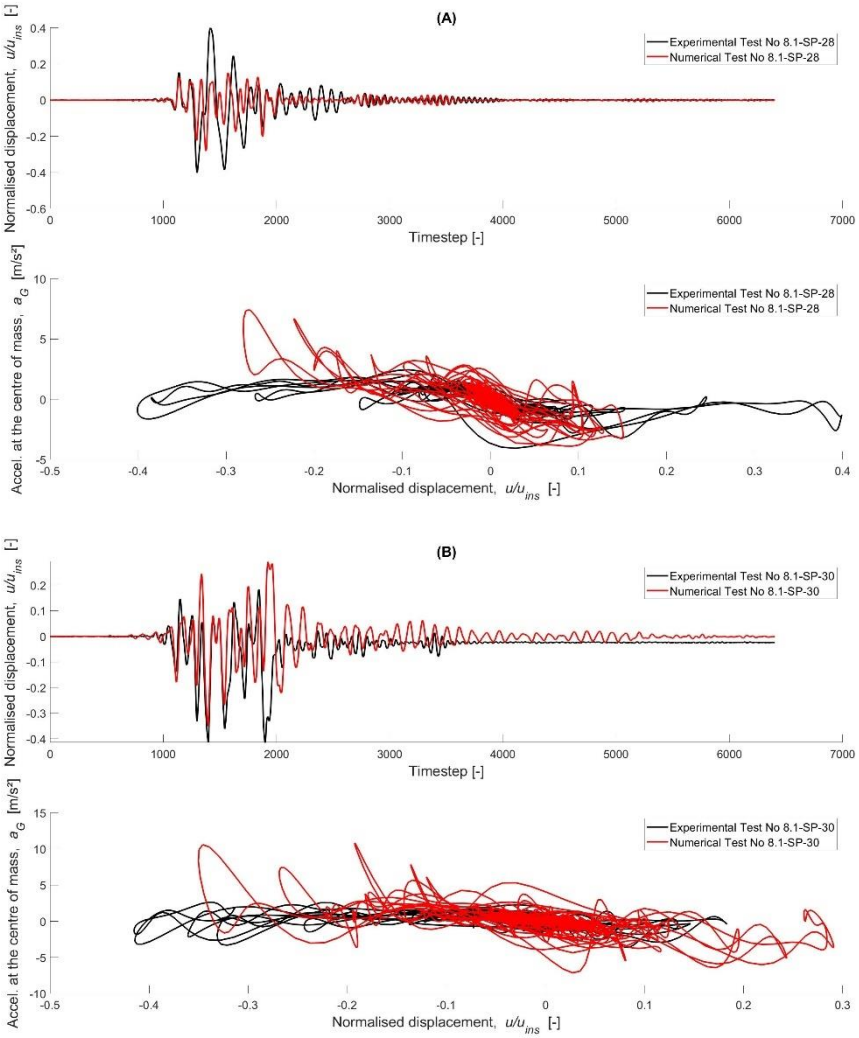

Figure 21: Comparison between the experimental and numerical responses of the South parapet in the EUC-BUILD-8.1 tests: (A) 8.1-SP-28; and (B) 8.1-SP-30

5.1.2 EUC-BUILD-8.2

5.1.2.1 Gable Wall

The gable wall of the EUC-BUILD-8.2 specimen had structural damage occurring from test 8.2-GW-9 onwards and was retrofitted after test 8.2-GW-21. The simulation of the four tests 8.2-GW-9, 8.2-GW-13, 8.2-GW-18, and 8.2-GW-21, are shown in Figure 22 (A) to (D), respectively. Overall, the numerical response tends to simulate the experimental response well. Primarily tests 8.2-GW-9 and 8.2-GW-18 show a good agreement between the experimental and numerical behaviour, despite the numerical response slightly underestimating the smaller peaks (around time step 1500) by a value of approximately 0.015 in terms of normalised displacement during test 8.2-GW-18 (Figure 22 (C)).

Figure 22 (B) shows the response of test 8.2-GW-13, where the experimental response is well simulated in the time window containing the first peaks, i.e. 1000 to 1200, and the final rocking motions of the component. There occurs an overestimation of the normalised displacement, showing a difference in value of 0.01, during the oscillations between time step 1700 and 2000.

In Table 18 and Table 19, it can be noted that the parameters possess an increase in range as compared to the 8.1-GW tests. This testing sequence, however, consists of double the number of tests, so the parameters have a higher chance of showing a deviating value.

Table 18: Calibrated values for the input model parameters of the cracked gable for the 8.2-GW tests

Test name	**Height h [m]** h_{nom} **= 1.94 m**	a_1	a_3	***CorrCoeff***
8.2-GW-9	1.649	0.015	1.000	0.220
8.2-GW-13	1.552	0.011	0.998	0.495
8.2-GW-18	1.552	0.030	0.900	0.195
8.2-GW-21	1.746	0.030	0.945	0.300

Table 19: Ranges of the calibrated input model parameters of the cracked gable for the 8.2-GW tests

Input parameter	**Lower bound**	**Upper bound**
Height h [m]	1.552	1.746
a_1	0.011	0.030
a_3	0.900	1.000
CorrCoeff	0.195	0.495

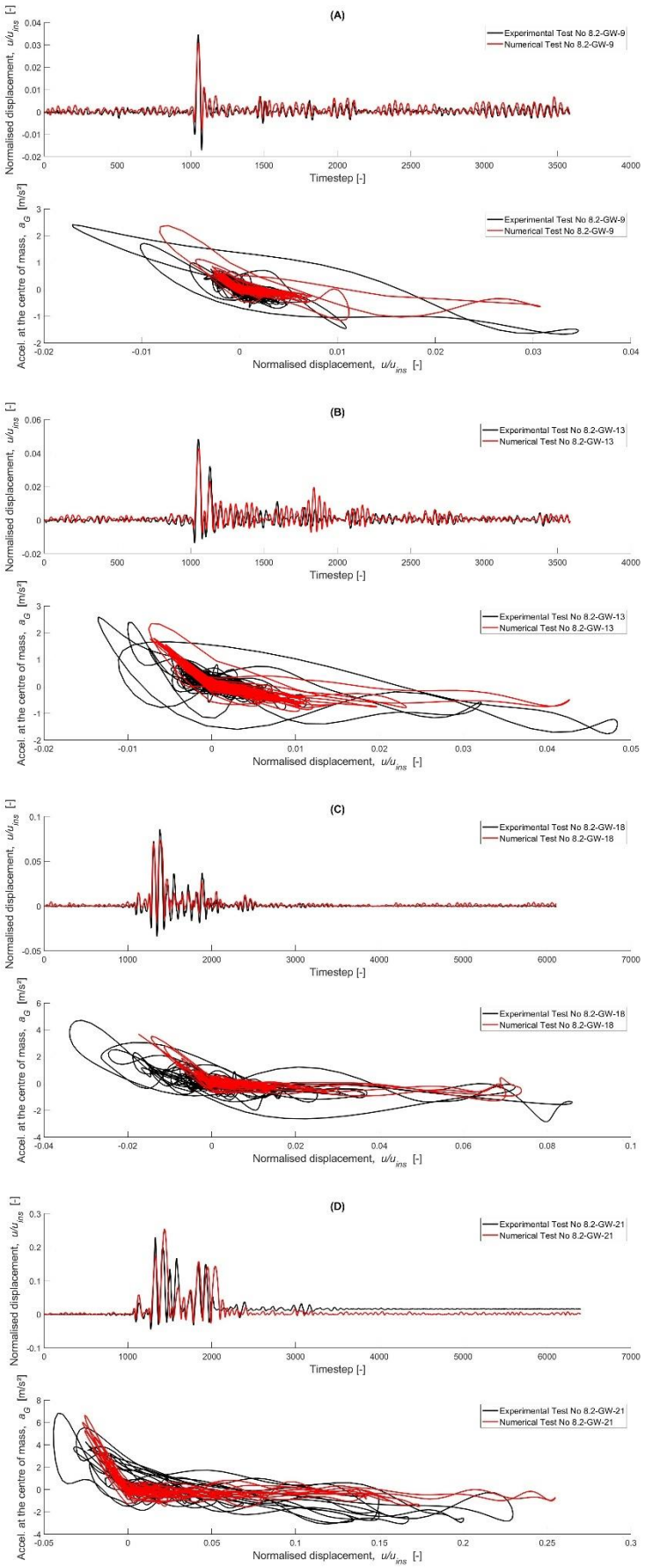

Figure 22: Comparison between the experimental and numerical responses of the gable wall in the EUC-BUILD-8.2 tests: (A) test 8.2-GW-9; (B) test 8.2-GW-13; (C) test 8.2-GW-18; and (D) test 8.2-GW-21

5.1.2.2 Slender Chimney

The EUC-BUILD-8.2 slender chimney has 8.2-SC-32 and 8.2-SC-34 simulated as cracked, which are shown in Figure 23. The numerical response does not manage to capture the experimental behaviour well for test 8.2-SC-32. First of all, the chimney shows an experimental negative shift of the entire component, a phenomenon that cannot be simulated by the analysis software. This results in the negative peak values being underestimated by values of 0.15 in terms of normalised displacement. The numerical simulation also neglects the final three experimentally recorded peaks and shows an excessive final oscillation of the component after time step 4000.

Table 20 shows the values of the input parameters for the numerical simulations. The correction coefficient for the analytical CR has a value of 1.05. In this case, extra attention should be put on the value of the corrected CR, as a CR value greater than one is not physically possible. In practice, this would mean that at each impact due to rocking of the element, the component would not dissipate energy, but absorb energy. Meaning the element would gain velocity during rocking. However, in this case, the corrected CR has been checked to have a value of 0.895.

Table 20: Calibrated values for the input model parameters of the cracked chimney for the 8.2-SC tests

Test name	**Height h [m]** h_{nom} **= 2.04 m**	a_1	a_3	***CorrCoeff***	$F_{0,Ratio}$
8.2-SC-32	1.632	0.024	0.850	1.050	0.90
8.2-SC-34	2.346	0.018	0.850	0.560	0.60

Table 21: Ranges of the calibrated input model parameters of the cracked chimney for the 8.2-SC tests

Input parameter	**Lower bound**	**Upper bound**
Height h [m]	1.632	2.346
a_1	0.018	0.024
a_3	0.850	0.850
CorrCoeff	0.560	1.050
$F_{0,Ratio}$	0.60	0.90

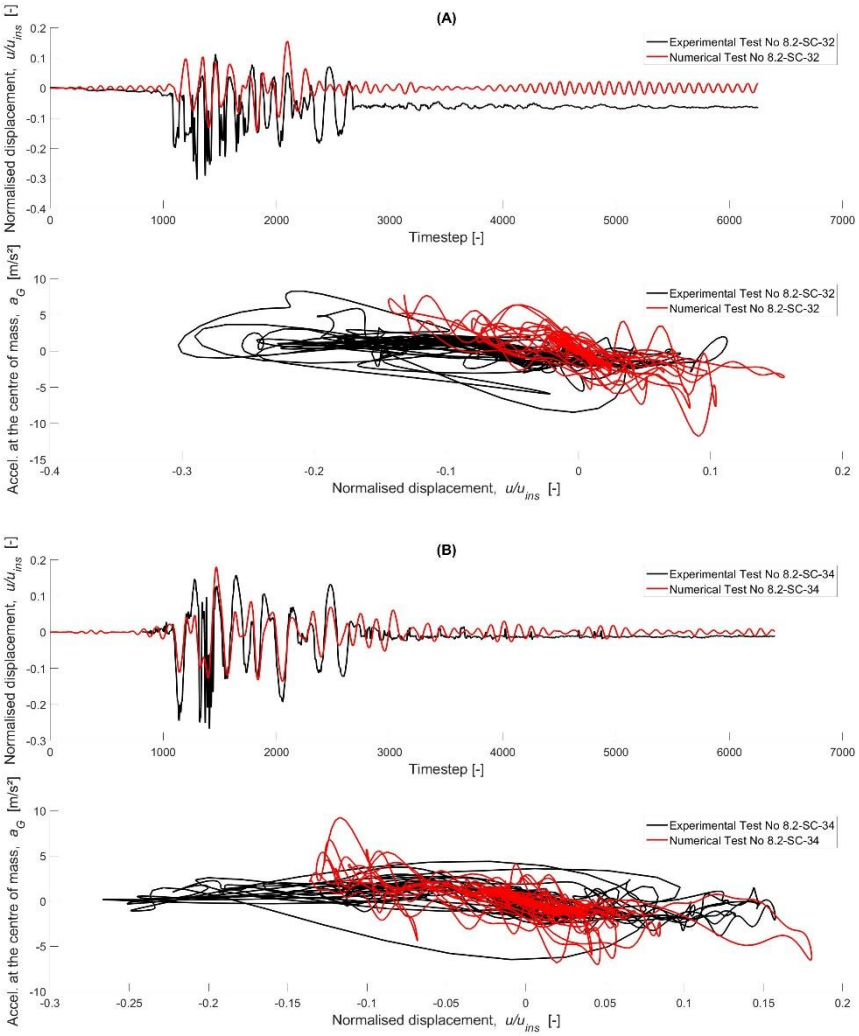

Figure 23: Comparison between the experimental and numerical responses of the slender chimney in the EUC-BUILD-8.2 tests: (A) 8.2-SC-32; and (B) 8.2-SC-34

5.1.2.3 South Parapet

The South parapet showed signs of structural damage in an early stage of the EUC-BUILD-8.2 building test sequence, with the first damage occurring during test 8.2-SP-9. The parapet collapsed during test 8.2-SP-34, meaning this test is not simulated numerically.

The collapse of the South parapet can be anticipated looking at test 8.2-SP-32, seen in Figure 25 (C). In this test, the parapet responds differently to the input accelerations than during the previous tests. It shows a series of continuous, oscillating displacements with a value of a 0.5-0.6 in terms of normalised displacement. This points to the component rocking with large oscillations, being close to collapse through overturning. The numerical simulation captures this response well, as well as the other, less constant behaviour of the South parapet.

Test 8.2-SP-9, 8.2-SP-18, and 8.2-SP-21 show satisfactory simulations of the experimental response, reproducing both the significant peaks, as the smaller peaks well. In the case of test 8.2-SP-13, the experimental response is simulated well, apart from the negative peak value, around time step 1100, being underestimated by a normalised displacement value of approximately 0.04.

The numerical simulation of test 8.2-SP-28 shows a good numerical response of both the initial and final behaviour. Four to five larger peaks situated in the time window between time step 1500 to 2000, however, are underestimated by normalised displacement values up to 0.2. For test 8.2-SP-30, the overall numerical response simulates the experimental response quite well, apart from the underestimation of specific negative peaks in the window between time step 1200 and 2500, and the overestimation of the final oscillations.

Table 22: Calibrated values for the input model parameters of the cracked South parapet for the 8.2-SP tests

Test name	**Height h [m]** h_{nom} **= 0.84 m**	a_1	a_3	***CorrCoeff***
8.2-SP-9	0.714	0.028	0.808	0.64
8.2-SP-13	0.714	0.024	0.850	0.56
8.2-SP-18	0.672	0.032	0.850	0.56
8.2-SP-21	0.714	0.024	0.893	0.76
8.2-SP-28	0.714	0.024	0.850	0.92
8.2-SP-30	0.756	0.084	0.940	0.84
8.2-SP-32	1.008	0.080	0.808	0.95

Table 23: Ranges of the calibrated input model parameters of the cracked South parapet for the 8.2-SP tests

Input parameter	**Lower bound**	**Upper bound**
Height h [m]	0.672	1.008
a_1	0.024	0.084
a_3	0.8075	0.893
CorrCoeff	0.56	0.95

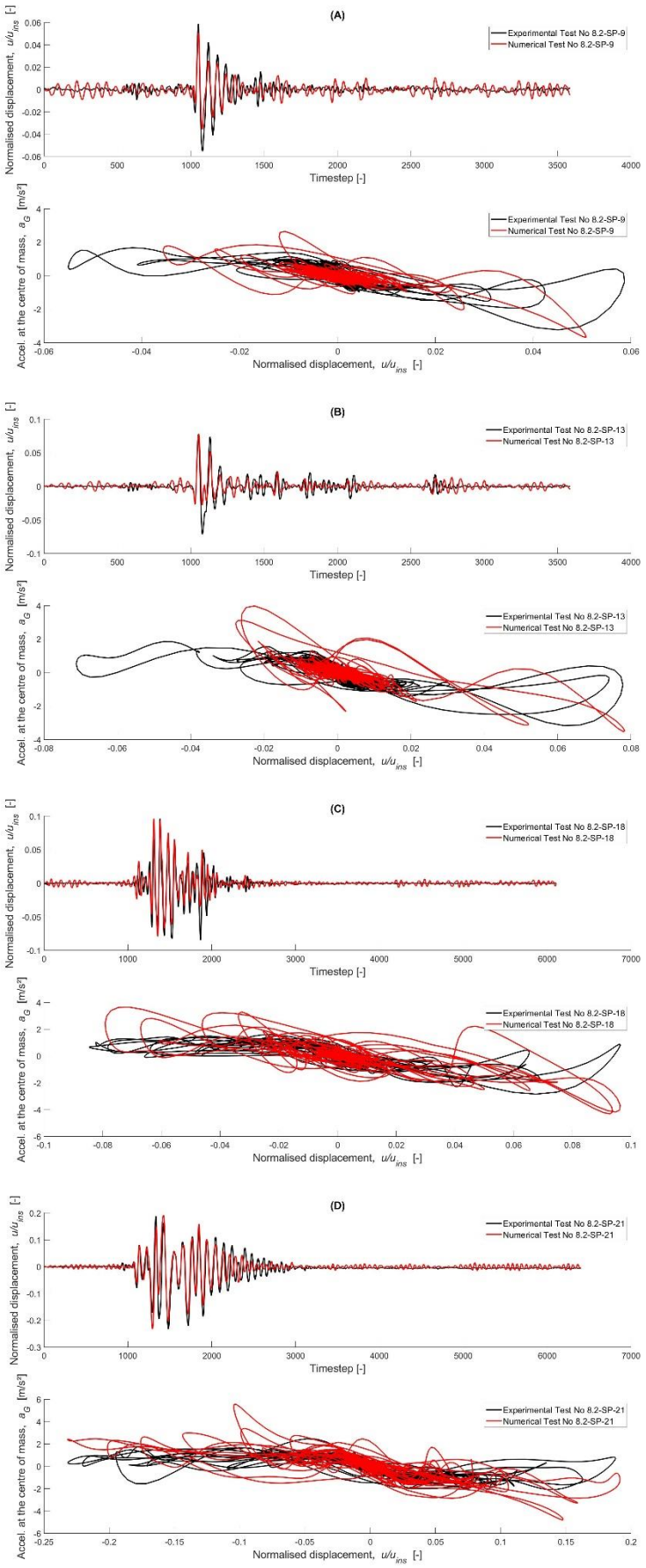

Figure 24: Comparison between the experimental and numerical responses of the South parapet in the EUC-BUILD-8.2 tests: (A) test 8.2-SP-9; (B) test 8.2-SP-13; (C) test 8.2-SP-18; and (D) test 8.2-SP-21

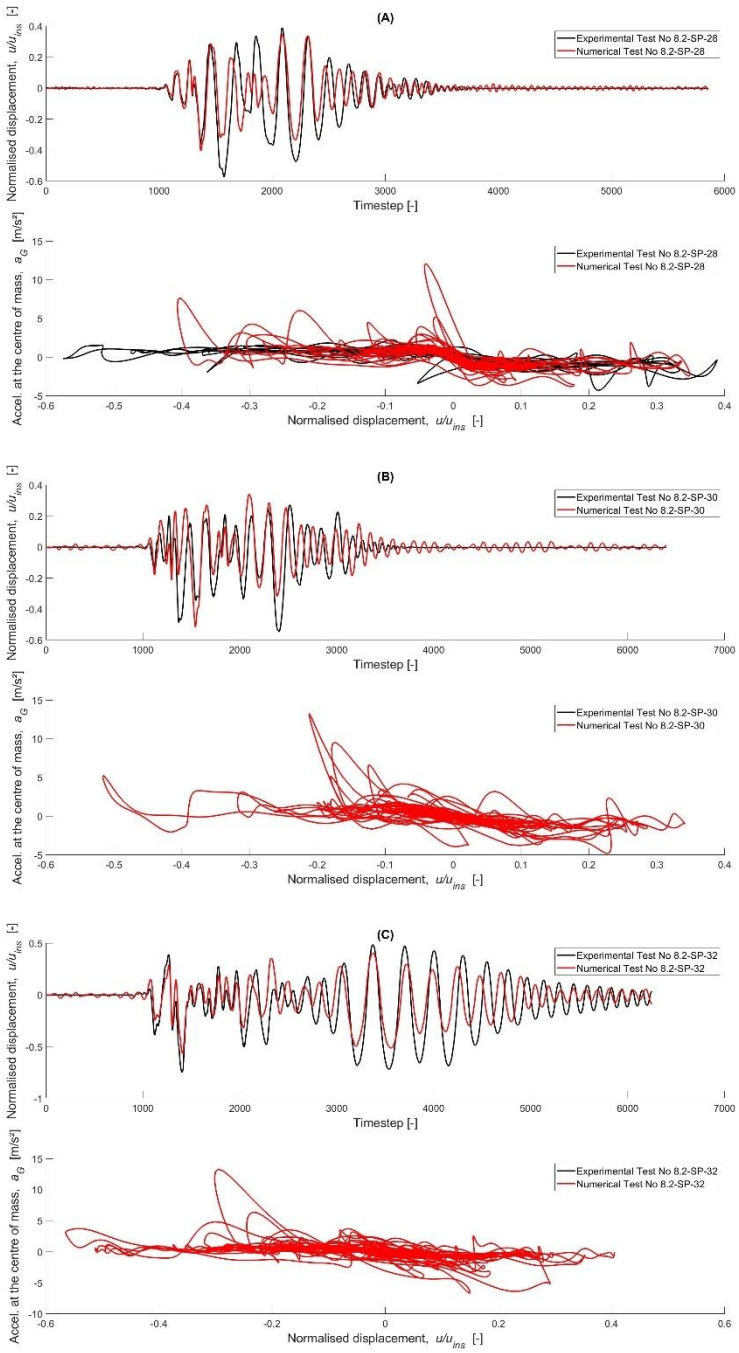

Figure 25: Comparison between the experimental and numerical responses of the South parapet in the EUC-BUILD-8.2 tests: (A) test 8.2-SP-28; (B) test 8.2-SP-30; and (C) test 8.2-SP-32

5.1.3 EUC-BUILD-8.3

5.1.3.1 Gable Wall

The gable wall of the EUC-BUILD-8.3 building specimen showed structural damage from the test 8.3-GW-10 onwards until being retrofitted at the test 8.3-GW-29. The simulations of this component in its cracked condition show satisfying results. The analysis software simulates the peak responses and the overall response quite well.

Only the simulation of test 9.3-GW-20 shows an overestimation of the values within the time window containing the smaller peaks that immediately follow the largest positive peak, i.e. between time step 1500 and 2000.

Table 24: Calibrated values for the input model parameters of the cracked gable wall for the 8.3-GW tests

Test name	Height h [m] h_{nom} = 1.94 m	a_1	a_3	*CorrCoeff*
8.3-GW-10	1.746	0.018	0.950	0.500
8.3-GW-16	1.649	0.020	0.998	0.385
8.3-GW-20	2.134	0.018	0.945	0.330

Table 25: Ranges of the calibrated input model parameters of the cracked gable wall for the 8.3-GW tests

Input parameter	Lower bound	Upper bound
Height h [m]	1.649	2.134
a_1	0.018	0.020
a_3	0.945	0.998
CorrCoeff	0.330	0.500

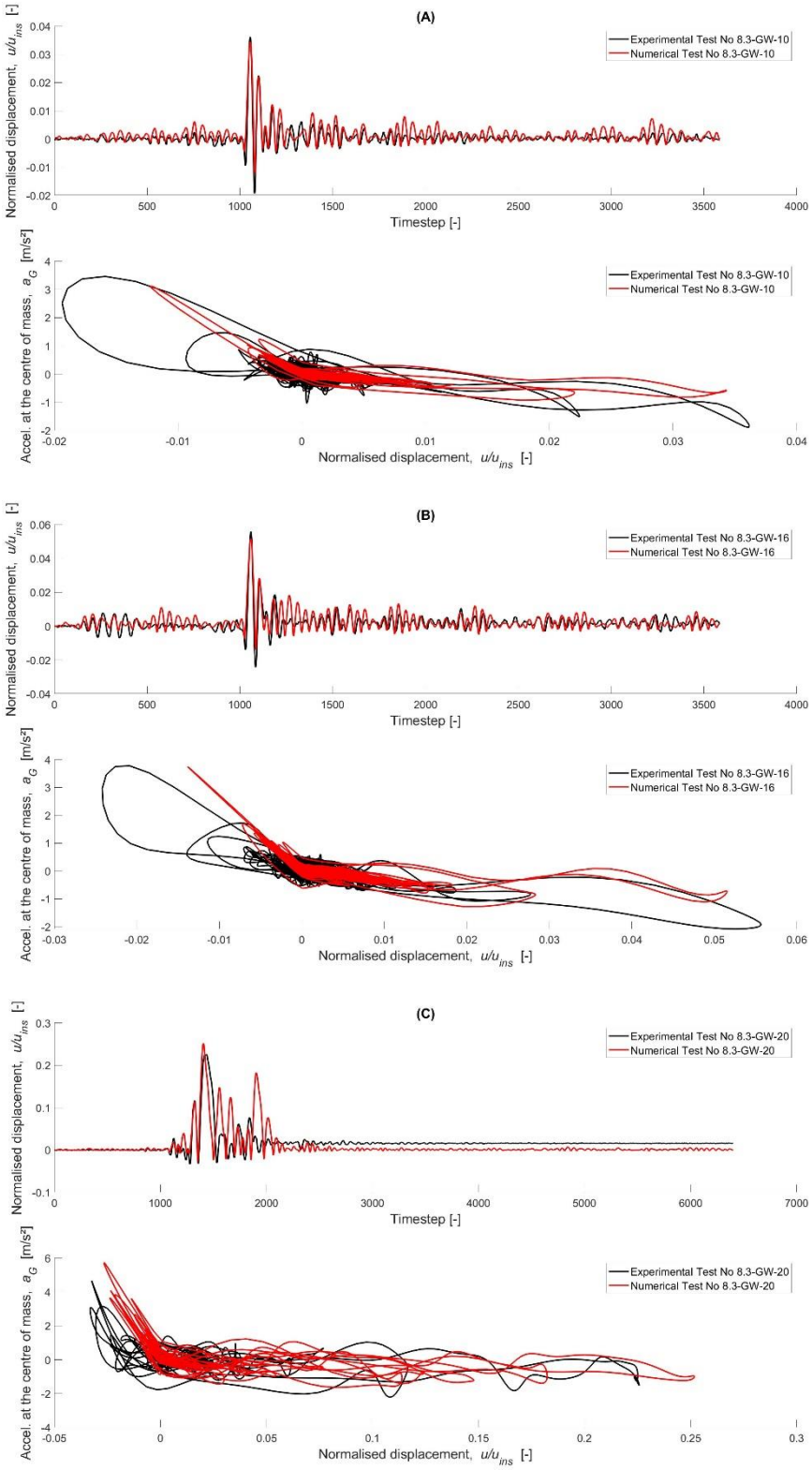

Figure 26: Comparison between the experimental and numerical responses of the gable wall in the EUC-BUILD-8.3 tests: (A) 8.3-GW-10; (B) 8.3-GW-16; and (C) 8.3-GW-20

5.1.3.2 Slender Chimney

The EUC-BUILD-8.3 slender chimney showed structural damage from test 8.3-SC-20 onwards. The numerical simulations of the component for this specific building specimen show satisfactory results. Over the different tests in the sequence, the numerical responses tend to replicate the experimental behaviour well, simulating the majority of peaks to almost identical values, as can be seen in Figure 27 and Figure 28.

Figure 28 (B) and (C), showcasing tests 8.3-SC-35 and 8.3-SC-38, respectively, show the trend that was previously seen at the gable walls. Due to the entire chimney that shifts, there is a difference in the normalised displacement between the numerical and experimental response due to the software only being able to simulate the rocking response, no absolute displacements. This forms, especially for test 8.3-SC-38, a distorted image. The peaks do not coincide for this test, due to the shift of the chimney being of significant value (around 0.1 normalised displacement). However, after taking a closer look, it can be noticed that if the two responses would both be located around the primary axis of zero normalised displacement, the peaks do not differ significantly in value.

Table 26: Calibrated values for the input model parameters of the cracked chimney for the 8.3-SC tests

Test name	**Height h [m]** h_{nom} **= 2.04 m**	a_1	a_3	***CorrCoeff***	$F_{0,Ratio}$
8.3-SC-20	1.632	0.010	0.850	0.805	0.90
8.3-SC-29	2.244	0.007	0.800	0.600	0.60
8.3-SC-32	1.632	0.033	0.893	1.015	0.90
8.3-SC-35	2.244	0.032	0.808	0.770	0.60
8.3-SC-38	2.142	0.022	0.808	0.770	0.55

Table 27: Ranges of the calibrated input model parameters of the cracked chimney for the 8.3-SC tests

Input parameter	**Lower bound**	**Upper bound**
Height h [m]	1.632	2.244
a_1	0.007	0.033
a_3	0.800	0.893
CorrCoeff	0.600	1.015
$F_{0,Ratio}$	0.55	0.90

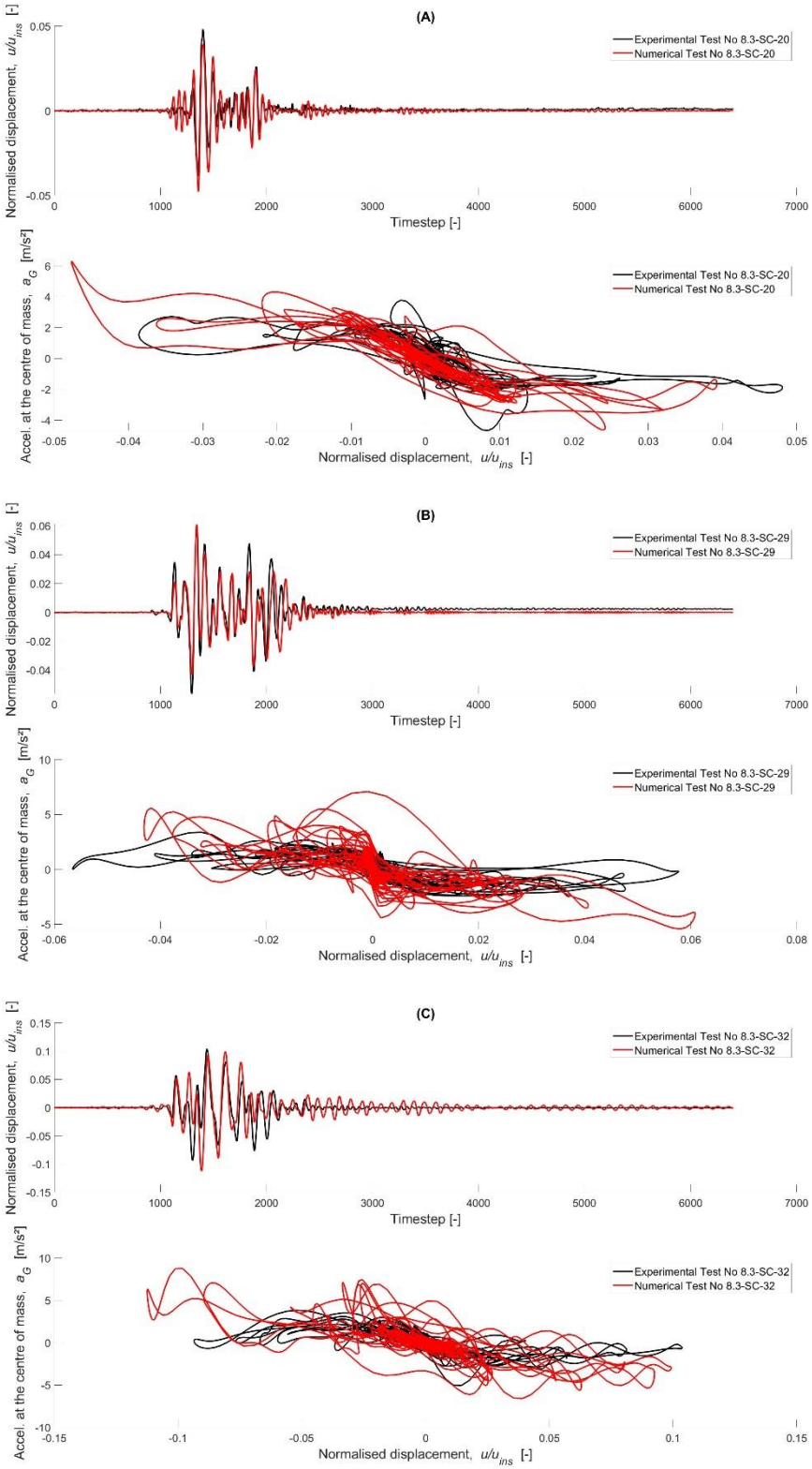

Figure 27: Comparison between the experimental and numerical responses of the slender chimney in the EUC-BUILD-8.3 tests: (A) test 8.3-SC-20; (B) test 8.3-SC-29; and (C) test 8.3-SC-32

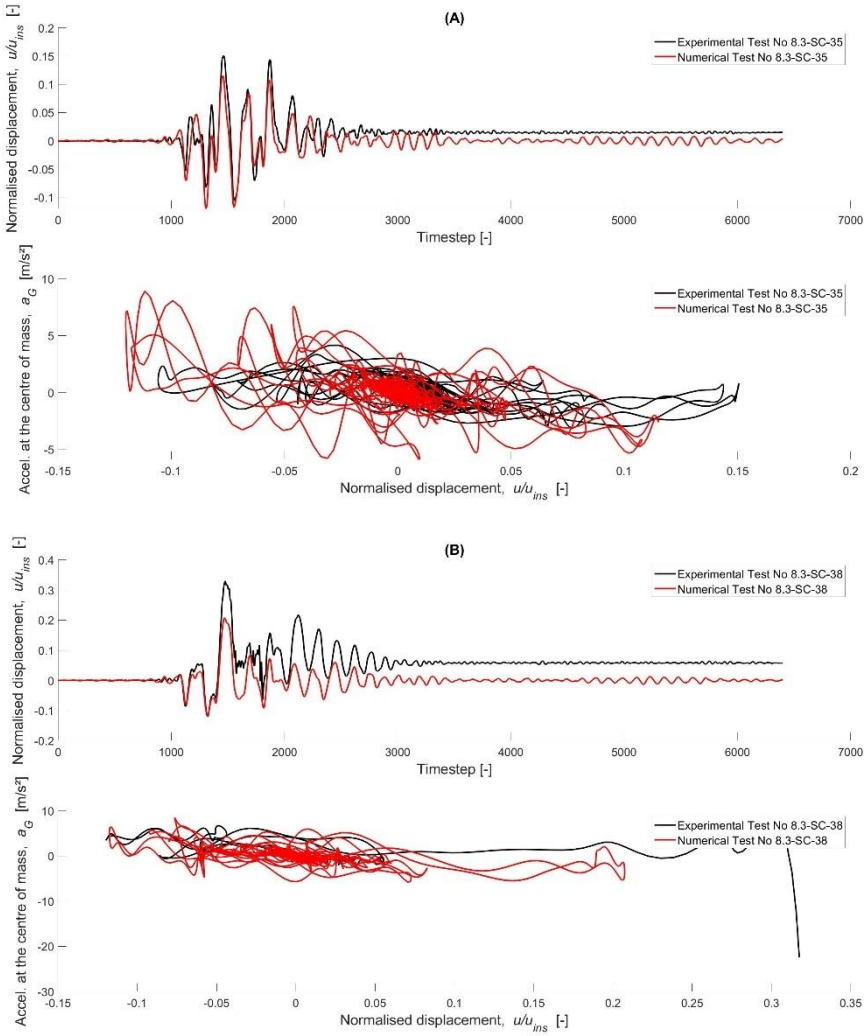

Figure 28: Comparison between the experimental and numerical responses of the slender chimney in the EUC-BUILD-8.3 tests: (A) test 8.3-SC-35; and (B) test 8.3-SC-38

5.1.3.3 South Parapet

In the case of the South parapet, the numerical simulations of the experimental response looked good for tests 8.3-SP-32 and 8.3-SP-35, as seen in Figure 29 (B) and (C). The numerical simulations capture well the peak values, both positive and negative. Only a comment should be made on the slight overestimation of the final part of the responses, from around time step 3000 onwards.

Test 8.3-SP-29 shows a generally good representation of the experimental response by the numerical simulation; only the two most significant peaks (one negative and one positive) are underestimated by the numerical model with a difference in value of around 0.4 and 0.1 in terms of normalised displacement for the negative and positive direction, respectively.

The analysis software simulates the 8.3-SP-38 test start, in the range from time step 0-2200, very well. After that, the numerical response underestimates the smaller peak values, having a normalised displacement difference of 0.4 for the negative peaks, and around 0.2 for the positive peaks.

Table 28: Calibrated values for the input model parameters of the cracked South parapet for the 8.3-SP tests

Test name	**Height h [m]** h_{nom} **= 0.84 m**	a_1	a_3	***CorrCoeff***
8.3-SP-29	0.840	0.052	0.850	0.920
8.3-SP-32	0.924	0.096	0.893	0.891
8.3-SP-35	0.882	0.104	0.850	0.855
8.3-SP-38	0.840	0.040	0.893	0.720

Table 29: Ranges of the calibrated input model parameters of the cracked South parapet for the 8.3-SP tests

Input parameter	**Lower bound**	**Upper bound**
Height h [m]	0.840	0.924
a_1	0.040	0.104
a_3	0.850	0.893
CorrCoeff	0.720	0.920

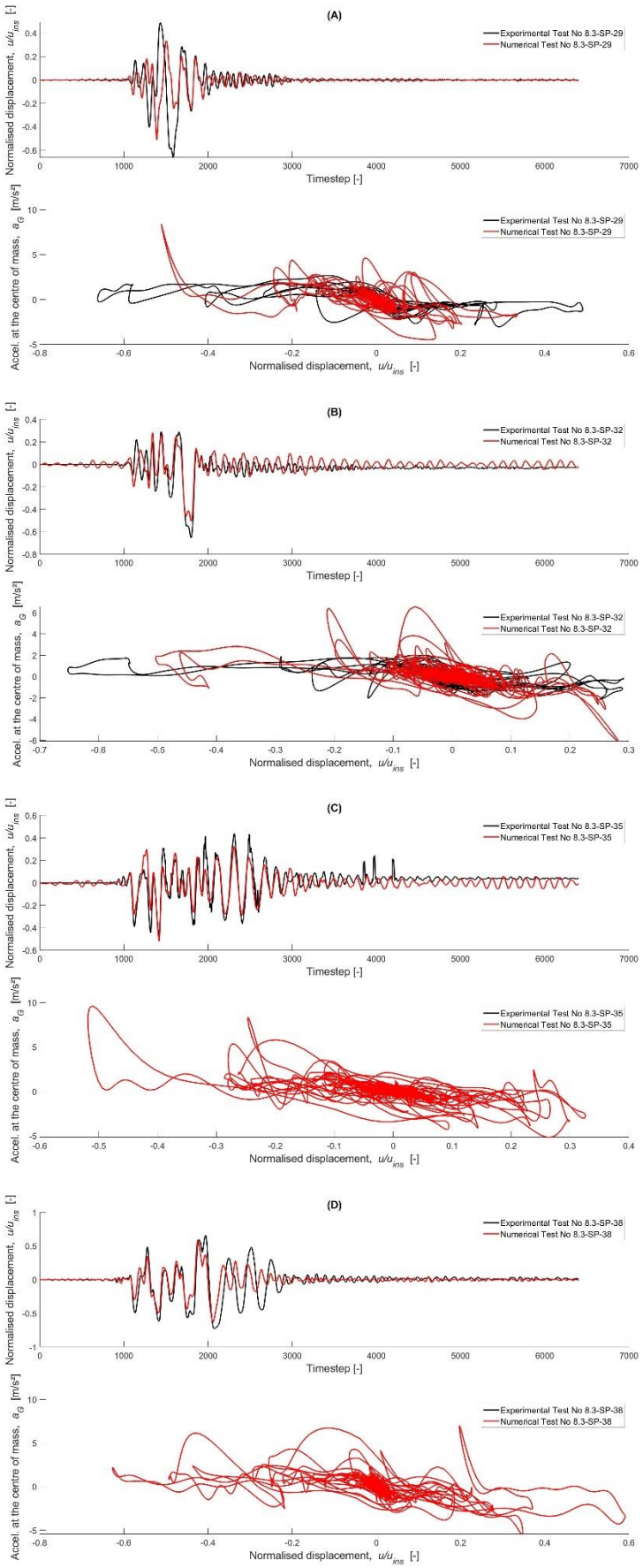

Figure 29: Comparison between the experimental and numerical responses of the South parapet in the EUC-BUILD-8.3 tests: (A) test 8.3-SP-29; (B) test 8.3-SP-32; (C) test 8.3-SP-35; and (D) 8.3-SP-38

5.1.3.4 East Parapet

The East parapet showed signs of structural damage for the first time during the tests on the EUC-BUILD-8.3 building specimen, due to the additional horizontal acceleration component acting perpendicular to the North-South axis of the parapet. The first damage occurred at the 8.3-EP-20 test.

The numerical simulations of all five tests are satisfactory. They reproduce both overall responses as the peak responses in a reliable way, which can be seen in Figure 30 and Figure 31. In test 8.3-EP-35, a small shift of the entire East parapet is visible in the displacement response time-series graph. Nevertheless, the analysis software manages to create a proper consideration of the normalised displacement.

Table 30: Calibrated values for the input model parameters of the cracked East parapet for the 8.3-EP tests

Test name	**Height *h* [m]** h_{nom} **= 0.66 m**	a_1	a_3	***CorrCoeff***
8.3-EP-20	0.693	0.016	0.998	0.713
8.3-EP-29	0.792	0.009	0.760	0.720
8.3-EP-32	0.759	0.030	0.867	0.784
8.3-EP-35	0.726	0.056	0.980	0.800
8.3-EP-38	0.759	0.063	0.903	0.808

Table 31: Ranges of the calibrated input model parameters of the cracked East parapet for the 8.3-EP tests

Input parameter	**Lower bound**	**Upper bound**
Height *h* [m]	0.693	0.792
a_1	0.009	0.063
a_3	0.760	0.998
CorrCoeff	0.713	0.808

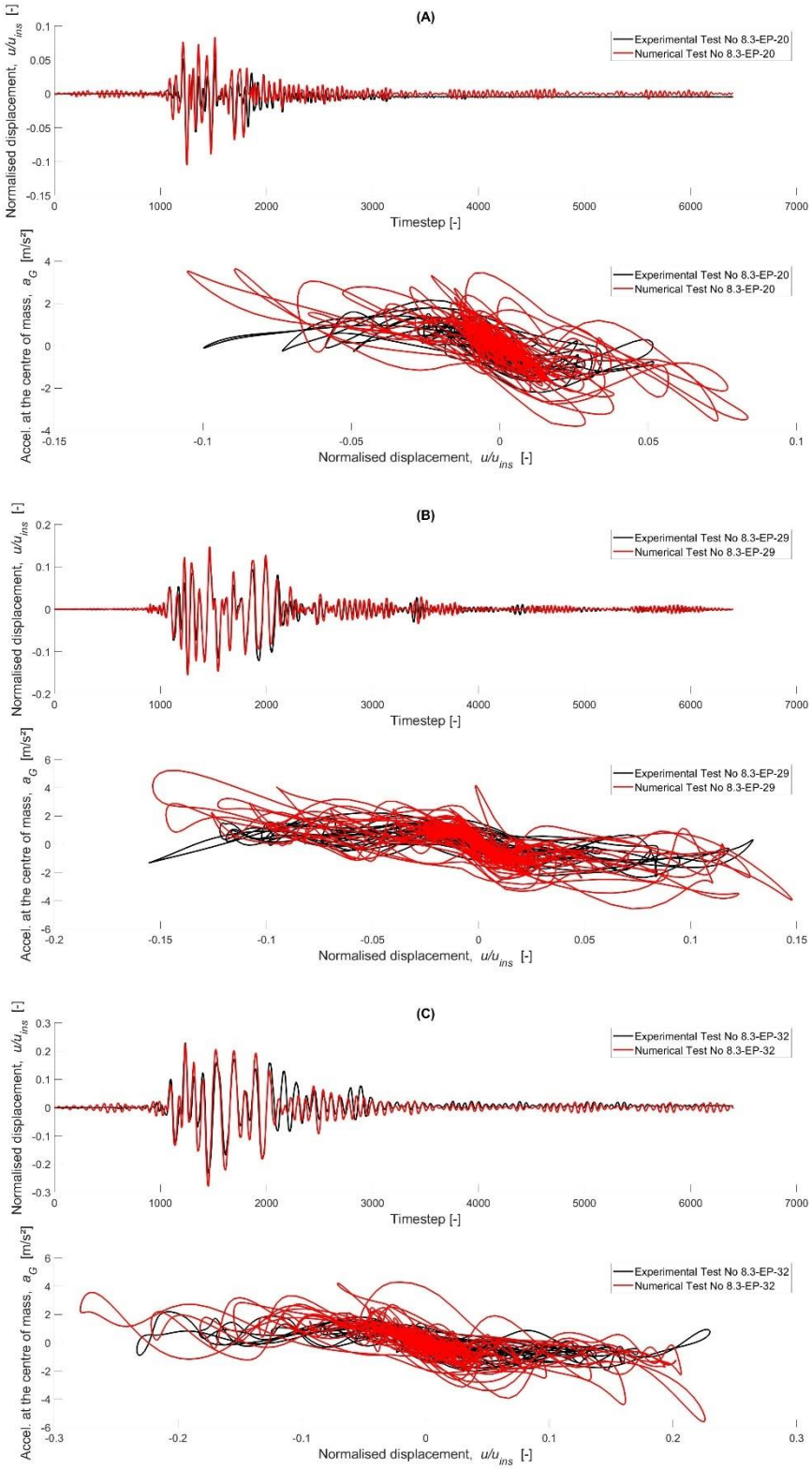

Figure 30: Comparison between the experimental and numerical response of EUC-BUILD-8.3 East parapet tests: (A) test 8.3-EP-20; (B) test 8.3-EP-29; and (C) 8.3-EP-32

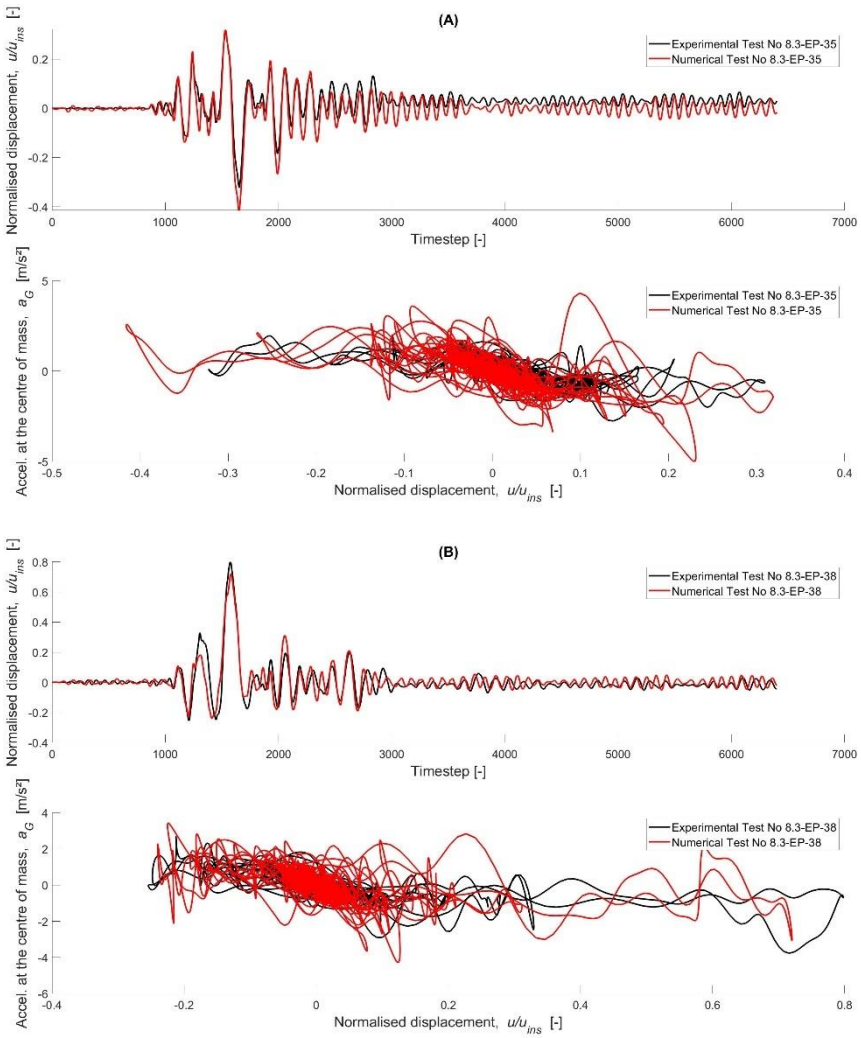

Figure 31: Comparison between the experimental and numerical responses of the East parapet in the EUC-BUILD-8.3 tests: (A) test 8.3-EP-35; and (B) 8.3-EP-38

5.1.3.5 West Parapet

Similar to the previous building specimens, the West parapet of building EUC-BUILD-8.3 did not suffer any structural damage throughout the test sequence.

5.1.4 Summary of Analysis Results for the Post-Crack Response

As shown in the preceding sections, the analysis software *Trilly* is capable of simulating well the seismic response of the components for both horizontal only and combined horizontal plus vertical input accelerations. Table 32 summarises the lower and upper values of the different input parameters for all building components and every considered test. The height tends to vary considerably when the number of acceleration components the building component is subjected to increases. This is especially noticeable for the gable wall. The height has also been shown throughout the simulations to be the most influential parameter on the accuracy of the simulations. The values of a_1 seem to maintain values that do not differ too much within one component. For a_3, the same conclusion can be made. All values of the parameter stay reasonably in range to one another within the testing sequences of one specific component. The correction coefficient is a parameter that, due to being indirectly linked with the height parameter through the CR, changes considerably within the tests of one component. The ratio of the plateau region height, $F_{0,Ratio}$, tends to differ substantially within one building specimen test sequence with a difference in value of around 0.30. However, the range of the $F_{0,Ratio}$ does show to keep relatively constant values between the different building specimens.

Table 32: Input model parameters for the simulation of the cracked elements: comparison of all building tests

	Building specimen	Height *h* [m]		a_1		a_3		*CorrCoeff*		$F_{0,Ratio}$	
		Lower	Upper	Lower	Upper	Lower	Upper	Lower	Upper	Lower	Upper
Gable wall	EUC-BUILD-8.1	2.231	2.328	0.012	0.034	0.945	0.99	0.250	0.380		
	EUC-BUILD-8.2	1.552	1.746	0.011	0.030	0.900	1.000	0.195	0.495		
	EUC-BUILD-8.3	1.649	2.134	0.018	0.020	0.945	0.998	0.330	0.500		
Slender chimney	EUC-BUILD-8.1	1.734	2.488	0.001	0.034	0.800	0.900	0.175	0.980	0.50	0.80
	EUC-BUILD-8.2	1.632	2.346	0.018	0.024	0.850	0.850	0.560	1.050	0.60	0.90
	EUC-BUILD-8.3	1.632	2.244	0.007	0.033	0.800	0.893	0.600	1.015	0.55	0.90
South parapet	EUC-BUILD-8.1	0.672	0.756	0.026	0.084	0.893	0.893	0.800	0.808		
	EUC-BUILD-8.2	0.672	1.008	0.024	0.084	0.808	0.893	0.560	0.950		
	EUC-BUILD-8.3	0.840	0.924	0.040	0.104	0.850	0.893	0.720	0.920		
East parapet	EUC-BUILD-8.1	*N.C.*	*N.C.*	*N.C.*	*N.C.*	*N.C.*	*N.C.*	*N.C.*	*N.C.*		
	EUC-BUILD-8.2	*N.C.*	*N.C.*	*N.C.*	*N.C.*	*N.C.*	*N.C.*	*N.C.*	*N.C.*		
	EUC-BUILD-8.3	0.693	0.792	0.009	0.063	0.760	0.998	0.713	0.808		

N.C.: not calibrated

5.1.5 Comparison of EVD Models

This section discusses a comparison between the three EVD models detailed in Chapter 2. In the analysis results presented above, the simulations of the response of the cracked elements were performed using the CDC damping model. However, as explained in Section 2.4, there are two other possible damping types: i) the constant damping ratio (CDR); and ii) the stiffness-proportional damping ratio (SDR).

The comparison of the efficiency of the different EVD models is shown here only on the slender chimney of specimen EUC-BUILD-8.3. Figure 32 to Figure 36 show the results of the numerical simulations. Based on these simulations, it seems that all three EVD models show satisfactory results in numerically simulating the experimental response of the slender chimney.

Figure 32 shows for test 8.3-SC-20 that both CDR and SDR damping models capture slightly better both the positive and the negative peak displacements. However, by taking a closer look at the simulation results, it is visible that the CDC model does a better job in simulating the overall response-history of the component. The CDC damping model better simulates the smaller peaks from time step 2000 onwards. In Figure 33, a similar simulation of the peak experimental values is seen between the different damping models. Nevertheless, the non-peak response of the chimney is most accurately simulated by the CDC damping model. The numerical simulation of 8.3-SC-35 and 8.3-SC-38, confirm that the overall response of the numerical simulation is most suitable using the CDC damping model. Figure 34, on the contrary, shows that the CDC model generates the most satisfactory peak value simulation. Showing an excellent numerical response from time step 2000 onwards, the SDR model shows an adequate overall simulation.

The input parameters, listed in Table 33, for each test comparison, shows that the height h the a_3 value, and the plateau region factor $F_{0,Ratio}$ remain almost constant between the different damping models within one specific test. The value of a_1, however, tend to show an occasional deviating value. The correction coefficient shows different values for each damping model, making it more difficult to predict. However, generally, except for test 8.3-SC-32, a rising trend in the correction coefficient value can be seen; with the lowest value being for the CDC damping model, and the highest being linked to the SDR damping model.

This way, it can be concluded that overall, for the slender chimney of EUC-BUILD-8.3, subjected to three-directional seismic input motions, the constant CDC model seems to be the most competent damping model. However, the use of a CDR or SDR model can also be considered due to arriving at similar results. In case one of the latter EVD models is employed, there is the necessity to adapt the input parameters to new values. The input parameters for the three EVD models of the EUC-BUILD-8.3 slender chimney are listed in Table 33, in which is visible that the parameter that changes most in between the different EVD models is the correction coefficient for the analytical CR. In any way, there is a definite need to conduct more research on this particular topic.

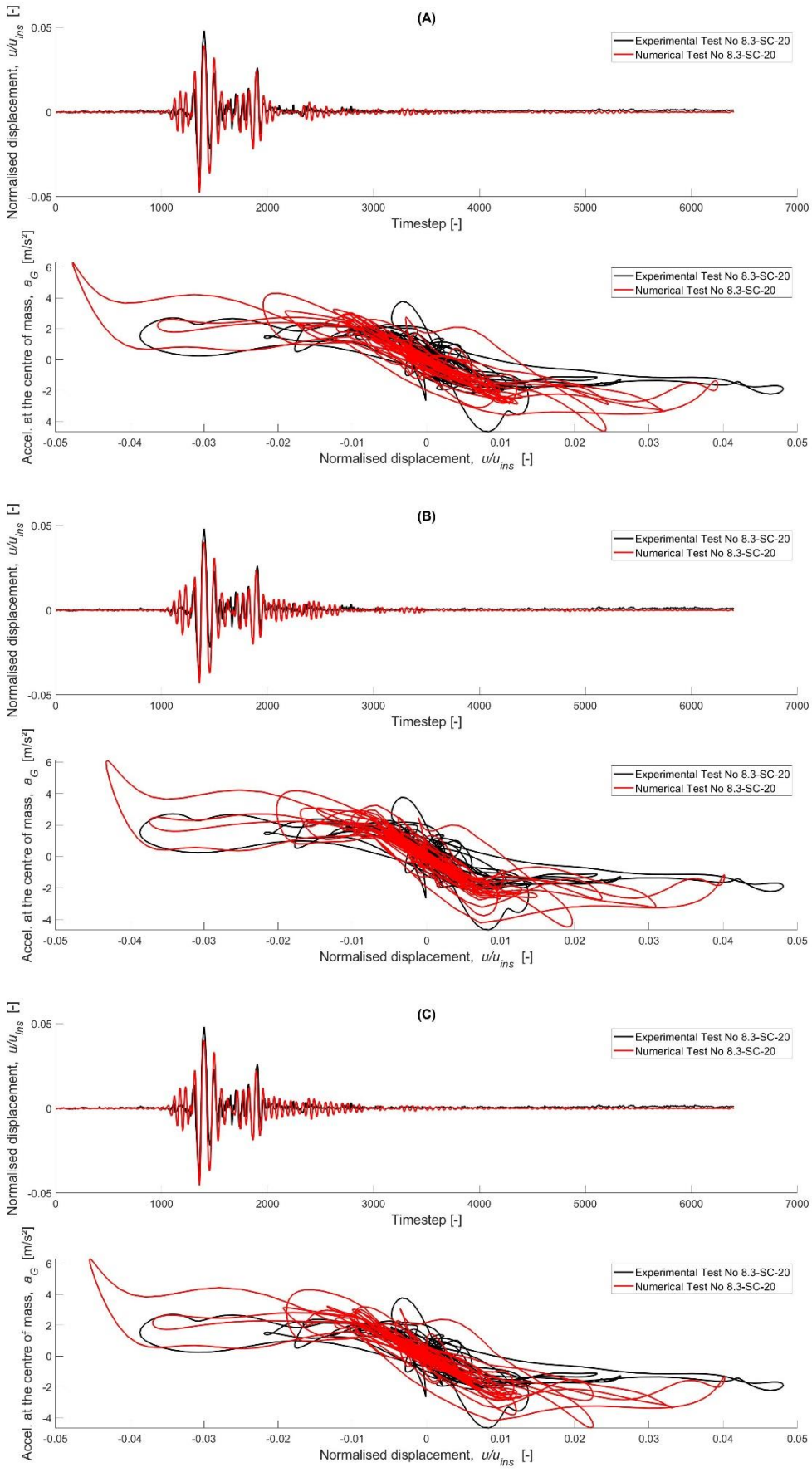

Figure 32: Simulation of the rocking response of the cracked slender chimney during test 8.3-SC-20 using: (A) CDC damping model; (B) CDR damping model; and (C) SDR damping model

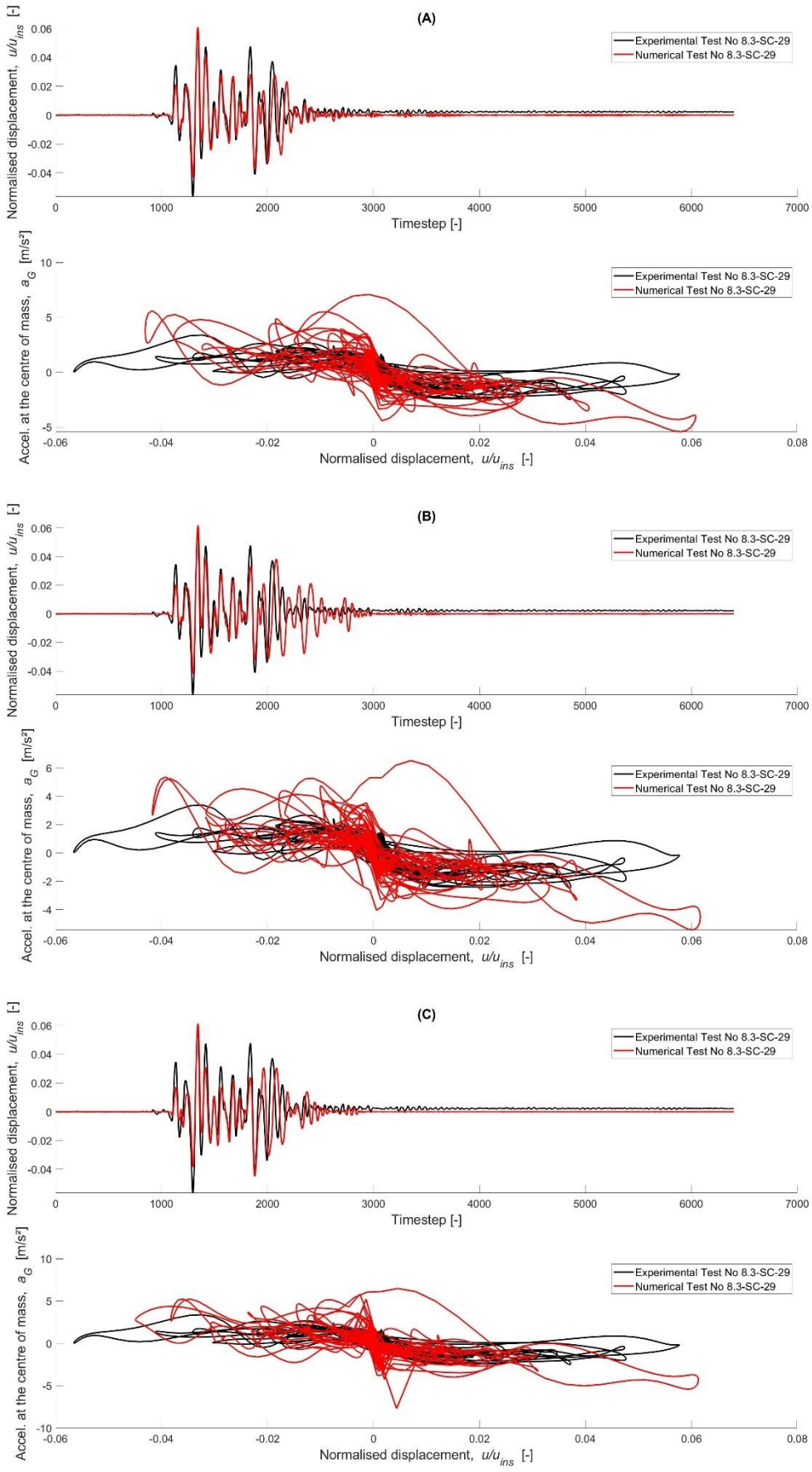

Figure 33: Simulation of the rocking response of the cracked slender chimney during test 8.3-SC-29 using: (A) CDC damping model; (B) CDR damping model; and (C) SDR damping model

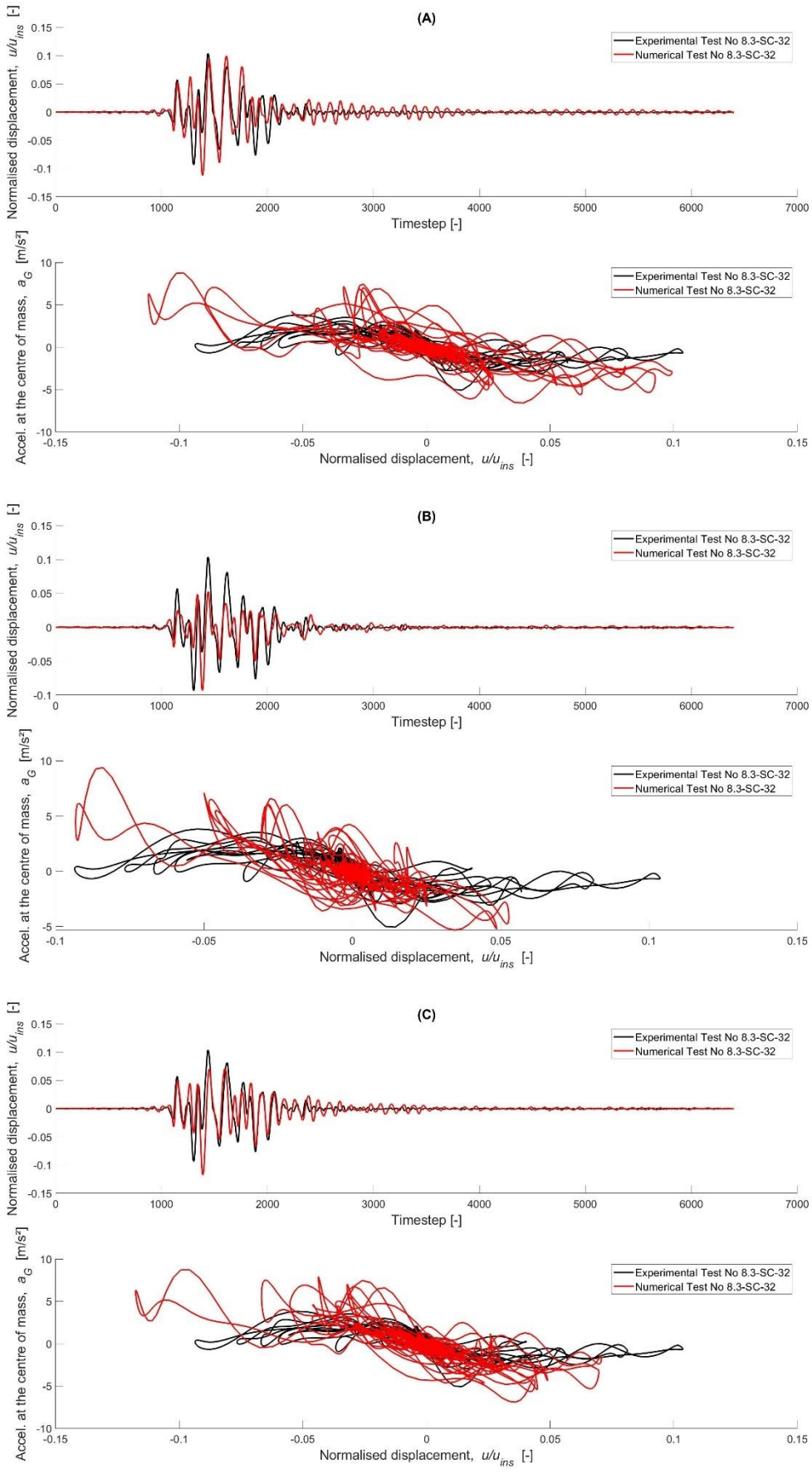

Figure 34: Simulation of the rocking response of the cracked slender chimney during test 8.3-SC-32 using: (A) CDC damping model; (B) CDR damping model; and (C) SDR damping model

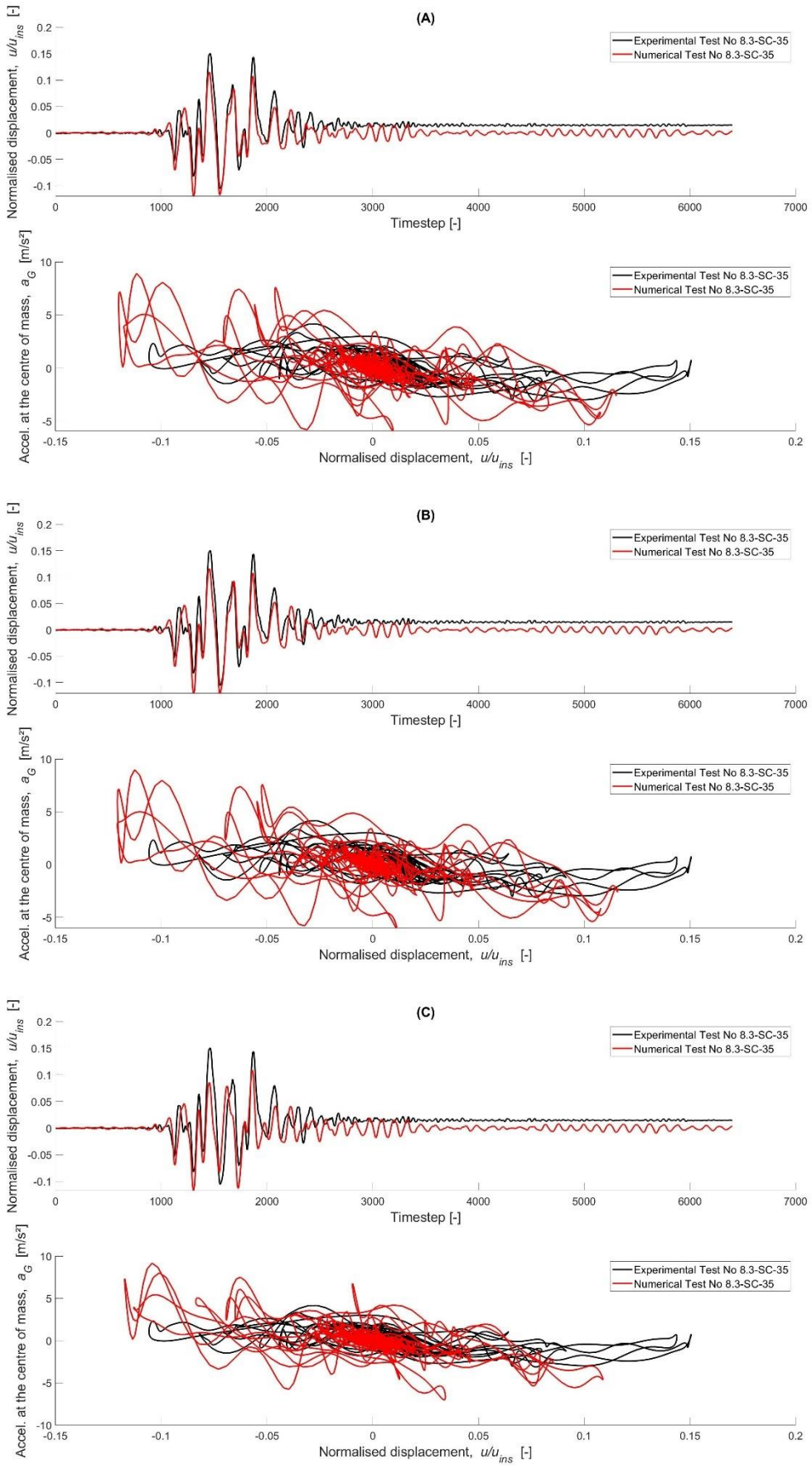

Figure 35: Simulation of the rocking response of the cracked slender chimney during test 8.3-SC-35 using: (A) CDC damping model; (B) CDR damping model; and (C) SDR damping model

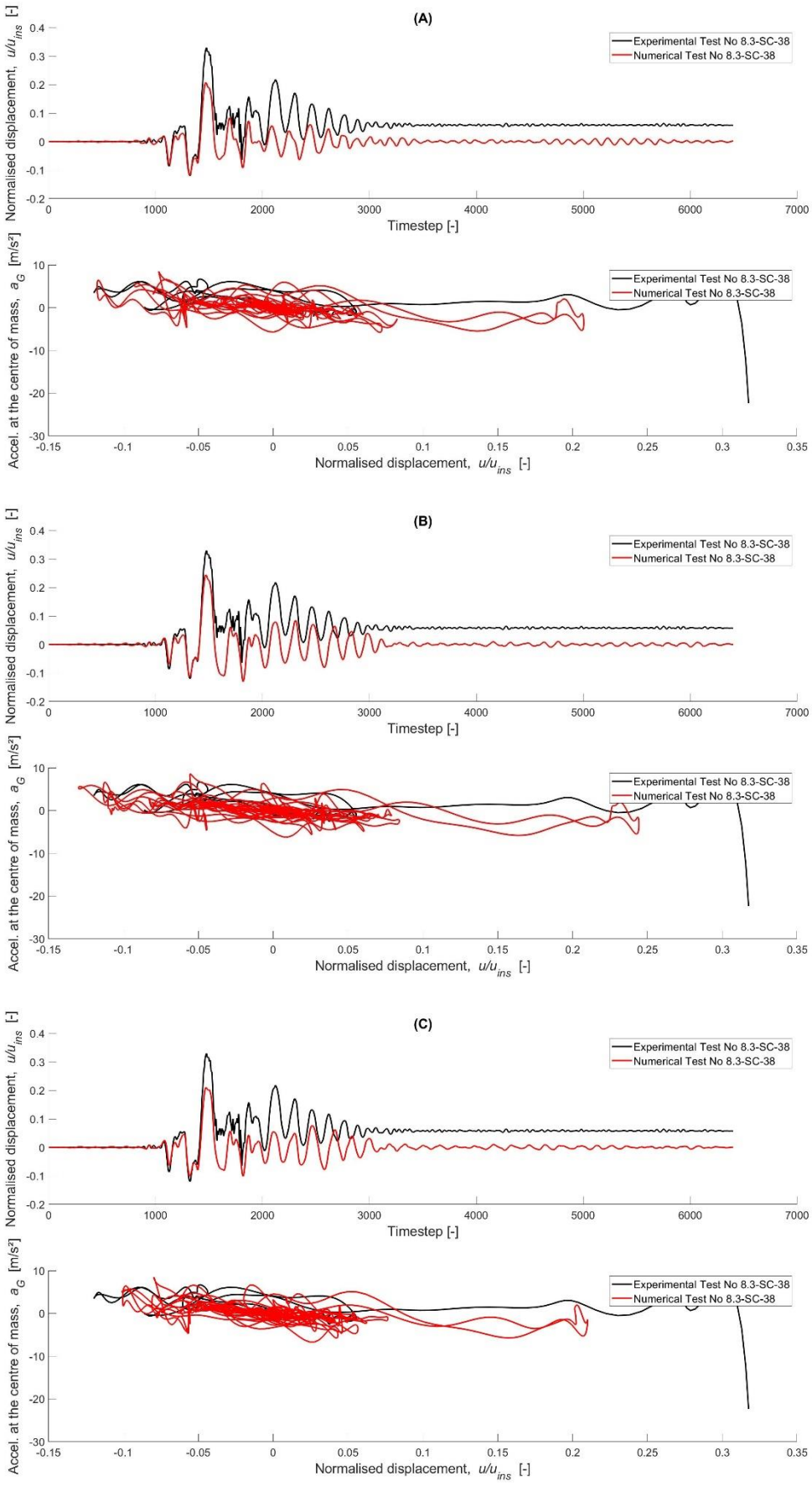

Figure 36: Simulation of the rocking response of the cracked slender chimney during test 8.3-SC-38 using: (A) CDC damping model; (B) CDR damping model; and (C) SDR damping model

Table 33: Input model parameters for the simulation of the rocking response of the cracked slender chimney: comparison of the different EVD models

	EVD damping model	**Height h [m] h_{nom} = 2.04 m**	a_1	a_3	*CorrCoeff*	$F_{0,Ratio}$
8.3-SC-20	CDC	1.632	0.010	0.850	0.805	0.90
	CDR	1.836	0.007	0.850	0.980	0.95
	SDR	1.632	0.009	0.850	1.085	0.90
8.3-SC-29	CDC	2.244	0.0007	0.800	0.600	0.60
	CDR	2.142	0.0008	0.800	0.900	0.50
	SDR	2.040	0.0003	0.800	0.975	0.45
8.3-SC-32	CDC	1.632	0.033	0.893	1.015	0.90
	CDR	1.632	0.060	0.893	0.560	0.90
	SDR	1.632	0.030	0.850	1.015	0.85
8.3-SC-35	CDC	2.244	0.024	0.808	0.770	0.60
	CDR	2.244	0.024	0.850	0.910	0.60
	SDR	2.346	0.027	0.850	0.980	0.70
8.3-SC-38	CDC	2.142	0.022	0.808	0.770	0.55
	CDR	2.244	0.034	0.850	0.945	0.65
	SDR	2.142	0.036	0.850	0.945	0.55

5.2 Analysis of Uncracked Components

This section will discuss the simulations of the tests for the components in uncracked condition. A summary of the parameter ranges and the quality simulations will be stated at the end of this section. For this section, a reference to the explanation accompanying section 5.1 regarding the East and West parapet simulations is made.

5.2.1 EUC-BUILD-8.1

5.2.1.1 Gable Wall

The uncracked seismic response for the gable wall is shown in Figure 37. Overall, it can be stated that the numerical response shows a good simulation of the experimental seismic response for this element. Especially test 8.1-GW-22 shows satisfying results in simulating the response. In the case of the other tests, a small overestimation of the experimental response can be noticed after the initial peak values. Apart from that, the 8.1-GW-9 numerical response shows to underestimate the peak values between time step 1000 and 1200 by half their experimental value.

Due to the building component not being cracked, the normalised displacements have smaller values of 0.01 to 0.1, compared to the responses in cracked condition (with values of 0.3 to 0.5 in terms of normalised displacement.

Table 34: Calibrated values for the input model parameters of the uncracked gable for the 8.1-GW tests

Test name	Height h [m] h_{nom} = 1.94 m	*damp_el*	f_w [MPa]	E_{m1} [MPa]
8.1-GW-9	1.940	0.013	0.091	2400
8.1-GW-12	2.328	0.048	0.130	1500
8.1-GW-16	2.134	0.055	0.150	1200
8.1-GW-22	2.328	0.100	0.078	1600

Table 35: Ranges of the calibrated input model parameters of the uncracked gable for the 8.1-GW tests

Input parameter	Lower bound	Upper bound
Height h [m]	1.940	2.328
damp_el	0.013	0.100
f_w [MPa]	0.091	0.150
E_{m1} [MPa]	1200	2400

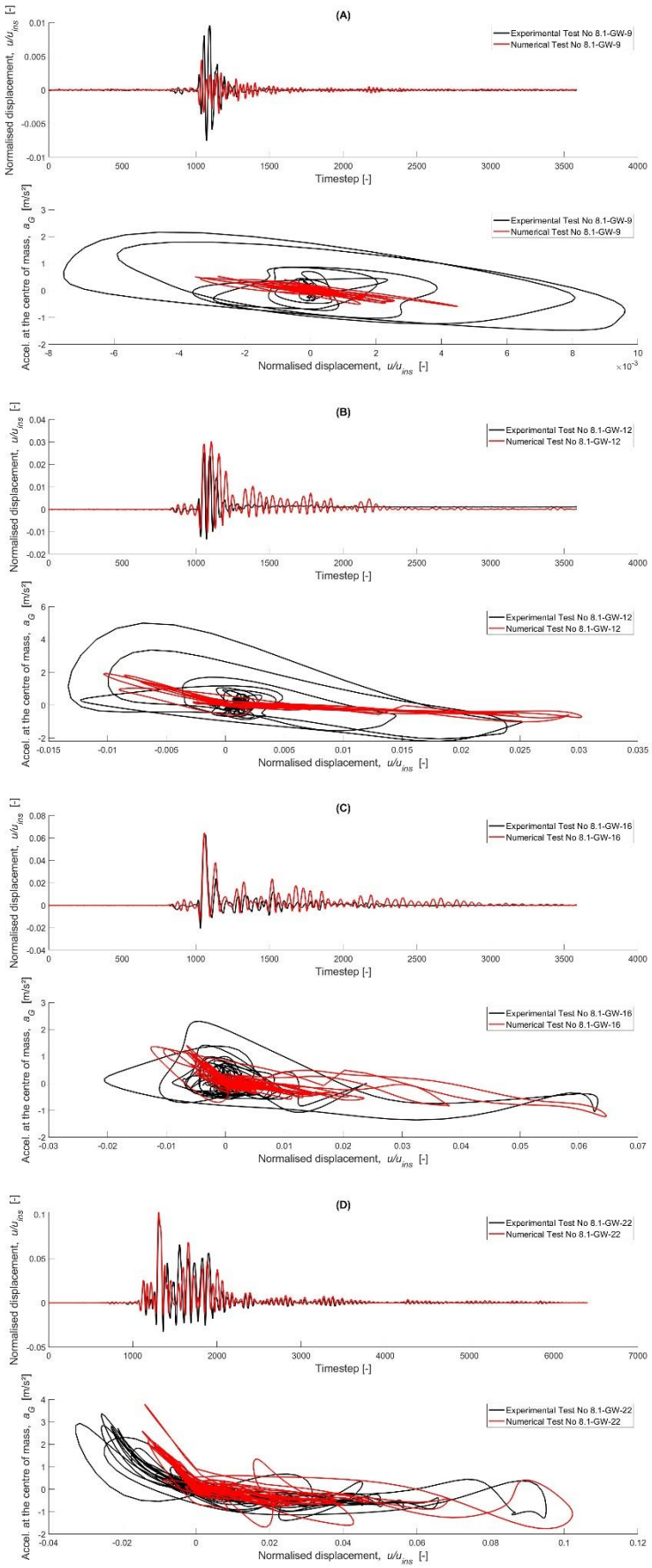

Figure 37: Comparison between the experimental and numerical responses of the gable wall in the EUC-BUILD-8.1 tests: (A) test 8.1-GW-9; (B) test 8.1-GW-12; (C) test 8.1-GW-16; and (D) 8.1-GW-22

5.2.1.2 Slender Chimney

The tests for the EUC-BUILD-8.1 slender chimney show deviating results, compared to the simulations of the gable wall. As can be seen in Figure 38, the numerical software is not entirely capable of creating an overall well-fitting simulation for test 8.1-SC-9 and 8.1-SC-12 (Figure 38 (A) and (B)).

These numerical responses show that the software well simulates the largest peak value and the seismic behaviour that shortly follows. However, due to the minimal nature of the oscillations, having a value of around 0.0005 in terms of normalised displacement, the first (between time step 0-1000) and final (between time step 1300-3500) non-peak experimental behaviour cannot be captured well by the analysis software. The numerical response in these particular cases, this behaviour is more like a static that occurs in capturing the motions of the different sensors, which cannot be simulated by the analysis software.

The 8.1-SC-16 test simulation shows a numerical underestimation of the normalised displacement peak values with a difference in value of around 0.006. The overall response, however, especially from time step 1500 onwards, is well captured by the numerical simulations.

Table 36: Calibrated values for the input model parameters of the uncracked chimney for the 8.1-SC tests

Test name	**Height h [m]** h_{nom} **= 2.04 m**	***damp_el***	f_w **[MPa]**	E_{m1} **[MPa]**
8.1-SC-9	2.244	0.088	0.267	800
8.1-SC-12	2.244	0.080	0.260	800
8.1-SC-16	2.244	0.078	0.260	400

Table 37: Ranges of the calibrated input model parameters of the uncracked chimney for the 8.1-SC tests

Input parameter	**Lower bound**	**Upper bound**
Height h [m]	2.244	2.244
damp_el	0.078	0.088
f_w **[MPa]**	0.260	0.267
E_{m1} **[MPa]**	400	800

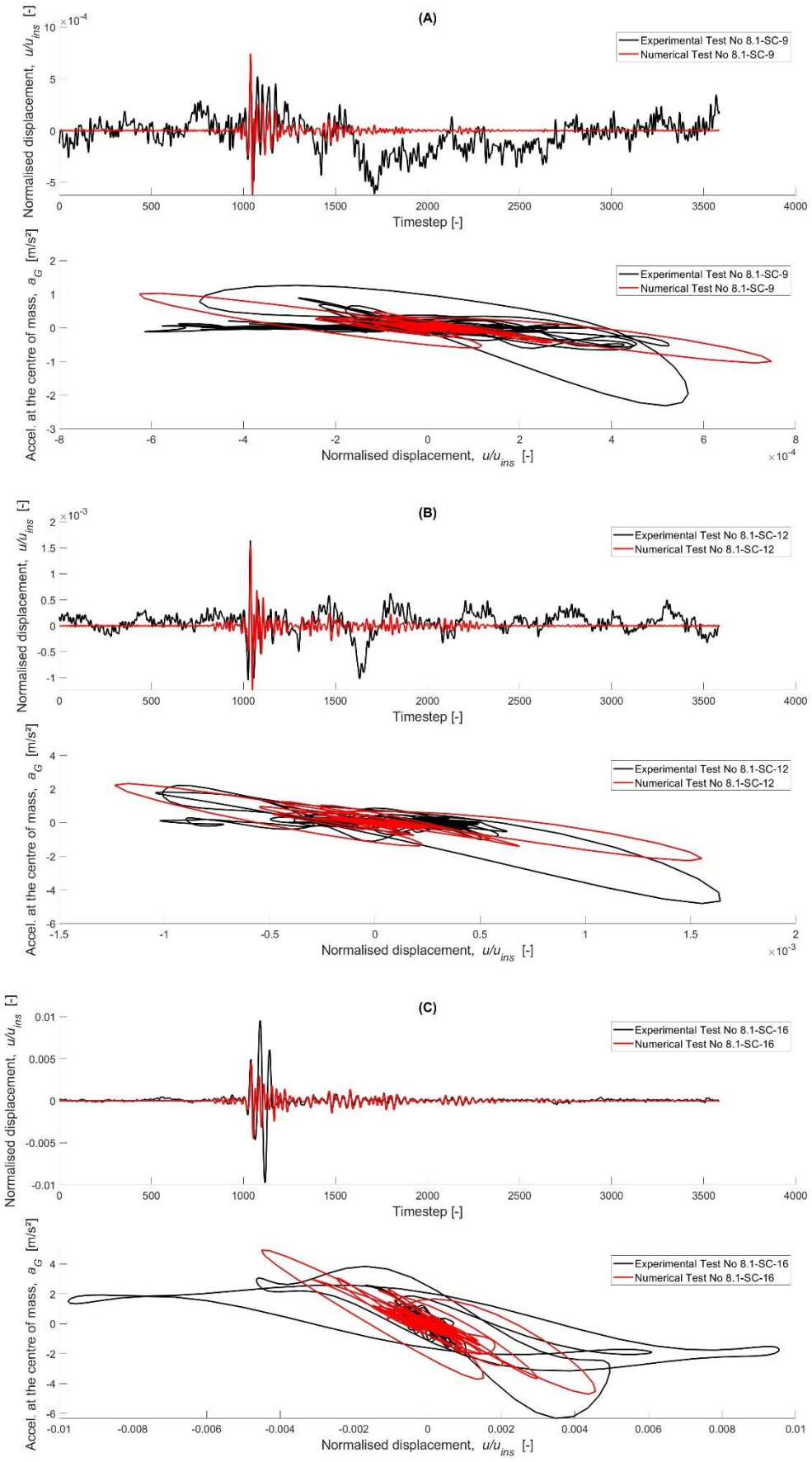

Figure 38: Comparison between the experimental and numerical responses of the slender chimney in the EUC-BUILD-8.1 tests: (A) test 8.1-SC-9; (B) test 8.1-SC-12; and (C) test 8.1-SC-16

5.2.1.3 South Parapet

In case of the South parapet under only one horizontal seismic input motion, seen in Figure 39 and Figure 40, the numerical response of the first two experimental tests show similar behaviour as the first EUC-BUILD-8.1 slender chimney tests. The experimental response consists of small oscillations, in the range of 0.002 to 0.005 in terms of normalised displacement. It can once again be noted that the numerical simulations of these two experimental responses show no good agreement, due to the experimental behaviour acting as a static.

The following tests, however, show better results in numerically simulating the experimental response. It should only be noticed that for test 8.1-SP-22, the numerical response greatly overestimates the experimental response with differences in values of approximately 0.05. This can be seen in Figure 40 (A).

Table 38: Calibrated values for the input model parameters of the uncracked South parapet for the 8.1-SP tests

Test name	Height h [m] h_{nom} = 0.84 m	*damp_el*	f_w [MPa]	E_{m1} [MPa]
8.1-SP-9	0.924	0.078	0.208	1600
8.1-SP-12	0.966	0.133	0.202	1600
8.1-SP-16	0.672	0.135	0.163	300
8.1-SP-22	0.714	0.135	0.176	700
8.1-SP-24	0.756	0.138	0.098	1600

Table 39: Ranges of the best-fit input model parameters of the uncracked South parapet for the 8.1-SP tests

Input parameter	Lower bound	Upper bound
Height h [m]	0.672	0.966
damp_el	0.078	0.138
f_w [MPa]	0.098	0.208
E_{m1} [MPa]	300	1600

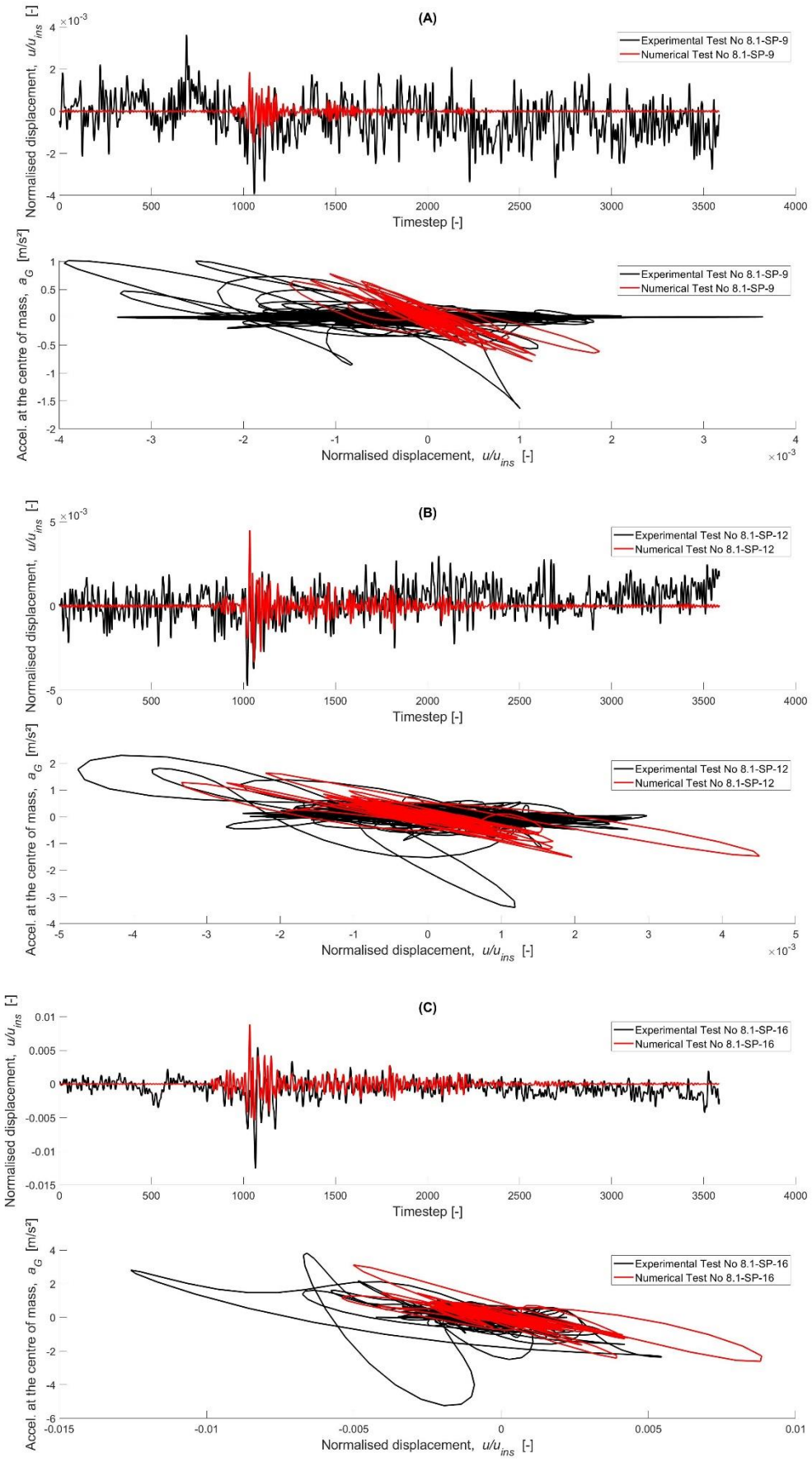

Figure 39: Comparison between the experimental and numerical responses of the South parapet in the EUC-BUILD-8.1 tests: (A) test 8.1-SP-9; (B) test 8.1-SP-12; and (C) test 8.1-SP-16

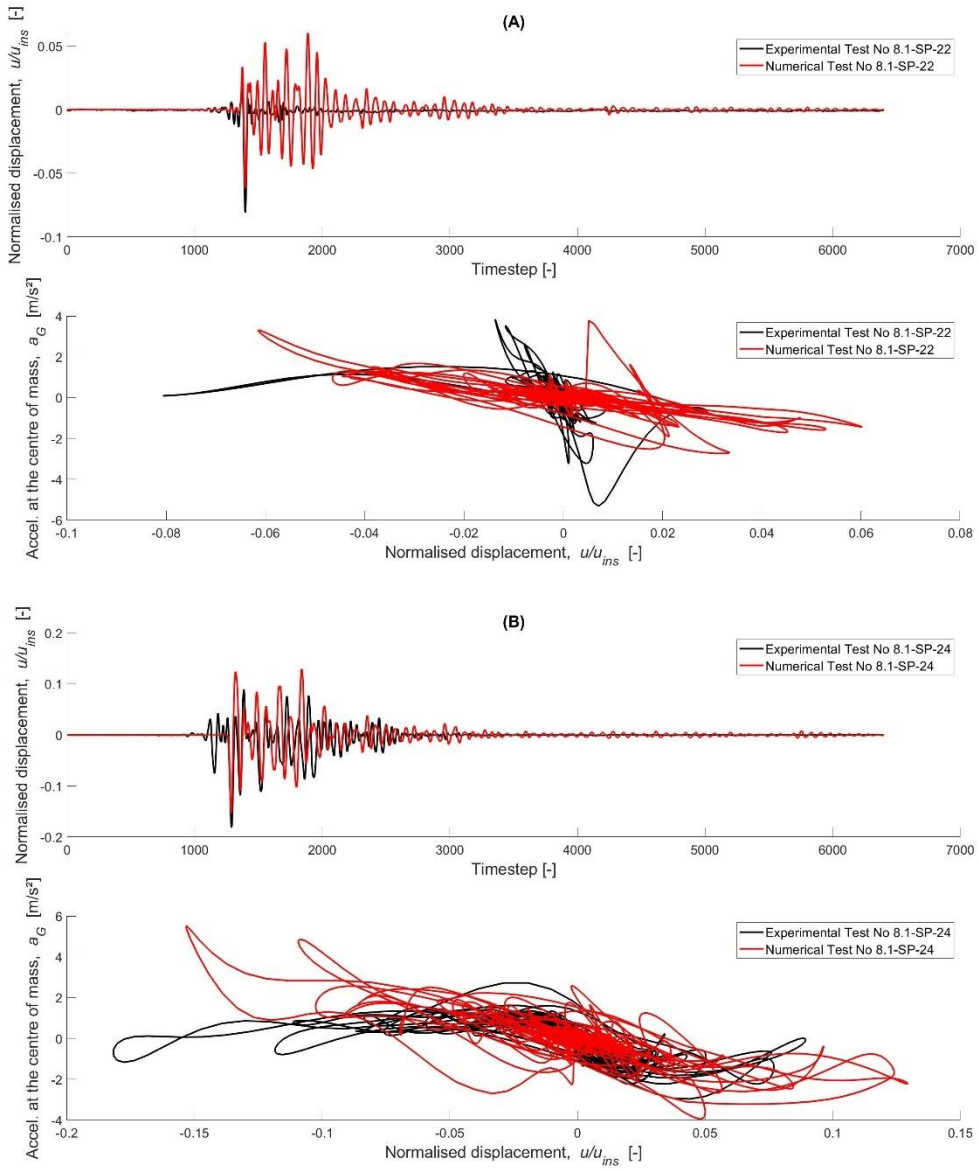

Figure 40: Comparison between the experimental and numerical responses of the South parapet in the EUC-BUILD-8.1 tests: (A) test 8.1-SP-22; and (B) test 8.1-SP-24

5.2.2 EUC-BUILD-8.2

5.2.2.1 Gable Wall

In the case of the EUC-BUILD-8.2 gable wall, the component was uncracked only during the first test. This 8.2-GW-6 test is shown in Figure 41 and shows an excellent numerical simulation of the experimental seismic response.

Table 40: Calibrated values for the input model parameters of the uncracked gable for the 8.2-GW test

Test name	Height h [m] h_{nom} = 1.94 m	*damp_el*	f_w [MPa]	E_{m1} [MPa]
8.2-GW-6	2.037	0.118	0.156	1400

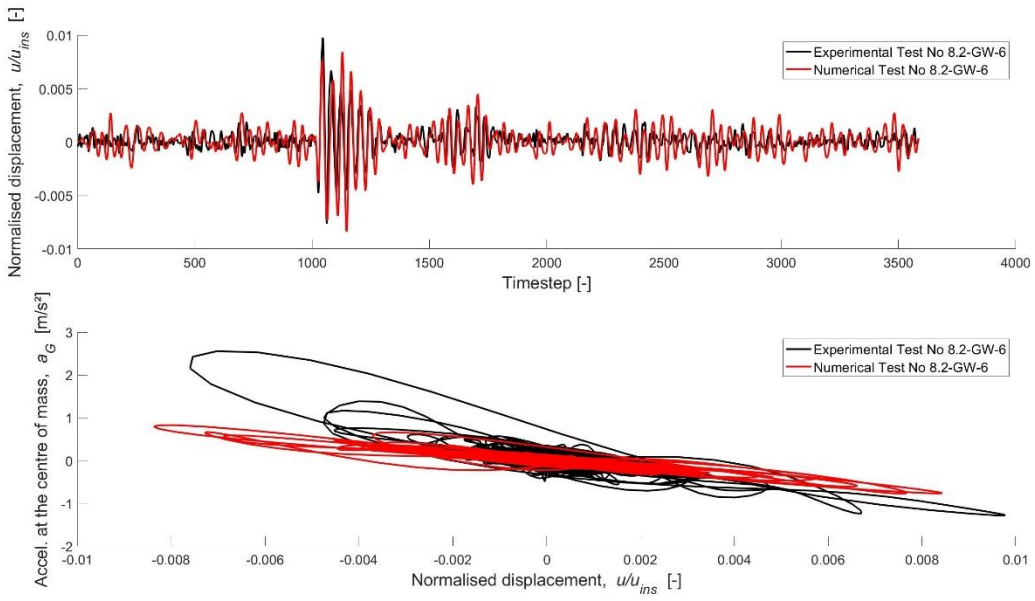

Figure 41: Comparison between the experimental and numerical responses of the gable wall in the EUC-BUILD-8.2 test 8.2-GW-6

5.2.2.2 Slender Chimney

The slender chimney of the second building specimen shows the reoccurring phenomenon of the small oscillations in the experimental response that cannot be simulated by the numerical software for test 8.2-SC-6 and 8.2-SC-9. The following tests, however, all show better simulations of the experimental response. Test 8.2-SC-21, seen in Figure 43 (B), shows the drift of the entire chimney as has already been discussed in particular cracked component condition simulations. This drift is visible from time step 2000 onwards.

Although the numerical response of test 8.2-SC-28 simulates the most significant positive and negative peak value well, it shows a less adequate simulation of the experimental seismic response. This numerical response does not take into account the smaller peak values right before and after the main peaks. So it is overall less satisfying than the previous slender chimney simulations. This test also shows different values of the input parameters, listed in Table 41.

Table 41: Calibrated values for the input model parameters of the uncracked chimney for the 8.2-SC tests

Test name	Height h [m] h_{nom} = 2.04 m	*damp_el*	f_w [MPa]	E_{m1} [MPa]
8.2-SC-6	2.142	0.060	0.169	800
8.2-SC-9	2.448	0.055	0.176	1200
8.2-SC-13	2.448	0.150	0.189	700
8.2-SC-18	2.244	0.115	0.169	400
8.2-SC-21	2.040	0.115	0.208	100
8.2-SC-28	1.938	0.048	0.046	1900

Table 42: Ranges of the calibrated input model parameters of the uncracked chimney for the 8.2-SC tests

Input parameter	Lower bound	Upper bound
Height h [m]	1.938	2.448
damp_el	0.048	0.150
f_w [MPa]	0.046	0.208
E_{m1} [MPa]	100	1900

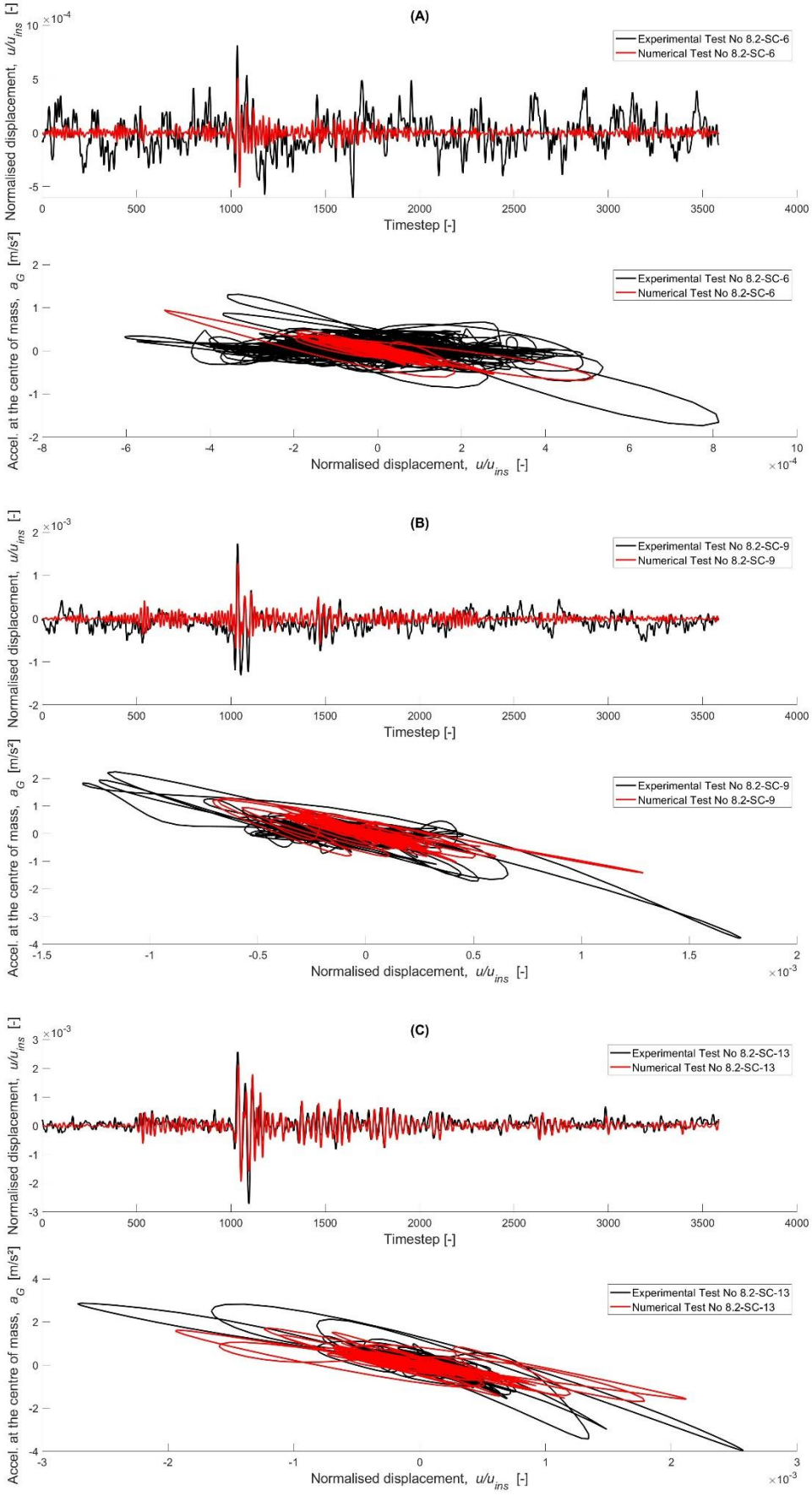

Figure 42: Comparison between the experimental and numerical responses of the slender chimney in the EUC-BUILD-8.2 tests: (A) test 8.2-SC-6; (B) test 8.2-SC-9; and (C) test 8.2-SC-13

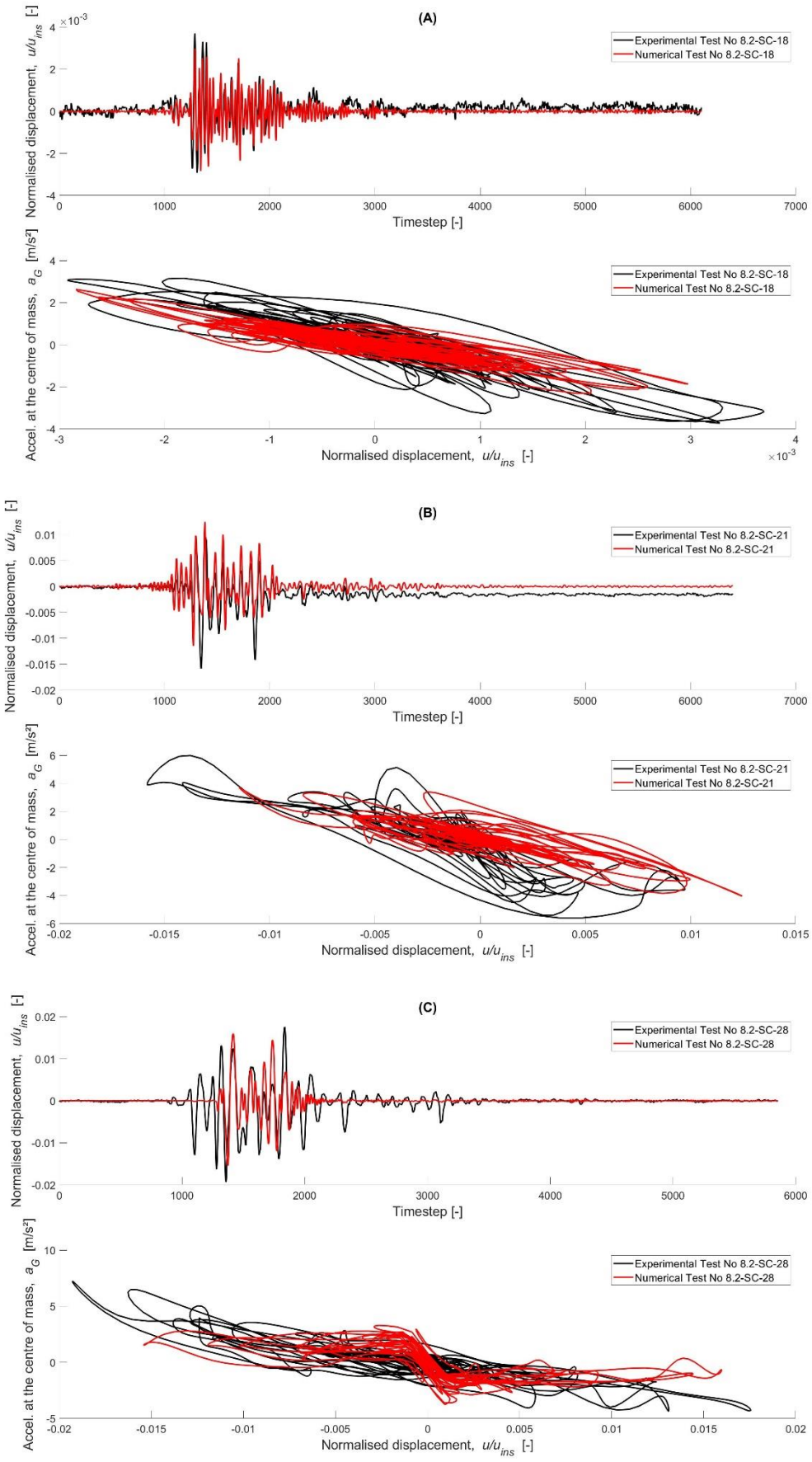

Figure 43: Comparison between the experimental and numerical responses of the slender chimney in the EUC-BUILD-8.2 tests: (A) test 8.2-SC-18; (B) test 8.2-SC-21; and (C) test 8.2-SC-28

5.2.2.3 South Parapet

The South parapet showed structural damage from the first test onward. This means that no tests for uncracked conditions could be simulated.

5.2.3 EUC-BUILD-8.3

5.2.3.1 Gable Wall

The gable wall of the third building specimen was in uncracked condition only during the first test 8.3-GW-6

The simulations of this test can be viewed in Figure 44. Even though the test consists of small normalised displacement oscillations, it shows an excellent numerical response despite occasional overestimations.

Table 43: Calibrated values for the input model parameters of the uncracked gable for the 8.3-GW-6 test

Test name	Height h [m] h_{nom} = 1.94 m	*damp_el*	f_w [MPa]	E_{m1} [MPa]
8.3-GW-6	1.746	0.040	0.026	1200

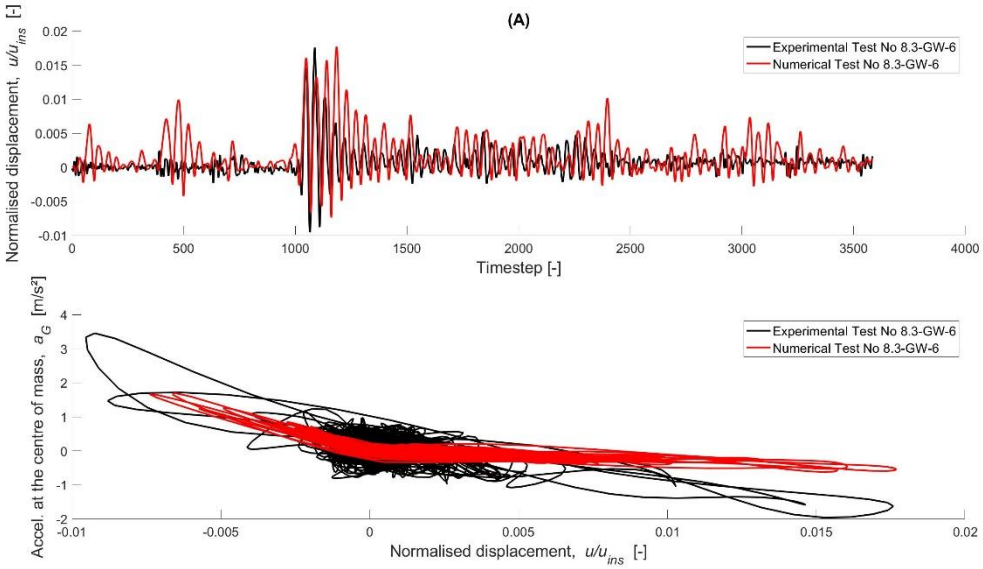

Figure 44: Comparison between the experimental and numerical responses of the slender chimney in the EUC-BUILD-8.3 test 8.3-GW-6

5.2.3.2 Slender Chimney

The EUC-BUILD-8.3 slender chimney shows the phenomenon with the minimal oscillations occurring for all three simulations. These simulations are not satisfying and the resulting ranges of parameters, as listed in Table 44 and Table 45, should be reviewed with a critical eye.

Table 44: Input parameter values of uncracked 8.3-SC tests

Test name	**Height *h* [m]** h_{in} **= 2.04 m**	***damp_el***	f_w **[MPa]**	E_{m1} **[MPa]**
8.3-SC-6	2.448	0.020	0.156	800
8.3-SC-10	2.346	0.018	0.156	1000
8.3-SC-16	2.244	0.038	0.143	800

Table 45: Input parameter range for uncracked 8.3-SC tests

Input parameter	**Lower boundary**	**Upper boundary**	**Difference**
Height *h* [m]	2.244 (1.10 *factor*)	2.448 (*1.20 factor*)	0.204
damp_el	0.018	0.038	0.020
f_w **[MPa]**	0.143	0.156	0.013
E_{m1} **[MPa]**	800	1000	200

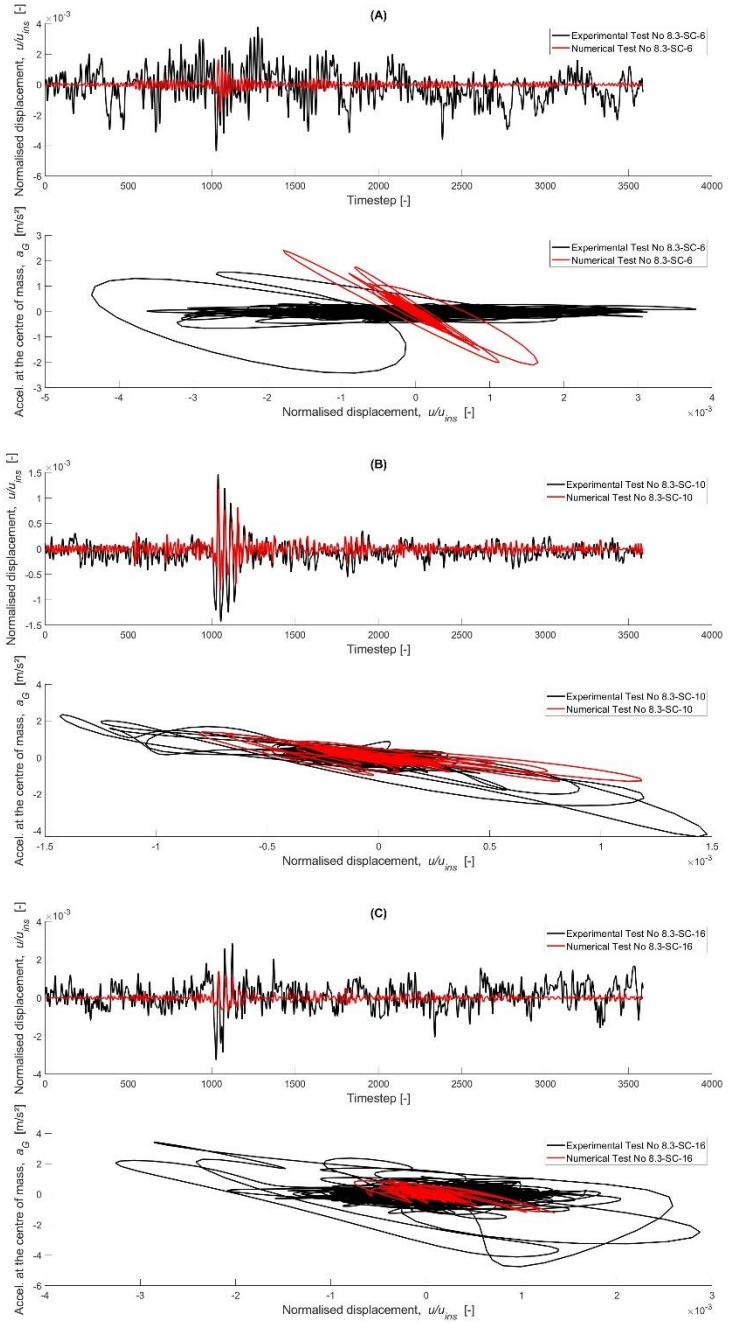

Figure 45: Comparison between the experimental and numerical responses of the slender chimney in the EUC-BUILD-8.3 tests: (A) test 8.3-SC-6; (B) test 8.3-SC-10; and (C) test 8.3-SC-16

5.2.3.3 South Parapet

The South parapet shows the small oscillation behaviour for the first test (8.3-SP-6) specifically. However, despite the small oscillations of 8.3-SP-10 and 8.2-SP-16, the numerical response simulates the experimental behaviour well, showing satisfactory results for these two tests, as can be seen in Figure 46 (B) and (C).

The final test with the component being in an uncracked state of the EUC-BUILD-8.3 South parapet also shows, apart from the overestimations of the first peak and the final oscillations (after time step 2500), an adequate simulation of the experimental response.

Table 46: Calibrated values for the input model parameters of the uncracked South parapet for the 8.3-SP tests

Test name	Height h [m] h_{nom} = 0.84 m	*damp_el*	f_w [MPa]	E_{m1} [MPa]
8.3-SP-6	0.924	0.160	0.143	3700
8.3-SP-10	0.672	0.153	0.182	400
8.3-SP-16	0.882	0.170	0.247	1300
8.2-SP-20	0.798	0.010	0.150	1600

Table 47: Ranges of the best-fit input model parameters of the uncracked South parapet for the 8.3-SP tests

Input parameter	Lower bound	Upper bound
Height h [m]	0.672	0.924
damp_el	0.010	0.170
f_w [MPa]	0.143	0.247
E_{m1} [MPa]	400	3700

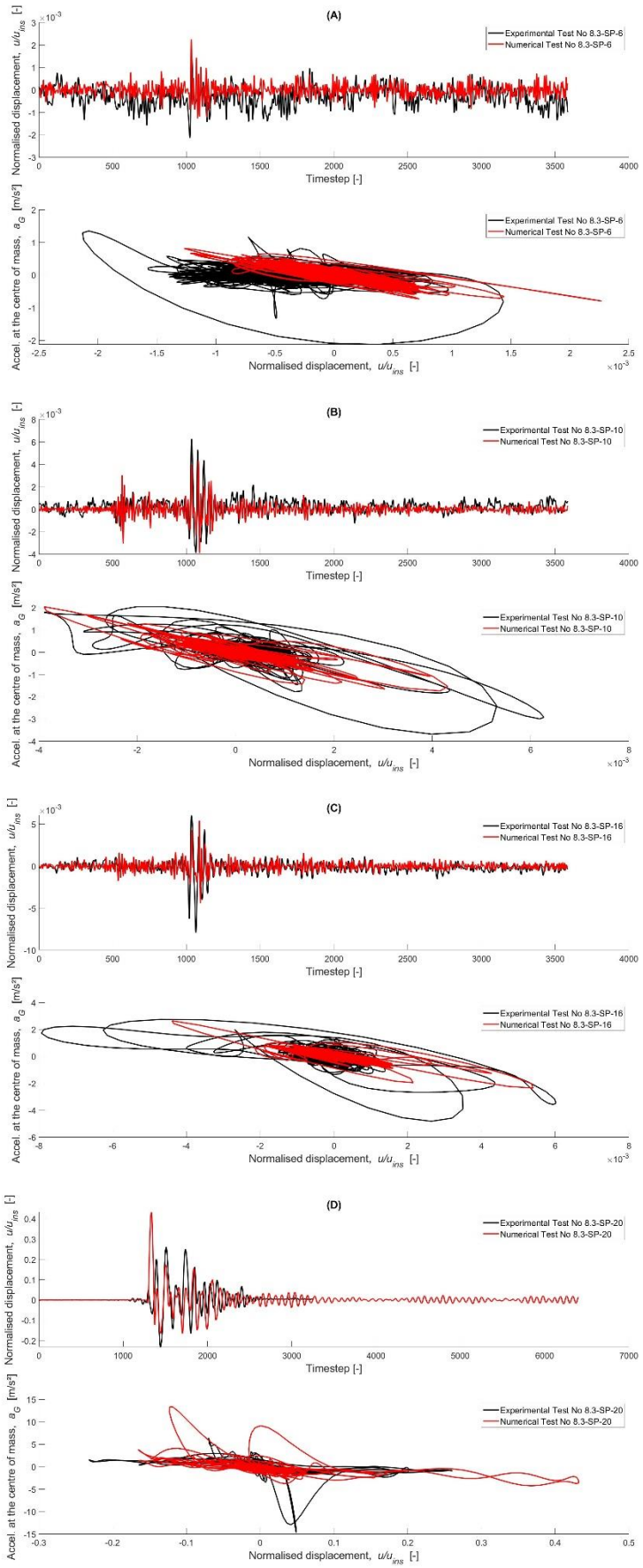

Figure 46: Comparison between the experimental and numerical responses of the South parapet in the EUC-BUILD-8.3 tests: (A) test 8.3-SP-6; (B) test 8.3-SP-10; (C) test 8.3-SP-16; and (D) 8.3-SP-20

5.2.3.4 East Parapet

In the case of the East parapet of the third building specimen, uncracked conditions occurred during the first three tests of the sequence. The simulations for these tests can be found in Figure 47. The first test, being 8.3-EP-6 shows a numerical response that is not capable of simulating the experimental response at all, neither the peak values as the overall response show corresponding values. The input parameters of this simulation are not discussed in Table 48 and Table 49 due to its inferior quality.

The following tests, however, show better results in simulating the experimental behaviour. Test 8.3-EP-10 tends to overestimate the overall behaviour of the parapet but shows a much more satisfying simulation that 8.3-EP-6 does. Even though the negative peak value is underestimated during the 8.3-EP-16 simulation, this final test does show an adequate simulation of the uncracked East parapet.

Table 48: Calibrated values for the input model parameters of the uncracked East parapet for the 8.3-EP tests

Test name	Height h [m] h_{nom} = 0.66 m	*damp_el*	f_w [MPa]	E_{m1} [MPa]
8.3-EP-10	0.759	0.050	0.091	800
8.2-EP-16	0.792	0.045	0.078	800

Table 49: Ranges of the calibrated input model parameters of the uncracked East parapet for the 8.3-EP tests

Input parameter	Lower bound	Upper bound
Height h [m]	0.759	0.792
damp_el	0.045	0.050
f_w [MPa]	0.078	0.091
E_{m1} [MPa]	800	800

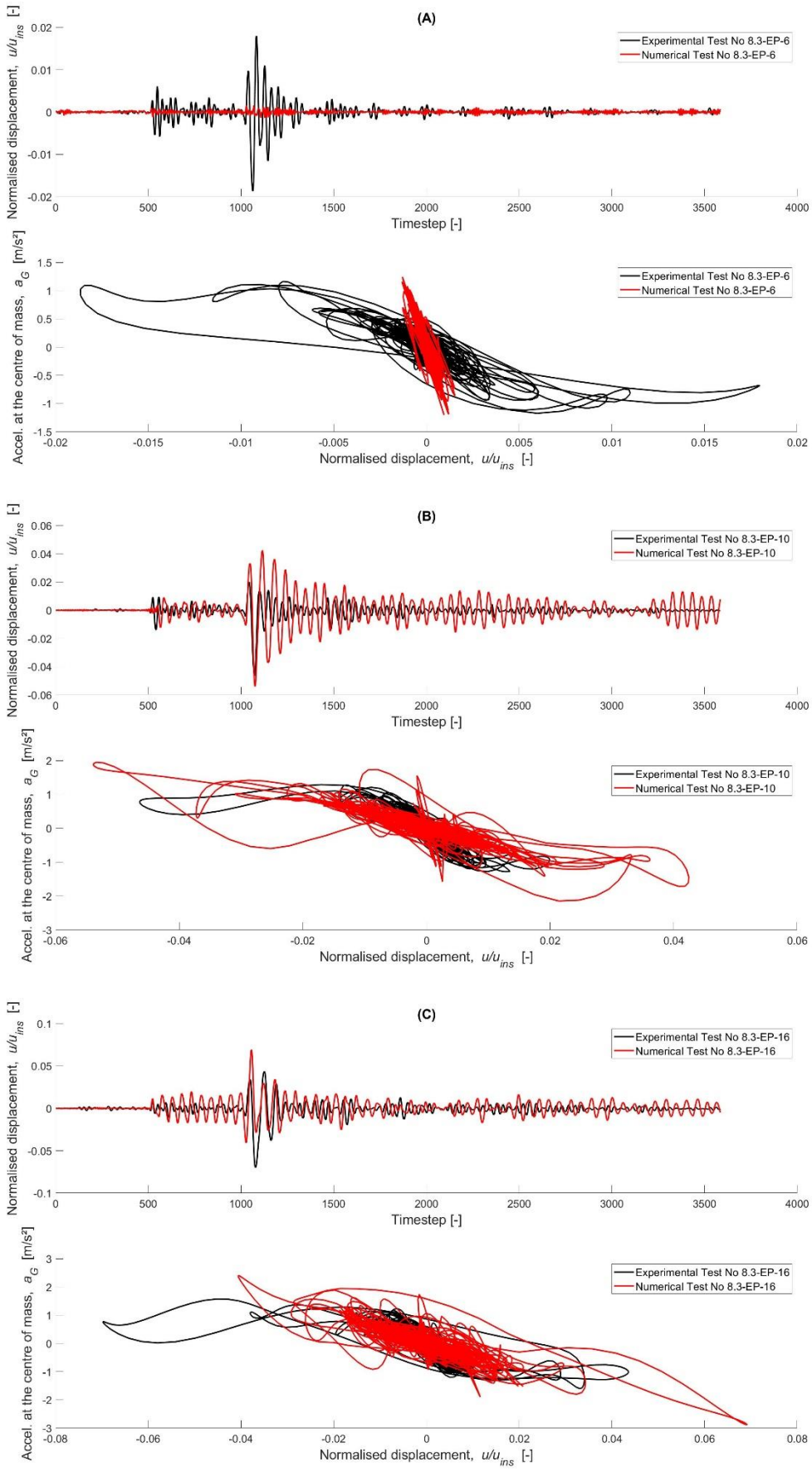

Figure 47: Comparison between the experimental and numerical responses of the East parapet in the EUC-BUILD-8.3 tests: (A) test 8.3-EP-6; (B) test 8.3-EP-10; and (C) test 8.3-EP-16

5.2.3.5 West Parapet

During the simulations of the West parapet in its uncracked condition it became clear that, because of high values of the normalised displacement (up to 0.2-0.3) during several tests, the element was actually cracked from most probably the test 8.3-WP-20 onwards. Due to this reason, the conclusion was made to not implement these simulations in the thesis, as this could probably cause uncertain and confusing results.

5.2.4 Summary of Analysis Results for the Pre-Crack Response

Table 50 below lists the range of each varying parameter for all building components and all considered building specimens in the analyses. There are a few conclusions that can be drawn when examining the outcome of these analyses. First of all, the height h seems to affect significantly the numerical response of the model. Altering this parameter results in significant sensitivity of the model during the simulations. The elastic damping coefficient is a factor that also affects greatly the numerical behaviour but, not as much as the height. The flexural strength takes a wide range of values for each building component, making it difficult to find a trend or correlation of the parameter and the accuracy of the model. The relationship between h and E_{m1} can be related to their influence on the calculation of the uncracked stiffness and the cracking displacement u_{cr}.

Table 50: Input model parameters for the simulation of the cracked elements: comparison of all building tests

	Building specimen	Height h [m]		*damp_el*		f_w [MPa]		E_{m1} [MPa]	
		Lower	Upper	Lower	Upper	Lower	Upper	Lower	Upper
Gable wall	EUC-BUILD-8.1	1.940	2.328	0.013	0.100	0.091	0.150	1200	2400
	EUC-BUILD-8.2	2.037	2.037	0.118	0.118	0.156	0.156	1400	1400
	EUC-BUILD-8.3	1.746	1.746	0.040	0.040	0.026	0.026	1200	1200
Slender chimney	EUC-BUILD-8.1	2.244	2.244	0.078	0.088	0.260	0.267	400	800
	EUC-BUILD-8.2	1.938	2.448	0.048	0.150	0.046	0.208	100	1900
	EUC-BUILD-8.3	2.244	2.448	0.018	0.038	0.143	0.156	800	1000
South parapet	EUC-BUILD-8.1	0.672	0.966	0.078	0.138	0.098	0.208	300	1600
	EUC-BUILD-8.2								
	EUC-BUILD-8.3	0.672	0.924	0.010	0.170	0.143	0.247	400	3700
East parapet	EUC-BUILD-8.1								
	EUC-BUILD-8.2								
	EUC-BUILD-8.3	0.759	0.792	0.045	0.050	0.078	0.091	800	800
West parapet	EUC-BUILD-8.1								
	EUC-BUILD-8.2								
	EUC-BUILD-8.3	0.660	0.792	0.030	0.073	0.052	0.137	500	2000

6 Conclusions

6.1 Concluding remarks

This Master's thesis aims at investigating the capabilities of the *Trilly* analysis software in simulating accurately the experimental behaviour of various full-scale URM building components. The investigations focus on elements representative of parapets, slender chimneys and gable walls typically seen in real buildings. The analyses have been performed accounting for shaking under both horizontal-only and combined horizontal-plus-vertical acting accelerations. The thesis first identifies the range of input parameters of the numerical models that best fit the experimental seismic response of the elements. In the analyses, a distinction was made between the response at the pre- and post-cracking conditions of the elements.

The analysis software proved successful in simulating the experimental response of all considered building components, both at the uncracked and the cracked conditions. A constant damping coefficient (CDC) was used to model the damping phenomenon due to rocking behaviour. A trilinear elastic force-displacement rule with a plateau and a descending branch was adopted to approximate the rocking behaviour of the slender chimney. On the contrary, a bilinear elastic force-displacement relationship was assigned to the thinner gable and parapet walls. Apart from the height h of the elements and the correction factor of the coefficient of restitution CR, the rest input parameters (i.e. α_1, α_3, $F_{0,Ratio}$, associated with the shape of the hysteretic rule) did not affect significantly the sensitivity of the model to capture the experimental response of the elements, when the latter were cracked. The height seems to affect significantly also the accuracy of the model to capture the behaviour of the elements in the pre-crack condition, as it controls the elastic stiffness, and the cracking force/displacement of the URM components.

The efficiency of various EVD models was also tested by comparing the simulated response of the slender chimney using all three damping models. Overall, all three EVD models showed satisfying results in simulating the experimental seismic rocking response of the cracked chimney. Nevertheless, the best results were achieved with the use of the constant damping coefficient (CDC) model. In those simulations, the values for the height h, the parameters a_1 and a_3, and the ratio $F_{0,Ratio}$ remained quasi-constant, while only the correction coefficient of the CR was modified significantly to achieve a good fit between experimental and numerical responses. The correction coefficient tends to show its lowest value for the CDC damping model, while the highest value was required for the stiffness-proportional damping ratio (SDR) model.

6.2 Future Developments

Future developments of this study may consider comparing the different EVD models for other building components, as the comparison presented here focussed only on the slender chimney. Also, a more extensive research should be conducted on simulating the dynamic response of URM building components at the moment of collapse. This was not possible in this study; the moment of collapse was not captured by the instrumentation, as part of it was dismounted from the building specimens to secure it from damage due to potential collapse.

Bibliography

[1] F. Graziotti, A. Penna and G. Magenes, "A comprehensive in situ and laboratory testing programme supporting seismic risk analysis of URM buildings subjected to induced earthquakes," *Bulletin of Earthquake Engineering,* vol. 17, pp. 4575-4599, 2018.

[2] H. Crowley, R. Pinho, J. van Elk and J. Uilenreef, "Probabilistic damage assessment of buildings due to induced seismicity," *Bulletin of Earthquake Engineering,* vol. 17, pp. 4495-4516, 2018.

[3] J. J. Bommer, B. Dost, B. Edwards, P. J. Stafford, J. van Elk, D. Doornhof and M. Ntinalexis, "Developing an Application-Specific Ground-Motion Model for Induced Seismicity," *Bulletin of the Seismological Society of America,* vol. 106, no. 1, pp. 158-173, 2016.

[4] S. Kallioras, L. Grottoli, M. Panatti and F. Graziotti, "Shake-table experiments on three identical unreinforced clay-brick masonry buildings under uni-, bi-, and tri-directional seismic input motions," EUCENTRE, Pavia, 2020.

[5] S. Kallioras, F. Graziotti, L. Grottoli, A. Penna and G. Magenes, "Effects of multi-directional seismic input on the dynamic behavior of URM structures: An experimental study," in *17th World Conference on Earthquake Engineering, 17WCEE*, Sendai, Japan, 2020.

[6] U. Tomassetti, F. Graziotti, A. Penna and G. Magenes, "Modelling one-way out-of-plane response of single-leaf and cavity walls," *Engineering Structures,* vol. 167, pp. 241-255, 2018.

[7] H. Derakhshan, M. Griffith and J. Ingham, "Airbag testing on multi-leaf unreinforced masonry walls subjected to one-way bending," *Engineering Structures,* vol. 57, pp. 512-522, 2013.

[8] F. Graziotti, U. Tomassetti, A. Penna and G. Magenes, "Out-of-plane shaking table tests on URM single leaf and cavity walls," *Engineering Structures,* vol. 125, pp. 455-470, 2016.

[9] U. Tomassetti, F. Graziotti and A. Penna, "Probabilistic seismic assessment of URM chimneys and parapets," Pavia, 2018.

[10] H. Derakhshan, M. Griffith and J. Ingham, "Out-of-plane behavior of one-way spanning unreinforced masonry walls," *Journal of Engineering Mechanics,* vol. 139, no. 4, pp. 409-417, 2013.

[11] K. Doherty, M. Griffith, N. Lam and J. Wilson, "Displacement-based seismic analysis for out-of-plane bending of unreinforced masonry walls," *Earthquake Engineering and Structural Dynamics,* vol. 31, pp. 833-850, 2002.

[12] K. T. Doherty, "An investigation of the weak links in the seismic load path of unreinforced masonary buildings," The University of Adelaide, Adelaide, 2000.

[13] M. DeJong and E. Dimitrakopoulos, "Dynamically equivalent rocking structures," *Earthquake Engineering & Structural Dynamics,* vol. 43, pp. 1543-1563, 2014.

[14] U. Tomassetti, F. Graziotti, L. Sorrentino and A. Penna, "Modelling rocking response via equivalent viscous damping," *Wiley,* vol. 48, pp. 1277-1296, 2019.

[15] M. Aslam, W. G. Godden and D. T. Scalise, "Earthquake Rocking Response of Rigid Bodies," Lawrence Berkeley National Laboratory, California, 1978.

[16] L. Sorrentino, O. AlShawa and L. Decanini, "The relevance of energy damping in unreinforced masonry rocking mechanisms. Experimental and analytical investigations," *Bulletin of Earthquake Engineering,* vol. 9, pp. 1617-1642, 2011.

[17] M. Griffith, G. Magenes, G. Melis and L. Picchi, "Evaluation of out-of-plane stability of unreinforced masonry walls subjected to seismic excitation," *Journal of Earthquake Engineering,* vol. 7, pp. 141-169, 2003.

[18] T. den Bezemer and J. van Elk, "Special Report on the Zeerijp Earthquake, 8 January 2018," NAM, Assen, the Netherlands, 2018.

[19] U. Tomassetti, "Trilly User Manual V0," Pavia, Italy.